TRANSPORT PROPERTIES OF FLUIDS

METHODOLOGY AND FORCE FIELD IMPROVEMENT USING MOLECULAR DYNAMICS SIMULATIONS

TRANSPORT PROPERTIES OF FLUIDS

METHODOLOGY AND FORCE FIELD IMPROVEMENT USING MOLECULAR DYNAMICS SIMULATIONS

Proefschrift

ter verkrijging van de graad van doctor
aan de Technische Universiteit Delft,
op gezag van de Rector Magnificus prof.dr.ir. T.H.J.J. van der Hagen
voorzitter van het College voor Promoties,
in het openbaar te verdedigen op donderdag 16 april 2020 om 10:00 uur

door

Seyed Hossein JAMALI

Werktuigbouwkundig Ingenieur,
Technische Universiteit Delft, Nederland
geboren te Teheran, Iran.

Dit proefschrift is goedgekeurd door de

promotor:	Prof.dr.ir. T.J.H. Vlugt
copromotor:	Dr. O.A. Moultos

Samenstelling promotiecommissie:

Rector Magnificus,	voorzitter
Prof.dr.ir. T.J.H. Vlugt	Technische Universiteit Delft, promotor
Dr. O.A. Moultos	Technische Universiteit Delft, copromotor
Onafhankelijke leden:	
Prof.dr. N. van der Vegt	Technische Universiteit Darmstadt, Duitsland
Prof.dr.-ing.habil. J. Vrabec	Technische Universiteit Berlin, Duitsland
Prof.dr. J.H. van Esch	Technische Universiteit Delft
Prof.dr.ir. W. de Jong	Technische Universiteit Delft
Dr. D. Dubbeldam	Universiteit van Amsterdam

This work was sponsored by NWO Exacte Wetenschappen (Physical Sciences) for the use of supercomputer facilities, with financial support from the Nederlandse Organisatie voor Wetenschappelijk Onderzoek (Netherlands Organization for Scientific Research, NWO).

Keywords: molecular simulation, molecular dynamics, transport properties, finite-size effects, force field

Printed by: Ridderprint BV | www.ridderprint.nl

Cover design by F. Jamali

ISBN 978-94-6366-256-7

An electronic version of this dissertation is available at
http://repository.tudelft.nl/.

For my beloved parents, who always supported me.

تقدیم به پدر و مادر مهربانم که همیشه پشتیبان من بوده‌اند.

CONTENTS

1

INTRODUCTION

1

The study of transport phenomena involves dynamic processes with transport of mass, momentum, or energy [1]. These dynamic processes are present everywhere from small scales, such as selective transport of nutrition materials and oxygen through the cell membrane [2], to large-scale atmospheric circulation and ocean currents [3, 4]. When the length scales of fluid flow are large compared to molecular length scales, e.g., the mean free path between collisions, the continuum description applies [5–7]. For the transport of momentum, this description would be the Navier-Stokes equation [7]. The continuum description is based on the linear response of the system to perturbations, such as a change of the chemical potential, the temperature, or the velocity [1, 6, 8]. The coefficient of the linear relation between the response (i.e, the flux, J) and the perturbation (i.e., the driving force, f) is the transport coefficient (γ):

$$J = -\gamma \nabla f \tag{1.1}$$

As shown in Fig. 1.1, transport of mass, momentum, and energy in a continuum medium is caused by the movement of constituent molecules and the interactions between these molecules. The diffusivity, viscosity, and thermal conductivity are the transport coefficients for mass, momentum, and energy transfer caused by gradients in the chemical potential, velocity, and temperature, respectively. A generalization form ofEq. (1.1) can represent more complex transport phenomena where the relation between the driving force and the flux are multidimensional [9, 10]. A flux of matter due to a temperature gradient (the Soret effect) and an energy flux due to gradients in composition are two examples that will not be considered in this thesis [6, 9–12].

Transport properties of fluids are traditionally measured in experiments [8, 9, 13, 14]. Various measurement techniques are available to obtain diffusion coefficients [15–18], shear viscosities [19–22], bulk viscosities [23–27], and thermal conductivities [28] of fluids. As shown in Fig. 1.1, the flux of mass, momentum, or heat is measured as a response to the imposed external driving force, and the linear coefficient is the corresponding transport coefficient (Eq. (1.1)). To provide a quantitative framework for obtaining transport properties of fluids, various theories and models have been developed. For instance, the kinetic theory and the quasi-universal scaling law are two important theories for calculating transport properties of dilute gases [8, 29, 30] and simple fluids [31–33].

Experiments are not always a feasible choice for conditions that are not accessible easily (e.g., high temperatures and pressures) or for fluids and materials that are toxic or explosive, or not yet synthesized. As measurements may be time-consuming and expensive [18, 34], performing many experiments to obtain transport properties at different conditions (e.g., temperatures and pressures) as well as different compositions may not economically and technically be feasible.

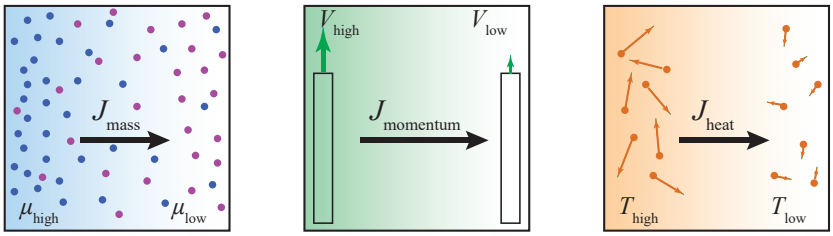

$$J_{\text{mass}} = -Đ \frac{\partial \mu}{\partial x} \qquad J_{\text{momentum}} = -\eta \frac{\partial V}{\partial x} \qquad J_{\text{heat}} = -\lambda \frac{\partial T}{\partial x}$$

Figure 1.1: Schematic representation of mass, momentum, and heat transfer due to gradients in the spatial chemical potential (μ), velocity (V), and temperature (T), respectively. The corresponding transport properties are the diffusion coefficient ($Đ$), viscosity (η), and thermal conductivity (λ), respectively.

Although accurate predictive models are needed for screening studies and improving design of industrial processes, currently available models and theories may not be applied for highly nonideal systems (such as ionic systems) as well as all conditions (e.g., conditions close to the critical point) [8, 14]. These limitations on the use of experiments and models make Molecular Dynamics (MD) an attractive choice to compute properties of fluids and materials [35, 36]. The other potential application of MD is to establish a framework for developing new models for highly nonideal mixtures [37–40].

In MD, equations of motion are integrated over time for a set of molecules inside a simulation box [35, 36, 41–43]. The trajectories of these molecules are determined based on interactions and forces between atoms. From these trajectories, different structural, thermodynamic, and transport properties of the system can be obtained. As shown in Fig. 1.2, MD can be used to obtain transport properties of working fluids in different unit operations. Since its initial development in 1950s and 1960s [41, 44], MD has widely been used to study processes at a molecular level. In the pharmaceutical industry, drug delivery and how drug molecules would interact with proteins and cells are two important subjects of research [45–47]. In the food industry, obtaining properties of biomaterials (e.g., lipids and carbohydrates) and developing predictive descriptions for physical mechanisms present in different processes are the focus of research [48–52]. In the oil and gas industry, thermodynamic and transport properties of

molecules, from small hydrocarbons to long polymers, are studied for applications such as catalytic cracking [53–56] and carbon capture and sequestration [57–60].

Nonetheless, considerable effort is required to extend the industrial applications of MD and provide accurate predictions. An example of such effort is the Industrial Fluid Properties Simulation Challenge (IFPSC) [61]. This competition is organized by Computational Molecular Science and Engineering Forum (CoMSEF) of different institutes and companies such as the American Institute of Chemical Engineers (AIChE) and National Institute of Standards and Technology (NIST) [61]. The aims of this competition are to drive improvements in molecular modeling and provide relevant simulation methodologies for industrial applications with the focus on verifying and validating simulation results with experiments [61]. This paves the way to progressively incorporate molecular simulation into solving industrial challenges and using in real-world applications. Since 2001, the computation of different properties of materials which are used extensively in chemical industries has been the focus of the IFPSC. Typical examples are the vapor pressure and heat of vaporization of acetone (2003-2004), the liquid-liquid equilibrium of dipropylene glycol dimethyl ether and water (2010), and the water/oil interfacial tension at high temperature and pressure (2016). The subject of the latest challenge in 2018 was to compute the shear viscosity of a branched hydrocarbon (2,2,4 trimethylhexane) at high pressures (up to 1000 MPa). This hydrocarbon is a glass-former and at high pressures, the shear viscosity increases significantly [62]. As shown by this challenge, many factors should be taken into account to obtain accurate predictions by MD [63–65]. This includes an appropriate methodology for calculating high shear viscosities with an acceptable statistical uncertainty and a correct description of the interactions between hydrocarbon molecules. Hence, up to now, there are still challenges that should be addressed to take full advantage of MD for industrial applications.

1.1. MOLECULAR DYNAMICS FOR COMPUTING TRANSPORT PROPERTIES

In MD, equations of motion can be integrated provided that the total force exerted on each atom is known. This total force is the sum of interactions between all atoms in the simulation box. These interactions can be computed from quantum mechanics. Alternatively, these interactions can effectively be computed from a classical force field. In the latter approach, simple functional forms are assumed for intramolecular and intermolecular potentials [36]. For instance, intermolecular potentials can be described by the 12-6 Lennard-Jones and the Coulomb's law, and intramolecular potentials can be described by quadratic po-

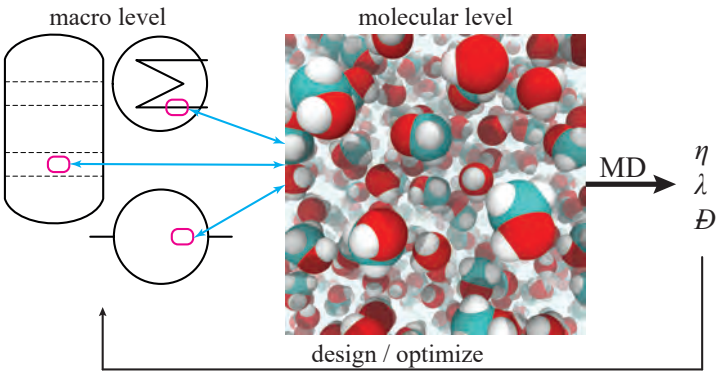

Figure 1.2: MD simulations can be used to compute viscosities (η), thermal conductivities (λ), and diffusivities ($Đ$) at different temperatures and pressures. These computations can help the design and optimization of industrial applications.

tentials for bond-stretching and bond-angle bending [35, 36]. Other contributions can be added to improve the accuracy of the force field. The use of simple functional forms in a classical force field significantly decreases the computational requirements of performing MD, compared to the computational requirements of using quantum mechanics calculations. Therefore, performing long simulations (of the order of hundreds of nanoseconds) of complex molecular systems consisting of thousands of atoms, such as polymers [66], proteins [67, 68], carbohydrates [69], and ionic liquids [70, 71], are feasible with current computers, while quantum mechanics calculations are limited to several hundred atoms within small timescales (on the order of picoseconds) [72]. The accuracy of results obtained from quantum mechanics depends on the choice of the method (e.g., Density function theory) used for solving the governing equations and the specified parameters (such as the basis set). The accuracy of computed properties from molecular mechanics depends on the classical force field used to describe intramolecular and intermolecular interactions. Incompatibility of force field parameters for different molecular systems and different required properties is the main reason for inaccurate results [69, 73]. To address this issue, force fields have been developed for specific groups of molecules and applications. These force fields are parameterized on the basis of quantum mechanics calculations (e.g. Density Functional Theory [74]) and/or reproduction of specific experimental data (e.g. vapor-liquid equilibria). As more data are used for parameterization of force fields, better estimation of properties can be obtained. Some of the well-known force fields are: Transferable Potential for Phase Equilibria (TraPPE) [75–81], Optimized Potential for Liquid Simulations-All Atom (OPLS-

AA) [82–85], Assisted Model Building with Energy Refinement (AMBER) [86–89], Chemistry at HARvard Macromolecular Mechanics (CHARMM) [90, 91], Universal Force Field (UFF) [92]. More information on force field parameterization can be found in literature [93–97].

At each timestep of an MD simulation, the equations of motions are solved, and positions and velocities of all atoms as well as forces between atoms are computed. From the resulting trajectories, other properties of the system such as the temperature and pressure can be computed [36]. By sampling a property (A) over an observation time of t_{obs}, the time average of the observed property is equal to [36]:

$$\langle A \rangle = \frac{\int_0^{t_{\text{obs}}} \mathrm{d}t \cdot A}{t_{\text{obs}}} \tag{1.2}$$

If the simulation is performed for a long time and the phase space is sufficiently sampled, the computed time average approaches the experimentally observable macroscopic property.

Two main methods are available for computing transport properties using MD: equilibrium (EMD) or nonequilibrium (NEMD) simulations. In EMD, a transport coefficient (γ) is related to the integral of time-correlation function of a dynamical variable $\dot{A}$ [35, 36, 98, 99]:

$$\gamma = \int_0^{\infty} \left\langle \dot{A}(t)\dot{A}(0) \right\rangle \mathrm{d}t \tag{1.3}$$

where the angle brackets $\langle \ldots \rangle$ denote an ensemble average. Eq. (1.3) is called the Green-Kubo relation [8, 35, 36, 42, 99]. The corresponding variables $\dot{A}$ for the diffusion coefficient, viscosity, and thermal conductivity are the velocities of molecules, the components of the stress tensor, and the components of the energy current (heat flux), respectively [36, 99]. An equivalent method for obtaining transport coefficients from EMD is the Einstein method [36, 98]:

$$\gamma = \lim_{t \to \infty} \frac{\left\langle (A(t) - A(0))^2 \right\rangle}{2t} \tag{1.4}$$

where the linear relation between time (t) and the mean-squared displacement (MSD) of the dynamical variable $(A(t) - A(0))^2$ yields the corresponding transport coefficient [36]. The linear relation of Eq. (1.4) is valid at timescales where the slope of MSD as a function of time is unity in a log-log plot [35, 36]. This criterion is often used to specify the minimum length of the simulation for obtaining transport properties with the Einstein method. Such a criterion is missing from the conventional Green-Kubo method, where the tail of the time-correlation functions very slowly converges towards zero regardless of the simulation length [100, 101]. While this issue has recently been addressed by the time-decomposition method proposed by Maginn and co-workers [102, 103], from a

practical point of view the Einstein method has an advantage over the conventional Green-Kubo method. In NEMD, the response of the system to external flows or driving forces yields the transport properties [36]. This method uses the definition specified earlier for transport properties, i.e., Eq. (1.1). Because the sizes in MD are small (on the order of nanometers), the applied driving forces (or gradients) are significantly larger than the forces which the system experiences on the macroscopic scale. Properties computed from NEMD may depend on the applied driving force and extrapolation to a zero force is then required [104]. At large external driving forces, the thermostat for controlling the temperature of the system may interfere with the motion of molecules and may cause partial phase separation [105]. This artifact forms stream phases of different species similar to the opposing traffic lanes on a road, leading to unrealistically large diffusion coefficients [18, 105–107]. Therefore, EMD is usually preferred. However, EMD may not be as effective as NEMD for studying some specific phenomena with slow response and large background thermal noises, causing large statistical uncertainties in computed properties [104, 108–110]. Another advantage of NEMD is the possibility of investigating linear and nonlinear responses of the system to a range of external driving forces [99, 107]. A representative example of NEMD is the study of membrane separation systems at the microscopic scale. This is due to the inefficient sampling of permeation of molecules through channels with high free energy barriers by using EMD simulations, because molecules tend to stay for a long time at low free energy sites [35, 53]. Many studies have used NEMD simulations to investigate water desalination [111–113] and gas separation systems [114, 115] by using nanoporous materials.

In EMD simulations, the conventional method for calculating the time averages (Eq. (1.2)) for the Green-Kubo (Eq. (1.3)) and Einstein (Eq. (1.4)) relations uses a fixed sampling frequency [35, 36]. This is not an efficient approach for systems with a broad range of dynamic timescales [116]. Low-frequency sampling may result in missing fast-decaying correlation functions, while high-frequency sampling requires a large amount of computational resources for storing and postprocessing large data files [117]. The sampling efficiency can be improved by using methods with adjustable sampling frequency, such as the multiple-tau correlator [116] and the order-n algorithm [35, 117]. These methods can efficiently capture both slow and fast dynamics while keeping the computational requirements low [116, 117]. Because not all these methods are available in all MD software packages, there is a clear need for implementing these advanced methods.

Typical MD simulations are performed for systems consisting of hundreds to thousands of molecules. The large computational requirement is the main limitation on the number of molecules. Still, this number is orders of magni-

tude smaller than the thermodynamic limit. Although periodic boundary conditions are used in MD simulations to mimic the presence of an infinite number of molecules, computed properties show dependency on the size of the simulation box. Some studies have already reported the system-size dependency of self-diffusivities [118, 119], thermal conductivities [120], activity coefficients [121], chemical potentials [122], and Kirkwood-Buff coefficients [123–125]. However, the finite-size effects of mutual diffusion coefficients have not been investigated despite being used in many MD studies. Hence, it is crucial to investigate the finite-size effects of transport properties in addition to improving the efficiency of the simulations.

The aim of this thesis is to address the challenges mentioned above for the methodology of computing transport properties, and taking into account finite-size effects. The focus of this thesis is on EMD. However, due to the advantage of NEMD over EMD for studying membrane separation systems, NEMD will be used for investigating water desalination applications using nanoporous zeolite nanosheets. For computation of transport properties of bulk fluids using EMD simulations, a tool is developed for the users of the MD software package LAMMPS [126]. The state-of-the-art order-n sampling technique is used to obtain transport properties at a minimum computational requirement [35, 117]. This tool can be used by other researchers to compute transport properties in an efficient and consistent way. This tool enables the study transport properties of fluids at different conditions and it can be used to develop more complex predictive models for these properties based on the molecular structure of constituent molecules of a fluid. The developed tool can be used to efficiently investigate finite-size effects of transport properties and propose a correction for the finite-size effects of binary mutual diffusion coefficients. The developed correction eliminates the need to perform simulations for multiple system sizes and extrapolate to the thermodynamic limit. Finally, force field-based MD simulations cannot provide accurate results by using inaccurate force fields, regardless of the efficiency of simulation techniques. If an accurate force field is not available for a system, general or universal force fields can be reparameterized for this specific application. This adjustment, however, requires a profound understanding of atomic/molecular interactions to identify relevant parameters which should be refitted. Experimental data or quantum mechanics calculations can be used to refit these properties. In this thesis, two examples of refitting intermolecular and intramolecular force field parameters are investigated for: crown-ethers and carbohydrate molecules, respectively.

This thesis helps to expand the application of Molecular Dynamics in industry and the scientific community. The implementation of the OCTP tool, which computes transport properties during the simulation, provides a consis-

tent foundation for a consistent computation of transport properties. Postprocessing of large data files is no longer required for obtaining transport properties of viscous and complex fluids. By improving the efficiency of the computation methods and studying the finite-size effects of computed properties, one can predict transport properties at conditions that could not be achieved previously. Because non-ideality of mixtures and fluids are included in MD, computed transport properties from these simulations can be used to develop predictive models based on the molecular structure. Recent studies have focused on such investigations for diffusion coefficients [40, 127–130], shear viscosities [39, 62, 131–133], bulk viscosities [132], and thermal conductivities [132, 134, 135]. These investigations can be extended further by using the results of this thesis. Furthermore, as indicated in Fig. 1.2, investigating transport properties of working fluids in industrial processes can provide improvements in efficiency and yield by computing transport properties of novel fluids prior to performing experiments.

1.2. OUTLINE OF THIS THESIS

This thesis is organized in two main parts: (1) methodology and (2) force field improvement.

The aim of the first part is to form the basis for the methodology to compute transport properties. In Chapter 2, NEMD simulations are discussed for computing the permeability of fluids through nanoporous materials. In this case, the permeation of water and salt ions through nanoporous zeolite nanosheets is studied for water desalination applications. The water permeability and salt rejection are obtained for a set of zeolite nanosheets, and a relation between the water permeability and the characteristics of the zeolite nanosheet is established. The water permeability depends on the pore size and pore density of the zeolite as well as the free energy landscape inside pores. These results help to define a set of guidelines for future theoretical and experiential studies on water desalination using zeolite nanosheets. In Chapter 3, the computation of transport properties in EMD simulations are described in detail and the Einstein relations for various transport properties are defined. The transport properties considered here are self-diffusivities, Maxwell-Stefan and Fick mutual diffusivities, shear and bulk viscosities, and thermal conductivities. These relations have been implemented as a plugin for LAMMPS. To illustrate how this plugin can be used, transport properties of a binary mixture of water-methanol is studied by performing a set of EMD simulations. The method explained in this chapter is used in the rest of this thesis. The finite-size effects of transport properties of a Lennard-Jones fluid close to the critical point are also investigated in the same chapter. In Chapter 4, the finite-size effects of the diffusion coefficients are studied. While the shear viscosity does not show any system-size dependency, an an-

alytic correction to the finite-size self-diffusivity have been proposed previously [118]. Here, this correction is examined for a large number of mixtures and its limitations are investigated. This correction paves the way to study the finite-size effects of mutual diffusion coefficients. Based on this, an empirical correction is proposed to correct finite-size effects of binary mutual diffusion coefficients. In Chapter 5, a new method is proposed to compute the shear viscosity from finite-size self-diffusivities. As the shear viscosity does not show any system-size dependency, the analytic correction for finite-size self-diffusivities can be used to obtain the shear viscosity of a fluid from the difference in the self-diffusivities of two system sizes.

The aim of the second part of this thesis is to improve currently available force fields for an accurate prediction of transport and thermodynamic properties of two groups of molecules: (1) crown-ethers and (2) carbohydrates. Crown-ethers are a class of cyclic molecules with ether groups in their ring structure. As a potential application for these molecules would be natural gas and syngas treatment, the Transferable Potential for Phase Equilibria (TraPPE) [75, 76, 78, 136] is an appropriate force field. Currently, the TraPPE force field is only available for chain-ether molecules such as glymes [78]. The difference in the internal structure of a chain and a ring molecule results in inaccurate predictions of crown-ether properties. In Chapter 6, the dihedral angle torsion parameters of the TraPPE force field are refitted to energy profiles obtained from quantum calculations. The new force field parameters provide a significant improvement in estimated transport and thermodynamic properties of crown-ethers over the original TraPPE force field. This improved force field can be used to investigate the potential of porous liquids (mixtures of crown-ethers and molecules with permanent pores in their structure) for gas treatment applications. In Chapter 7, the OPLS force field is examined for providing accurate estimates of both transport and thermodynamic properties of aqueous solutions of carbohydrates. Due to the strong hydrogen bonds between the OH groups in carbohydrates and water molecules, the OPLS force field cannot provide accurate predictions for water-carbohydrate interactions at high sugar concentrations. To address this issue, the Lennard-Jones and electrostatic interactions of the OPLS force field are scaled to improve the predicted interactions for water-sucrose mixtures. The transferability of such scaling is verified by examining the modified OPLS force field for water-glucose mixtures.

2

Non-Equilibrium Molecular Dynamics Investigation of Water Desalination in Nanoporous Zeolites

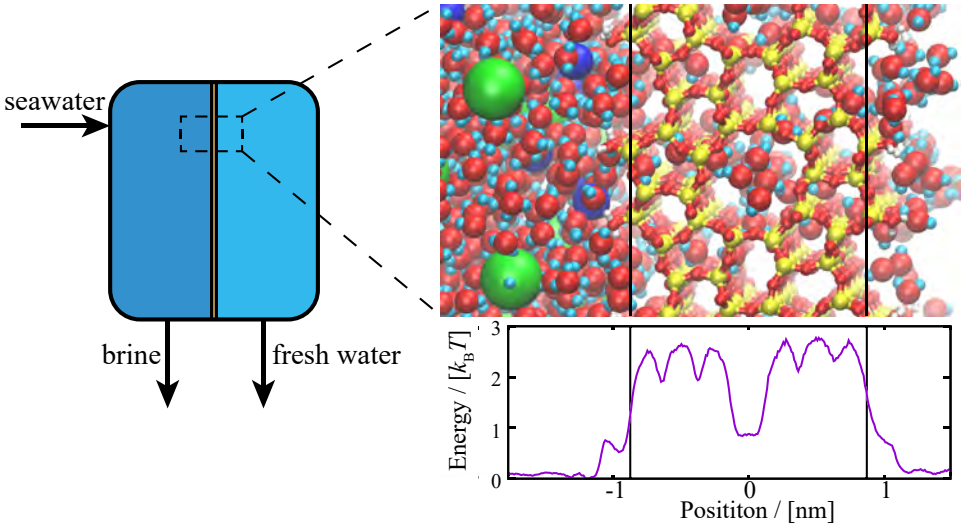

This chapter is based on the paper: S.H. Jamali, T.J.H. Vlugt, and L.-C. Lin, *Atomistic Understanding of Zeolite Nanosheets for Water Desalination.* Journal of Physical Chemistry C, **121**, 11273-11280 (2017) [137].

2.1. INTRODUCTION

In the past decades, the need for water desalination has increased significantly [138] and this need will become more pronounced due to the continuing population growth and economic development [139]. Amongst various methods to produce fresh water from saline sources, reverse osmosis (RO) is currently the most prevalent approach with a global market share of approximately 60% [138], and polyamide-based RO membranes have been widely used [140–142]. The associated energy consumption and the cost of the process largely depend on the permeability of the RO membrane [142]. Cohen-Tanugi et al. [143] have recently shown that there will be 44% reduction in the number of pressure vessels and 15% reduction in the energy consumption of the Sea Water Reverse Osmosis (SWRO) desalination, provided that the permeability of membranes is improved threefold compared to the current polyamide-based membranes. The need for more fresh water requires new membranes to increase the flux of RO membranes while maintaining excellent salt rejection to make this process more energy and cost efficient. Recently, many types of novel materials have been investigated experimentally and/or computationally. These materials have shown great promise as membranes in RO water desalination such as nanoporous graphene [111, 113, 144–147], graphene oxide [112, 146–148], covalent triazine frameworks (CTFs) [149], MoS_2 [150], and graphyne [151–153]. A common feature of these candidates is the ultrathin-film nature of the material, highlighting the need for discovering ultrathin-film membranes. Furthermore, well-defined pore structures in these membranes can effectively block salt ions passage, leading to outstanding salt rejections.

Recently, considerable attention has been paid to layered zeolites with a thickness varying from one to several unit cells [154–157]. These systems possess short diffusion lengths, potentially overcoming diffusion and mass transfer limits. Various types of zeolites have been synthesized in the nanosheet form with different possible inter-layer linkers [156, 158–161] with an aim at targeting various catalytic systems such as isomerization and hydrocracking [162–164], and selective formation of molecules [165–167]. Although zeolite nanosheets have been also considered for adsorption [168–170] and membrane [171] separation systems, zeolite nanosheets specifically as RO membranes for water desalination have been greatly overlooked in the literature. The small thickness of layered zeolites (i.e., short diffusion distance) along with their excellent chemical and physical resistance make zeolite nanosheets a promising type of RO membrane materials in water desalination. It is also anticipated that the hydrophilic nature (i.e. silanol (SiOH) groups on the surface) of zeolite nanosheets can render these membranes better resistant to biofouling [172]. Moreover, more than 230 distinct zeolite topologies have been identified and included in the International

Zeolite Associations (IZA) database to date [173], while millions more have been theoretically predicted [174–177]. Such a large materials space further provides tremendous opportunities for zeolite membranes in water desalination.

Despite the potential of zeolite nanosheets in water desalination applications, no experimental investigation of zeolite nanosheets as RO membranes has been reported. Experimental studies on desalination using zeolites focused primarily on bulk zeolites [178–188] or thin-film nanocomposites (TFN) in which zeolite nanoparticles are incorporated in thin film polyamide/polymer membranes [189–194]. These systems are inherently different from zeolite nanosheets, and these experimental studies are also limited to very few zeolites. A similar situation applies to computational studies reported to date in the literature. The computational investigation of zeolite nanosheets for their desalination performance remains limited. While some studies attempted to address the diffusion of water molecules or salt ions in bulk zeolites [195, 196], few were carried out to study zeolites in a form of nanosheet membrane [197–199]. Despite the vast material space of zeolites, only three zeolites (i.e., MFI, FAU, and LTA) have been investigated [197].

To push forward the development of zeolite nanosheets for water desalination applications, it remains of utmost importance to establish a fundamental structure-performance relationship, as an important basis for the optimal design of zeolite RO membranes. To achieve this, systematically studying a number of materials with a wide range of structural characteristics is needed. In this chapter, state-of-the-art Molecular Dynamics (MD) techniques are used as an efficient approach to address this missing knowledge.

This chapter is organized as follows. In Section 2.2, the details of simulations are described. In Section 2.3, the results obtained from MD simulations are presented and potential zeolite nanosheets are selected for water desalination. The findings are summarized in Section 2.4.

2.2. SIMULATION DETAILS

Non-equilibrium MD (NEMD) simulations are used to investigate the water permeability and salt rejection of zeolite nanosheet membranes. Simulations are carried out in LAMMPS, an MD simulation package [126], version released on 30 October 2014. A solution of water and salt is pressurized by a piston to push water molecules through a membrane. The position of water molecules and salt ions is recorded during the simulation, which is postprocessed to calculate the water permeability and salt rejection of that zeolite nanosheet. A sample chart of water permeation through an MFI nanosheet membrane along with three typical snapshots of the system is shown in Fig. 2.1. This figure shows the evolution of the number of water molecules in the feed (blue), membrane (green), and

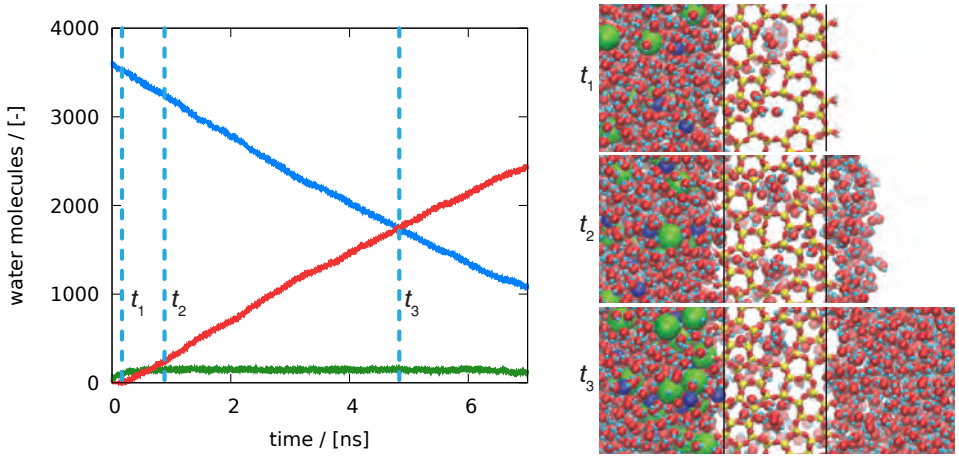

Figure 2.1: Number of water molecules in the feed (blue), inside the membrane (green), and on the permeate side (red) as a function of time for a typical simulation. Snapshots of the simulation at three time steps of t_1, t_2, and t_3 are shown. The vertical black lines indicate the surface of the membrane according to the position of the furthest silicon atom from the center of the zeolite.

permeate (red) during the simulation. As water permeates through the membrane, the number of water molecules in the membrane reaches a constant and water molecules accumulate on the permeate side. The water flux through the membrane is calculated from the slope of water accumulation on the permeate side. The water flux is computed when at least a single layer of water molecules is present on the surface of the permeate and the number of permeated water molecules is less than that of the feed. This corresponds to a time span between time t_1 and t_2 in Fig. 2.1. The water permeability (K/L) of a membrane is defined as the water flux divided by the pressure difference (i.e., the exerted pressure minus the osmotic pressure) and the cross-sectional area:

$$\frac{K}{L} = \frac{J}{A \cdot \Delta P} = \frac{J}{A \cdot (P - \Pi_{\text{osmotic}})} \tag{2.1}$$

where J is the water flux through a membrane. A is the area of the membrane. P and Π_{osmotic} are the applied transmembrane pressure and the osmotic pressure of the solution, respectively. The salt rejection is defined as the ratio of the number of passed ion pairs to the initial number on the feed side when half of the water molecules permeate to the permeate side (corresponding to time t_3 in Fig. 2.1).

The initial configuration of water molecules and salt ions in the simulations is constructed in several steps. A zeolite slab with a total thickness of approximately 25 Å (within a range of 20 to 30 Å) in the permeation direction is used as the active

reverse osmosis membrane layer. The surface of this zeolite slab is functionalized with hydroxyl (OH) groups, i.e., all dangling bonds of silicon atoms are saturated with hydroxyl groups. The silanol (SiOH) group is one of the most abundant surface functionalizing groups of zeolites. The hydrogen bond of the silanol groups provides the required interconnection force to stack zeolite nanosheets to construct a controlled multilayer zeolite nanosheet [156, 157]. An electrically neutral mixture of sodium and chloride ions along with water molecules is added to one side of the membrane by using the Autoionize plugin in VMD [200]. This saline solution with a concentration of 1.0 M, almost twice the salt concentration of seawater, is employed to achieve better statistics of the ability of membranes to reject salt ions within the short MD time scale (i.e., on the order of 10ns). A similar concentration has been also adopted by other computational studies [111, 149, 197]. A piston is placed on the feed side, and a constant force is applied on the piston to modulate the transmembrane pressure. The applied force exerts an average constant pressure of 300 MPa on the solution. The high pressure applied on the piston reduces the sensitivity of the driving force to the feed concentration and the water flux subsequently remains almost constant while the feed is depleted. Furthermore, applying such a high pressure is required to achieve more accurate statistics within the short MD timescale.

The force fields used in the simulations are chosen to be fully compatible between the membrane, water molecules, and salt ions. The potential parameters for both the inside and the surface of the zeolite nanosheet are adopted from the work of Emami et al. [201]. This force field has been applied to study zeolites with a wide range of hydroxyl group densities (the SiOH density on the surface of a zeolite) and pHs. Water molecules are modeled using the three-site TIP3P model. The force field for ions is taken from the work of Joung and Cheatham [202] with parameters compatible to the TIP3P model.

All short-range non-bonded interactions are truncated and shifted to zero at a cutoff radius of 12.0 Å. For long-range Coulombic interactions, the Particle-Particle Particle-Mesh (PPPM) method with a relative accuracy of 10^{-6} is used. For dissimilar atoms, the Lorentz-Berthelot mixing rules are applied [36]. The 1-4 intramolecular non-bonded interactions between atoms of hydroxyl groups on the surface of the membrane are included and scaled by 0.5 and 0.833 for Lennard-Jones and Coulombic interactions, respectively [201]. The force field parameters used for the simulations are listed in the Supporting Information of the work of Jamali et al. [137]. For simplicity, the bulk part of the studied zeolite nanosheet (i.e., non-surface part) is assumed to be rigid. Therefore, the silicon and oxygen atoms do not move during the simulation, although in experiments the structure of bulk zeolites may slightly vary while loaded with water molecules [203]. The effect of structural flexibility on the separation performance of zeolites

has been found to be negligible [197], and it is therefore anticipated that the outcome will not be significantly affected by assuming a rigid framework structure. Furthermore, the atomistic structure of the bulk part of zeolites are taken from the IZA database [173]. The equations of motion for water molecules, sodium and chloride ions, and atoms of the hydroxyl groups on the surface of the membrane are integrated using the velocity-Verlet algorithm [36]. The Nosé-Hoover thermostat is used to regulate the system's temperature at 298 K in an NVT ensemble whose effects on the diffusivity of water molecules in zeolites have been found to be insignificant [196]. The rigid bonds and bond angles of water are considered by the means of the SHAKE algorithm [36]. Four independent simulations with uncorrelated initial configurations have been carried out for each studied zeolite.

2.3. RESULTS AND DISCUSSION

A set of NEMD simulations for a total number of 27 zeolite structures were carried out to investigate saline water permeation through zeolite nanosheets. Out of this number of zeolites, 15 zeolites have one-dimensional channels, 8 zeolites have multi-dimensional channels, and 4 have cage-containing channels that connects cages to each other. All these zeolites, presented in Table 2.1, are adopted from the IZA database [173]. For simplification, only structures with an orthorhombic unit cell are considered. Such unit cells can be used in a rectangular simulation box with periodic boundaries. The pore-limited diameter (PLD or d_f) of these zeolites, which represents the diameter of the largest sphere that can transverse the channel, varies between 4.0 and 7.5 Å. It should be noted that a water molecule has a kinetic diameter of approximately 2.8 Å; water molecules are therefore less likely to permeate through channels with PLDs smaller than or close to this value [204]. Generally speaking, the transport properties of a zeolite membrane can be a function of various geometrical parameters, some of which are presented in Fig. 2.2 for a unit cell of a schematic zeolite. The PLD, however, is predicted to be of utmost importance for the diffusion properties such as the water permeation rate [205]. All results of the simulations including the permeabilities and salt rejections are reported in the Supporting Information of the work of Jamali et al. [137].

2.3.1. WATER PERMEABILITY

In Fig. 2.3, the water flux per cross-sectional area is shown as a function of the PLD. A connection between water flux and the PLD is found but it is rather scattered. As the density of channels per unit area varies from one zeolite to another, it is more sensible to take the number of channels per unit area into account. As expected, the water permeability per channel shows a more pronounced corre-

Table 2.1: The geometric characteristics of investigated zeolites. The characteristics are obtained from the IZA database [173]. d_f and D_i are the PLD and the largest included sphere diameters, respectively. d_{min} and d_{max} are the minimum and maximum diameter of the channel, respectively. The width (thickness) of the zeolites are multiples of the unit cell in the direction of permeation (channel direction). These characteristics of zeolites are schematically illustrated in Fig. 2.2.

name	channel dimension	channel direction	pore density	D_i	d_f	d_{min}	d_{max}	width
[-]	[-]	[-]	[#/nm^2]	[Å]	[Å]	[Å]	[Å]	[Å]
JRY	1-D	[0 1 0]	1.42	4.59	4.40	4.1	5.9	24.5
AEL	1-D	[1 0 0]	0.80	5.64	4.63	4.0	6.5	24.9
EUO	1-D	[1 0 0]	0.43	7.00	4.99	4.1	5.4	27.8
PSI	1-D	[1 0 0]	0.46	5.79	4.85	5.0	5.6	24.8
TON	1-D	[0 0 1]	0.79	5.71	5.11	4.6	5.7	26.3
MTT	1-D	[1 0 0]	0.80	6.19	5.07	4.5	5.2	26.3
MFS	1-D	[1 0 0]	0.73	6.81	5.37	5.1	5.4	22.6
GON	1-D	[0 0 1]	0.58	6.32	5.45	5.4	6.8	26.3
MRE	1-D	[1 0 0]	0.68	6.36	5.59	5.6	5.6	24.8
SSY	1-D	[0 0 1]	0.63	7.10	5.75	5.0	7.6	26.3
VET	1-D	[0 0 1]	0.59	6.39	5.98	5.9	5.9	24.7
EZT	1-D	[1 0 0]	0.73	6.57	6.13	6.5	7.4	20.5
SAF	1-D	[0 0 1]	0.52	6.66	6.19	5.6	8.5	25.0
OSI	1-D	[0 0 1]	0.58	6.66	6.28	5.2	6.0	26.3
ATS	1-D	[0 0 1]	0.70	7.30	6.82	6.5	7.5	26.3
FER	2-D	[0 0 1]	0.74	6.31	4.69	4.2	5.4	22.6
MFI	3-D	[1 0 0]	0.77	6.36	4.70	5.1	5.5	20.1
MFI	3-D	[0 1 0]	0.76	6.36	4.46	5.3	5.6	19.7
NES	2-D	[1 0 0]	0.63	7.04	5.07	4.8	5.7	26.1
NES	2-D	[0 1 0]	0.67	7.04	5.07	4.8	5.7	27.8
MEL	3-D	[1 0 0]	0.73	7.72	5.19	5.3	5.4	20.3
SFG	2-D	[0 0 1]	0.62	6.96	5.38	5.2	5.7	26.1
IWR	3-D	[0 0 1]	0.71	7.48	5.91	5.8	6.8	25.4
BEC	3-D	[0 0 1]	0.61	6.95	6.09	6.3	7.5	26.0
BEC	3-D	[1 0 0]	0.60	6.95	6.09	6.0	6.9	25.5
SAO	3-D	[0 0 1]	0.55	8.64	6.79	7.0	7.0	21.9
KFI	3-D (cage)	[0 0 1]	1.16	10.67	4.04	3.9	3.9	18.6
LTA	3-D (cage)	[0 0 1]	0.70	11.05	4.21	4.1	4.1	23.8
OBW	3-D (cage)	[0 0 1]	0.47	9.26	5.18	5.0	5.0	27.8
FAU	3-D (cage)	[0 0 1]	0.34	11.24	7.35	7.4	7.4	24.4

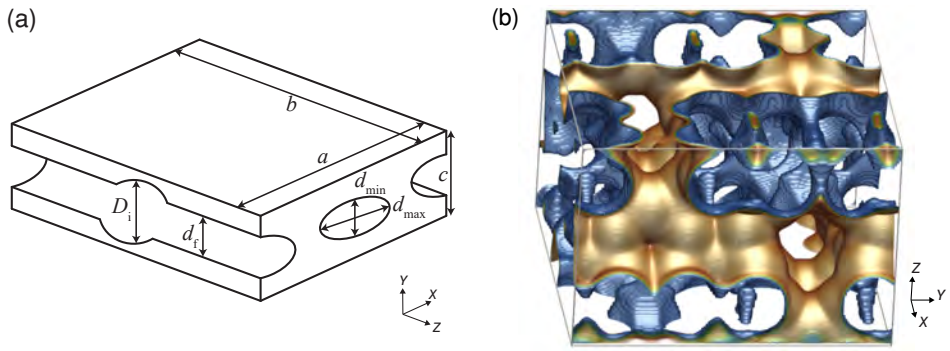

Figure 2.2: (a) Schematic representation of a 1-dimensional zeolite unit cell with a pore density of 2 channels per unit cell in the *xy* plane. d_f and D_i are the PLD and the largest included sphere diameters, respectively. d_{min} and d_{max} are the minimum and maximum diameter of the channel, respectively. (b) MFI, a zeolite with multi-dimensional channels, has a interconnected network of straight and zig-zag channels in the *y* and *x* directions that are shown in yellow. Similar structural characteristics can be defined for other zeolites.

lation with the PLD. Overall, it can be seen that the water permeability generally increases with an increase in the PLD. As shown in Fig. 2.3, the water permeability of one layer of zeolite nanosheet can be as high as 40 [lit/day/cm^2/MPa]. For comparison, a layer of nanoporous graphene functionalized with hydrogen or hydroxyl groups have water permeabilities up to 60 and 140 [lit/day/cm^2/MPa] [111], respectively. Two-dimensional covalent triazine frameworks (CTF) show also high water permeability up to 65 [lit/day/cm^2/MPa] depending on the pore area of the CTF structure [149]. Zeolite nanosheets have similar water permeabilities compared to other novel ultrathin-film membranes, which again demonstrates the importance of this type of membranes. In practice, several layers of these two-dimensional sheets are superimposed, resulting in multi-layered structures, or one layer of several unit cells are used [157]. A multi-layered structure can potentially lead to improved structural strength and better ability to reject salt but, at the same time, reduce the water flux [113]. If the water permeability decreases reciprocally with the thickness of the effective membrane [197], a currently available zeolite nanosheet of 100-nm thickness may have a permeability as high as 1.3 [lit/day/cm^2/MPa], which is still a significant improvement compared to the conventional systems with water permeabilities, ranging from 0.03 to 0.2 [lit/day/cm^2/MPa] [142]. This means that a substantial reduction in the number of pressure vessels and energy consumption can be achieved [143]. Nonetheless, to advance membranes using zeolite nanosheets, developing thinner stacked membranes should be an important subject of future studies.

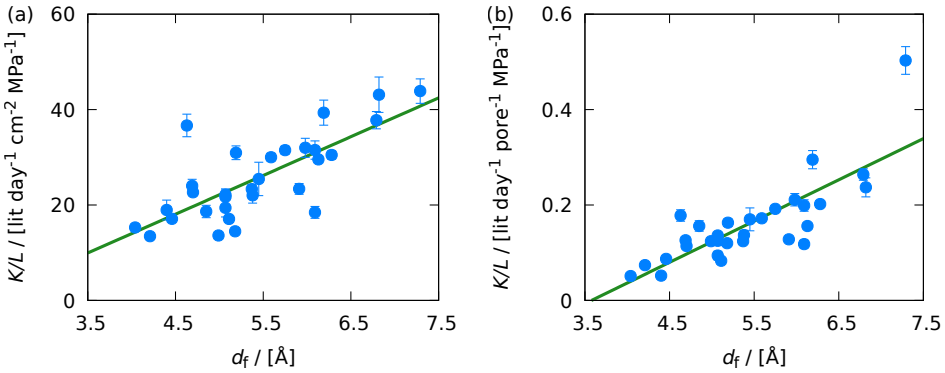

Figure 2.3: Water permeability (K/L) of studied zeolites (a) per area and (b) per channel as a function of the PLD. The permeability per pore has units of number of water molecules permeated per ns, per pore, per pressure difference. The lines serve as guides to the eye and represent linear regression fits to the data.

Although a relation between the water permeability and the PLD has been established (Fig. 2.3), a simple descriptor is still unable to fully explain water permeation in the membranes (i.e., notable variation in permeabilities at a fixed PLD). To better understand this variation, the free energy landscape of water in zeolites was computed, which is a critically determining factor to describe the transport of water molecules. The average density of water at each cross section of the membrane, computed from the configurations stored during the simulations, can be used to obtain the free energy landscape of water inside a zeolite nanosheet. The relative probability/frequency of sampling oxygen atoms of water at a cross section perpendicular to the flow provides the information required for obtaining the free energy landscape [43, 206]:

$$A = -k_B T \cdot \ln\left(\frac{P(q)}{P_{\text{ref}}}\right) \tag{2.2}$$

where A is the free energy, k_B and T are the Boltzmann constant and temperature, respectively. $P(q)$ is the probability of observing an oxygen atom of water at a specific cross section, q. The reference position is where the minimum energy occurs. The free energy landscape of several zeolites with one-dimensional channels which have permeabilities different than the average permeability of a PLD is shown in Fig. 2.4. The zeolites which have higher water permeabilities than the average are AEL, PSI, and SAF with pore-limited diameters of 4.63 Å, 4.85 Å, and 6.19 Å, respectively. The zeolites with lower water permeabilities are JRY, TON, and EZT with PLDs of 4.40 Å, 5.11 Å, and 6.13 Å. For the zeolites

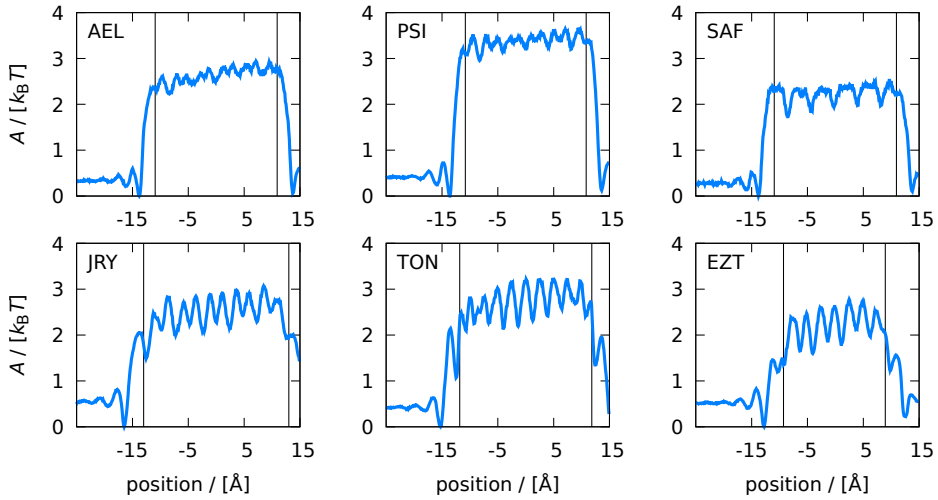

Figure 2.4: Free energy (A) profiles of zeolites with one-dimensional channels. The profiles in the upper panel have large permeabilities while those in the lower panel have smaller permeabilities than the average at a given PLD. The vertical lines indicate the surfaces of the membranes using the position of the furthest silicon atom from the center. The minimum free energy is shifted to zero.

with the PLDs between 4.40 Å and 5.11 Å, AEL has the highest water permeability followed by PSI, TON, and JRY. Moreover, SAF has a water permeability per channel twice that of EZT despite the fact that both of these zeolites have similar PLDs. Overall as shown in Fig. 2.4, these membranes possess a large free energy barrier for water permeation on their surfaces, filled with silanol (SiOH) groups. Interestingly, this suggests that such a barrier is not evidently correlated to the difference in water permeabilities and the density of hydroxyl groups may not have a pronounced influence on the water permeability. Instead, the transport barrier inside the membrane appears to control the diffusion of water molecules. Membranes with higher permeabilities are those structures with the lowest free energy barrier inside the channel (AEL and PSI vs. JRY and TON) along with a smaller number of barriers or jumps (EZT vs. SAF). For zeolites with multi-dimensional channels, a similar behavior can be observed as well, but the free energy landscape is more complex than zeolites with 1-dimensional channels due to the interconnected channels in different directions (Fig. 2.2).

It is worth mentioning that FAU (with a PLD of 7.35 Å) has the smallest free energy barrier (1.5 $k_B T$) on its surface and inside, which makes its large permeability per channel possible (see Fig. 2.3). However, since the pore density per area of FAU is half of the density of ATS, whose PLD is comparable to FAU's PLD

but possesses a higher transport free energy barrier, the permeability per area of these two zeolites are the same. Likewise, it was shown that AEL and PSI have a high water permeability per channel due to their favorable free energy landscape, but AEL has a two times more water permeability per area than PSI because of its larger pore density (0.80 vs. 0.46 pore/nm^2). Hence, these results clearly suggest that the density of channels plays an important role in quantitatively determining water flux in zeolites.

2.3.2. SALT REJECTION

To enable effective desalination, membranes have to be nearly semi-permeable (i.e., blocking salt ions from passage). Sodium and chloride ions have first hydrated shell radii of 2.356 Å and 3.187 Å [207], respectively. These radii can be reproduced by the force field of salt ions and the TIP3P water molecule model [202], and they have been calculated to be 2.38 Å and 3.13 Å, respectively. Zeolites with PLDs larger than 6.4 Å (twice 3.187 Å) may not be appealing candidates for water desalination due to the possible permeation of both sodium and chloride. To quantify the salt rejection of a membrane, a criterion for quantifying the salt rejection of a membrane can be used. The criterion for this study is the number of passed ion pairs from the beginning of a simulation until the number of water molecules on both sides of the membrane is equal. This corresponds to the time when the lines for the number of water molecules in the feed and the permeate sides cross each other (Fig. 2.1). In Fig. 2.5, the salt rejection is shown as a function of the PLD of the zeolites. Zeolites with PLDs below 5.5 Å (between the first hydrated shell diameters of sodium and chloride) show a salt rejection very close to 100%. At this point, it should be pointed out that higher applied pressures normally lead to a relatively lower salt rejection. As pointed out previously, a high pressure of 300 MPa is applied herein to obtain better statistics within the time scale of an MD simulation. As a result, under practical conditions, salt rejection might be higher [111]. As a comparison, Cohen-Tanugi and Grossman [111] showed that a layer of nanoporous graphene can effectively hinder salt ions when the nanoporous graphene has a pore size of 5.5 Å (i.e., PLD = 5.5 Å). This value is similar to the value of maximum PLD obtained here. Similarly, comparing the result to other classes of materials, it was found that CTFs with an effective radius of approximately 3 Å exhibit salt rejections of 96% and 100% depending on the chemistry of the pores [149]. Accordingly, to effectively reject salt ions, a PLD ranging from 5.5 Å to 6.0 Å seemingly generally defines the limits on how large the PLD needs to be. Nonetheless, other factors (such as topologies and pore chemistries) could also affect the salt rejection.

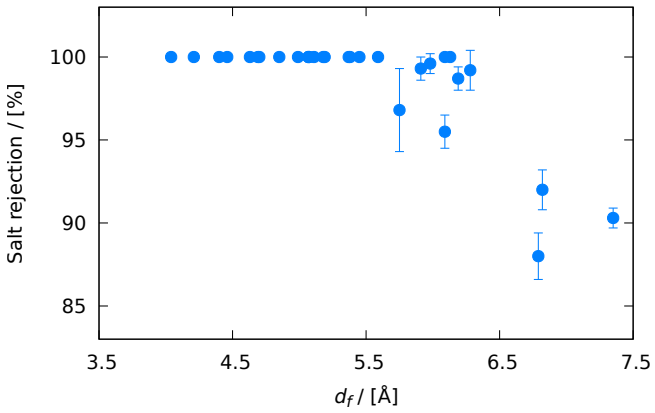

Figure 2.5: Salt rejection of the studied zeolite nanosheets as a function of the PLD.

In addition to the PLD criterion, the cross-sectional area of a zeolite channel—calculated from the area of an ellipse with major and minor radii equal to d_{max} and d_{min} (Fig. 2.2)—can be another factor to identify zeolites with high salt rejections. The area of the first hydrated shell of sodium and chloride are approximately 18 and 31 Å^2, respectively. It is anticipated that channels with cross-sectional areas less than 18 Å^2 can potentially block ions, resulting in a nearly 100% rejection rate. In contrast, zeolites with channel cross-sectional areas in the vicinity of 31 Å^2 or above may have a low salt rejection. From the MD simulations, it was found that all zeolites with a salt rejection less than 99% have a channel cross-sectional area larger than or equal to 30 Å^2. However, not all zeolites whose channel cross-sectional area is larger than 30 Å^2 show low salt rejection, so other factors and the energy barrier inside the channel against the ion transport play a role.

It is interesting to compare two specific zeolites: SSY and SAF. These zeolites have PLDs of 5.75 and 6.19 Å, respectively. Their one-dimensional channels have minimum widths of 5.0 and 5.6 Å, as well as maximum widths of 7.6 and 8.5 Å, corresponding to channel cross-sectional areas of 30 and 37 Å^2, respectively. SAF has a 25% higher water permeability than SSY due to its larger channel area and PLD. However, SAF is found to have a higher salt rejection (99%) than SSY (97%). This may seem less intuitive but this observation may be attributed to the effect of cages. The largest included sphere diameters (D_{i}) of SSY and SAF (i.e., the maximum diameter of a sphere that can be fitted in the pores of a zeolite; see Fig. 2.2) are 7.10 Å and 6.66 Å, respectively. Although both membranes have PLDs larger than the first hydrated shell diameter of sodium and smaller than

that of chloride, SAF has a similar included diameter compared to the hydrated shell of chloride. When a chloride ion and its hydrated shell permeate through SAF, the hydrated ions could fit tightly to the cage due to the strong interactions with the cage surface and therefore increase the overall transport barrier. Hence, chloride ions are anticipated to experience more resistance to permeation in SAF than SSY. This insight can be important to the design of novel zeolite nanosheet membranes, suggesting that the inclusion of cages with a right size may be exploited to manipulate membranes' salt rejection without sacrificing their water permeability.

Several zeolites that have been already synthesized in two-dimensional nanosheet forms are summarized in the review by Roth et al. [156]. According to the established structure-performance relationship, four of these two-dimensional zeolites appeal to be promising for water desalination: OKO, MWW, MFI, and FER. It is predicted that OKO has the highest water permeation among these zeolites due to the large PLDs of the two channels of OKO (5.1 Å and 5.9 Å) and their corresponding high pore densities (0.60 and 0.67 pore/nm^2). However, the salt rejection of OKO in the direction with a PLD of 5.9 Å might be slightly less ideal due to the rather large PLD together with a cross-sectional area of 31 Å^2 and an included diameter of 6.7 Å. These values are at the limit identified earlier for efficient salt rejection. Future investigations are needed to determine precisely the transport properties of this particular channel. Notwithstanding, the other direction possessing a PLD of 5.1 Å can provide a high water permeability while the smaller channel cross-sectional area (22.5 Å^2) can prevent the permeation of salt ions. It is important to note that the results obtained here are for hydrophobic zeolites without defects inside the membrane. Hydrophobic zeolites typically show a large infiltration pressure in the bulk structure [208]. The existence of defects or non-framework cations increases the hydrophilicity of a zeolite, which can increase the solubility of water while also potentially deteriorating diffusion properties [209]. Investigating zeolites with defects or non-framework cations is an important subject of future studies.

2.4. CONCLUSIONS

In this chapter, non-equilibrium Molecular Dynamics simulations were used to calculate the water permeability and salt rejection of 27 zeolites. The results clearly show that zeolite nanosheets possess promising separation performance, making them potential membrane candidates in water desalination. Furthermore, the results obtained herein have provided a set of guidelines for the design of novel reverse osmosis zeolite nanosheet membranes. Specifically, three important selection criteria and design principles for choosing appropriate zeolite nanosheets for water desalination were identified. First, a recommended zeolite

may have a large but smaller than 5.5 Å PLD. Channels with a larger PLD may still be promising for effective separations but other effects of the channel structure on salt rejection should be taken into account (e.g., the cross-sectional area and the shape of channels). Second, a larger channel density on the surface of zeolites is beneficial for the water permeation. Third, the salt rejection may be enhanced when the included cages have a comparable size to the first hydrated shell diameter of chloride (i.e., 6.5 Å). With this finding, one could potentially manipulate structures by designing channels with cages at a proper size to improve salt rejections without compromising water permeability.

3

Computation of Transport Properties in Equilibrium Molecular Dynamics Simulations

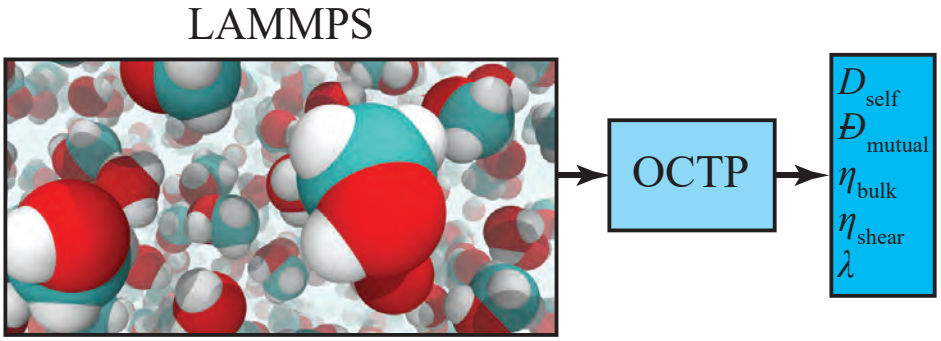

This chapter is based on the paper: S.H. Jamali, L. Wolff, T.M. Becker, M. de Groen, M. Ramdin, R. Hartkamp, A. Bardow, T.J.H. Vlugt, and O.A. Moultos, *OCTP: A Tool for On-the-fly Calculation of Transport Properties of Fluids with the Order-n Algorithm in LAMMPS*, Journal of Chemical Information and Modeling, **59**, 1290-1294 (2019) [210].

3.1. INTRODUCTION

Transport properties of liquids play an important role in many environmental and industrial applications [1, 14, 211]. The exponential increase in computational power in the past few decades, along with the development of robust open-source packages, such as LAMMPS [126], GROMACS [212], and NAMD [213], allows for the efficient use of Molecular Dynamics (MD) as a part of the design and optimization of various industrial processes. Typical examples are gas treatment [59, 214], carbon capture and sequestration [58, 60, 215, 216] and desalination using nanoporous membranes [112, 137]. Since there is a continuous demand for the prediction of transport coefficients, computational tools that are both accurate and easy-to-use are urgently needed [40, 127].

LAMMPS [126] is an open-source MD code distributed under the terms of the GNU Public License. It is one of the most widely-used MD packages because it features high degree of parallelization and size scalability as well as a modular structure, which promotes the development of new functionalities [217]. LAMMPS is equipped with generic functionalities to compute transport coefficients based only on the Green-Kubo method [217]. Despite the advantage over the Green-Kubo method, the Einstein approach combined with the order-n algorithm has not been implemented in this MD package.

To address this issue, a new plugin for LAMMPS has been developed for On-the-fly Calculation of Transport Properties (OCTP) of fluids using the Einstein relations combined with the order-n algorithm as presented in the work of Dubbeldam et al. [117]. The plugin can be used to compute the self and Maxwell-Stefan (MS) diffusivity (based on the Onsager coefficients), the shear and bulk viscosity, and the thermal conductivity. The OCTP plugin has the following features: (1) Once invoked it computes all transport properties on-the-fly in a single simulation, so there is no need to store large trajectory files; (2) it uses the order-n algorithm for the efficient sampling of MSD; (3) it has small cpu and storage requirements; (4) it is easy to setup and use because it follows the native format of LAMMPS input files; and (5) all the data required for the calculation of MSDs are automatically written in restart files, so that long simulations can be performed in consecutive runs. The OCTP source code along with an extensive documentation of its implementation and usage is available as open-source and can be accessed from `https://github.com/omoultosEthTuDelft/OCTP` [218].

This chapter is organized as follows. In Section 3.2, the computation of transport properties from the time correlation functions based on the Einstein approach is described. In Section 3.3, the implementation of the OCTP plugin is briefly described. Two case studies are provided in section Section 3.4, followed by the conclusion in Section 3.5.

3.2. THEORETICAL BACKGROUND

According to the Einstein relations and as explained in Chapter 1, a transport coefficient of a fluid (γ) can be obtained from the coefficient of the linear relation between the mean-squared displacement (MSD) of the time integral of the corresponding dynamical variable ($\dot{A}$) and correlation time (t) [36]. In this section, these relations for the diffusion coefficients, viscosities, and thermal conductivity are discussed. In addition, the order-n algorithm for an efficient sampling of dynamical variables of the system is explained.

3.2.1. DIFFUSIVITY

Three types of diffusion coefficients are discussed here [219]: (1) The self-diffusion coefficient (D_{self}), which is the diffusivity of a tagged particle in a medium due to its Brownian motion; (2) the Fick diffusivity (D_{Fick}), which is the coefficient of the linear relation between the mass flux and the concentration gradient in the system; and (3) the Maxwell-Stefan (MS) diffusivity ($Đ_{\text{MS}}$), which describes mass transport due to the gradient in chemical potential of a species in a mixture. D_{self} involves the motion of individual molecules, while D_{Fick} and $Đ_{\text{MS}}$ are due to the collective motion of all molecules in the system. Hence, for D_{Fick} and $Đ_{\text{MS}}$, the term "collective" or "mutual" diffusion is used. Although the MS diffusivity provides a more general description of transport diffusion in multicomponent mixtures [219], the Fick diffusivity is widely used in industry due to its simplicity. For homogeneous mixtures, the Fick and MS diffusion coefficients are related by the so-called thermodynamic factor (Γ), which is related to the nonideality of the system [220–222]. An extensive analysis and comparison of Fick and MS diffusion coefficients can be found in literature [9, 219, 223].

SELF-DIFFUSIVITY

The self-diffusion coefficient of species i ($D_{i,\text{self}}$) in an isotropic three-dimensional system can be defined as the mean-squared displacement of all molecules of species i [36, 107, 224–227]:

$$\begin{aligned} D_{i,\text{self}} &= \lim_{t\to\infty} \frac{1}{2t}\frac{1}{3N_i}\left\langle \sum_{j=1}^{N_i}\left(\int_0^t \boldsymbol{v}_{j,i}\left(t'\right)\mathrm{d}t'\right)\right\rangle \\ &= \lim_{t\to\infty} \frac{1}{2t}\frac{1}{3N_i}\left\langle \sum_{j=1}^{N_i}\left(\boldsymbol{r}_{j,i}\left(t\right)-\boldsymbol{r}_{j,i}\left(0\right)\right)^2\right\rangle \end{aligned} \tag{3.1}$$

where t is the correlation time, N_i is the number of molecules of species i. $\boldsymbol{v}_{j,i}$ and $\boldsymbol{r}_{j,i}$ are the velocity and position of j-th molecule of species i, respectively. The factor of 3 is for averaging over x, y, and z dimensions [35]. Note that the

OCTP plugin is also able to compute the diffusivities for the three different directions individually. This is required for non-isotropic fluids, e.g. liquid crystals or diffusion in nanoporous materials.

MAXWELL-STEFAN DIFFUSIVITY

The Maxwell-Stefan (MS) diffusion coefficients ($Đ_{\mathrm{MS}}$) of a binary or multicomponent mixture describe the motion of the constituent molecules due to the gradient in chemical potentials of constituent species [9, 107, 222]. MS diffusivities in a three-dimensional system can be obtained from the Onsager coefficients (Λ_{ij}), computed from the crosscorrelation of the displacement of the molecules of species i and j [107, 224, 226–228]:

$$\Lambda_{ij} = \lim_{t\to\infty} \frac{1}{2t}\frac{1}{3N} \left\langle \left(\sum_{k=1}^{N_i} \left(\boldsymbol{r}_{k,i}(t) - \boldsymbol{r}_{k,i}(0) \right) \right) \cdot \left(\sum_{l=1}^{N_j} \left(\boldsymbol{r}_{l,j}(t) - \boldsymbol{r}_{l,j}(0) \right) \right) \right\rangle \tag{3.2}$$

where N_i and N_j are the number of molecules of species i and j, respectively and N is the total number of molecules in the mixture. $\boldsymbol{r}_{l,j}$ is the position of the l-th molecule of species j. The Onsager coefficients (Λ_{ij}) in Eq. (3.2) are defined in a reference frame in which the velocity of the center of mass is zero [224]. Hence, the Onsager coefficients of a binary mixture are correlated by means of the molar masses of the two constituent species (M_1 and M_2) [224]:

$$\Lambda_{12} = -\left(\frac{M_1}{M_2}\right)\Lambda_{11} = -\left(\frac{M_2}{M_1}\right)\Lambda_{22} \tag{3.3}$$

The relations for computing MS diffusion coefficients from Onsager coefficients for binary, ternary, and quaternary mixtures are listed in the articles by Krishna and van Baten [224], and Liu et al. [107, 225, 228, 229]. For a binary mixture with mole fractions of x_1 and x_2, a single MS diffusion coefficient can be defined ($Đ_{12,\mathrm{MS}} = Đ_{21,\mathrm{MS}} = Đ_{\mathrm{MS}}$) [224]:

$$Đ_{\mathrm{MS}} = \frac{x_2}{x_1}\Lambda_{11} + \frac{x_1}{x_2}\Lambda_{22} - 2\Lambda_{12} \tag{3.4}$$

Using the constraint of Eq. (3.3), Eq. (3.4) can be rewritten as separate functions of the Onsager coefficients:

$$\begin{aligned} Đ_{\mathrm{MS}} &= -\left[\frac{(M_2 + x_1(M_1 - M_2))^2}{x_1 x_2 M_1 M_2}\right]\Lambda_{12} \\ &= +\left[\frac{(M_2 + x_1(M_1 - M_2))^2}{x_1 x_2 M_2^2}\right]\Lambda_{11} \\ &= +\left[\frac{(M_2 + x_1(M_1 - M_2))^2}{x_1 x_2 M_1^2}\right]\Lambda_{22} \end{aligned} \tag{3.5}$$

FICK DIFFUSIVITY

The Fick diffusion coefficient (D_{Fick}) describes the diffusion of molecules in a multicomponent mixture as a result of the gradient in the concentration of constituent species [107, 230]. D_{Fick} and $Đ_{\text{MS}}$ are related via the so-called thermodynamic factor (Γ). For a binary mixture, the following algebraic relation holds [9]:

$$D_{\text{Fick}} = \Gamma Đ_{\text{MS}} \tag{3.6}$$

For a multicomponent mixture, the matrix Γ is defined as [9, 107, 221, 222]:

$$\Gamma_{ij} = \delta_{ij} + \left.\frac{\partial \ln \gamma_i}{\partial \ln x_j}\right|_{T,p,\Sigma} \tag{3.7}$$

in which γ_i is the activity coefficient of species i and δ_{ij} is the Kronecker delta. The symbol Σ indicates that the partial differentiation of $\ln\gamma_i$ with respect to mole fraction x_j is carried out at constant mole fraction of all other components except the n-th one, so that $\sum_{i=1}^{n} x_i = 1$ during the differentiation [221]. Analytic expressions for Γ_{ij} for various activity coefficient models are derived by Taylor and Kooijman [221]. There are also different methods for computing the thermodynamic factors such as using equations of state [219, 224], the permuted Widom test particle insertion method [231, 232], and Kirkwood-Buff integrals [107, 123–125, 233, 234]. The last method has the advantage that the required parameters are directly accessible from MD simulations. In this method, the thermodynamic factors for binary systems are obtained from Kirkwood-Buff coefficients (G_{ij}). For isotropic fluids, the finite-size Kirkwood-Buff integral (G_{ij}^{V}) equals [107, 123, 124]:

$$\begin{aligned} G_{ij}^{V} &= \frac{1}{V}\int_V\int_V \left(g_{ij}(r)-1\right)\mathrm{d}\boldsymbol{r_1}\mathrm{d}\boldsymbol{r_2} \\ &= 4\pi\int_0^{2R}\left[g_{ij}(r)-1\right]\left(1-\frac{3r}{4R}+\frac{r^3}{16R^3}\right)r^2\mathrm{d}r \end{aligned} \tag{3.8}$$

where $g_{ij}(r)$ is the radial distribution function, $r = |\boldsymbol{r_1} - \boldsymbol{r_2}|$ and the integration is over a finite spherical subvolume V with radius R. As G_{ij}^{V} scales linearly with $1/R$, the Kirkwood-Buff coefficient in the thermodynamic limit can be obtained by extrapolating the linear regime to $1/R \to 0$ [124, 235]. For more details on obtaining Kirkwood-Buff coefficients from simulation, the reader is referred to the work of Krüger and Vlugt [124], and Dawass et al. [125]. Kirkwood-Buff coefficients can be used to obtained thermodynamic properties of a mixture. For a binary mixture, partial molar volumes $\bar{V}_i$ can be obtained from the following relations [234]:

$$\bar{V}_1 = \frac{1 + c_2\left(G_{22} - G_{12}\right)}{\eta} \tag{3.9}$$

$$\bar{V}_2 = \frac{1 + c_1 (G_{11} - G_{12})}{\eta} \tag{3.10}$$

where c_i indicates the number density of species i, and the auxiliary quantity η is:

$$\eta = c_1 + c_2 + c_1 c_2 \Omega_{12} \tag{3.11}$$

For a binary system the thermodynamic factor follows from [107, 226, 233, 236]:

$$\Gamma = 1 - \frac{c_1 c_2 \Omega_{12}}{\eta} \tag{3.12}$$

where the auxiliary quantity Ω_{ij} is defined as:

$$\Omega_{ij} = G_{ii} + G_{jj} - 2G_{ij} \tag{3.13}$$

Similar expressions can be defined for partial molar volumes and thermodynamic factor matrix of a ternary mixture. The partial molar volumes can be defined as [234, 237]:

$$\begin{aligned}\bar{V}_1 = \frac{1}{\eta}\big[1 &+ c_2 (G_{22} - G_{12}) + c_3 (G_{33} - G_{13}) + \\ &c_2 c_3 \left(G_{12}G_{23} + G_{13}G_{23} + G_{22}G_{33} - G_{13}G_{22} - G_{12}G_{33} - G_{23}^2\right)\big]\end{aligned} \tag{3.14}$$

$$\begin{aligned}\bar{V}_2 = \frac{1}{\eta}\big[1 &+ c_1 (G_{11} - G_{12}) + c_3 (G_{33} - G_{23}) + \\ &c_1 c_3 \left(G_{12}G_{13} + G_{13}G_{23} + G_{11}G_{33} - G_{11}G_{23} - G_{12}G_{33} - G_{13}^2\right)\big]\end{aligned} \tag{3.15}$$

$$\begin{aligned}\bar{V}_3 = \frac{1}{\eta}\big[1 &+ c_2 (G_{22} - G_{23}) + c_1 (G_{11} - G_{13}) + \\ &c_1 c_2 \left(G_{12}G_{13} + G_{12}G_{23} + G_{11}G_{22} - G_{11}G_{23} - G_{13}G_{22} - G_{12}^2\right)\big]\end{aligned} \tag{3.16}$$

where η equals:

$$\begin{aligned}\eta = &c_1 + c_2 + c_3 + c_1 c_2 \Omega_{12} + c_2 c_3 \Omega_{23} + c_1 c_3 \Omega_{13} - \\ &\frac{c_1 c_2 c_3}{4}\left[\Omega_{12}^2 + \Omega_{23}^2 + \Omega_{13}^2 - 2\Omega_{13}\Omega_{23} - 2\Omega_{12}\Omega_{13} - 2\Omega_{12}\Omega_{23}\right]\end{aligned} \tag{3.17}$$

For a ternary mixture, the four components of the thermodynamic factor matrix can be defined [107, 236]:

$$\Gamma_{11} = -\frac{1}{\eta}\Big[-c_2c_3G_{22} - c_2 + 2c_2c_3G_{23} - c_2c_3G_{33} - c_3 + c_1\left(c_2G_{12} - c_2G_{22} - 1 + c_2G_{23} - c_2G_{13}\right)\Big] \tag{3.18}$$

$$\Gamma_{12} = -\frac{c_1}{\eta}\Big[c_2G_{12} + c_3G_{12} - c_2G_{13} - c_3G_{13} - c_2G_{22} + c_2G_{23} - c_3G_{23} + c_3G_{33}\Big] \tag{3.19}$$

$$\Gamma_{21} = +\frac{c_2}{\eta}\Big[c_1G_{11} - c_1G_{12} - c_3G_{12} - c_1G_{13} + c_3G_{13} + c_1G_{23} + c_3G_{23} - c_3G_{33}\Big] \tag{3.20}$$

$$\Gamma_{22} = +\frac{1}{\eta}\Big[c_1c_3G_{11} + c_1 - 2c_1c_3G_{13} + c_1c_3G_{33} + c_3 + c_2\left(c_1G_{11} - c_1G_{12} - c_1G_{13} + 1 + c_1G_{23}\right)\Big] \tag{3.21}$$

It is important to note that one needs to correct for finite-size effects of the radial distribution function. This correction is performed using the procedure outlined by Ganguly and van der Vegt [238, 239]. Accordingly, the corrected RDF ($g_{ij}^{\text{corrected}}$) can be obtained from the computed RDF in a finite-size simulation box (g_{ij}) with a volume of V [238]:

$$g_{ij}^{\text{corrected}}(r) = g_{ij}(r)\,\frac{N_j\left(1 - \frac{(4/3)\pi r^3}{V}\right)}{N_j\left(1 - \frac{(4/3)\pi r^3}{V}\right) - \Delta N_{ij}(r) - \delta_{ij}} \tag{3.22}$$

where δ_{ij} is the Kronecker delta. ΔN_{ij} is the excess number of particles of type j in a sphere surrounding a particle type i with a radius of r [235, 238]:

$$\Delta N_{ij}(r) = \int_0^r \mathrm{d}r' 4\pi r'^2 \frac{N_j}{V}\left(g_{ij}(r') - 1\right) \tag{3.23}$$

It was recently shown that one can compute the RDFs from forces between atoms [240], rather than counting the distances between the atoms [36]. One can use the mean force between molecules to arrive at much smoother RDFs. A possible starting point for this is the thermodynamic identity [240, 241]:

$$g(r) = \beta \int_0^r \mathrm{d}r' g(r') F(r') \tag{3.24}$$

in which $\beta = (k_B T)^{-1}$ and $F(r)$ is the radial component of the average mean force between two molecules separated by distance r:

$$F(r) = \frac{1}{2}\left\langle (\vec{F}_i - \vec{F}_j) \cdot \frac{\vec{r}_{ij}}{|\vec{r}_{ij}|} \right\rangle \tag{3.25}$$

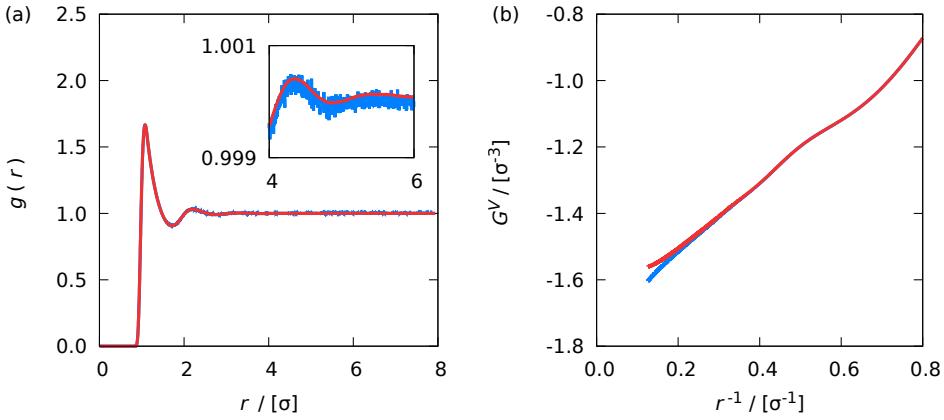

Figure 3.1: Computed (a) RDFs and (b) Kirkwood-Buff integrals (Eq. (3.8)) for a WCA fluid at a reduced temperature of 2.0 and reduced density of 0.5. Blue and red lines correspond to RDFs computed from the conventional counting method ($g_c(r)$) and the new method of using forces on atoms ($g_f(r)$), respectively. In the inset of subfigure (a), the RDFs $g_c(r)$ and $g_f(r)$ are compared for r between 4 and 6 to show the smooth profile of $g_f(r)$.

Here, $\vec{F}_i$ is the net force on molecule i, and $\vec{r}_{ij}$ is the vector that connects molecules i and j. One can write

$$g_f(r) = \int_0^r \mathrm{d}r' g_c(r') F(r') \tag{3.26}$$

where $g_f(r)$ is the resulting redial distribution function, and $g_c(r)$ is the radial distribution from counting distances. Of course, for long simulations $g_f(r)$ and $g_c(r)$ are identical. $g_f(r)$ is much smoother than $g_c(r)$ as it is obtained by integrating $g_c(r)$: integrals are usually much smoother than the integrand as fluctuations in the integrand are integrated out. As a technical note, for computing Kirkwood-Buff integrals (Eq. (3.8)) from RDFs, one can replace the integration by a summation over particle pairs. For any function $F(r)$ that only depends on the intermolecular distance r, one can write:

$$\int_0^R \mathrm{d}r r^2 g(r) F(r) = \frac{V}{2\pi N^2} \sum_{i<j} F(r) H(R-r) \tag{3.27}$$

in which $H(r)$ is the step function. An example of this equation is the computation of the pair energy with R being the cutoff radius and $F(r)$ the intermolecular potential [35, 36].

In Fig. 3.1a, $g_c(r)$ and $g_f(r)$ are compared for a pure WCA fluid, consisting of 2000 particles. WCA is a Lennard-Jones (LJ) potential ($\sigma = 1$ and $\epsilon = 1$) with a cutoff radius of $2^{1/6}\sigma$. Clearly, both RDFs are identical within the numerical accuracy, but the method of summation over pair potentials provide a smoother RDF with smaller noise compared to the conventional method. In Fig. 3.1b, Kirkwood-Buff integrals obtained from these two methods (Eq. (3.8)) are compared. It can be seen that despite a smoother radial distribution function $g_f(r)$, the same Kirkwood-Buff integrals are obtained.

3.2.2. VISCOSITY

SHEAR VISCOSITY

The shear viscosity (η) is the resistance of a fluid to flow [14]. η can be computed from the time integral over the autocorrelation function of the off-diagonal components of the pressure tensor ($P_{\alpha\beta,\alpha\neq\beta}$) [36, 98, 104, 242]:

$$\eta_{\alpha\beta} = \lim_{t\to\infty} \frac{1}{2t} \frac{V}{k_B T} \left\langle \left(\int_0^t P_{\alpha\beta}(t')\,\mathrm{d}t' \right)^2 \right\rangle \tag{3.28}$$

where V is the volume of the system. The components of the pressure tensor are composed of an ideal and a virial term. The first part is due to the total kinetic energy of particles and the second is constructed from intra- and intermolecular interactions [36, 243, 244]. In isotropic systems (rotational invariance), the shear viscosities computed from any of the three off-diagonal components of the pressure tensor (P_{xy},P_{xz}, and P_{yz}) are equal. In isotropic systems, the shear viscosity can also be computed from all components of the traceless pressure tensor ($P^{os}_{\alpha\beta}$) [104, 242]:

$$\eta = \lim_{t\to\infty} \frac{1}{10\cdot 2t} \frac{V}{k_B T} \left\langle \sum_{\alpha\beta} \left(\int_0^t P^{os}_{\alpha\beta}(t')\,\mathrm{d}t' \right)^2 \right\rangle \tag{3.29}$$

where [104]:

$$P^{os}_{\alpha\beta} = \frac{P_{\alpha\beta} + P_{\beta\alpha}}{2} - \delta_{\alpha\beta} \left(\frac{1}{3} \sum_k P_{kk} \right) \tag{3.30}$$

in which $\delta_{\alpha\beta}$ is the Kronecker delta. The last term, i.e. one-third of the invariant trace of the pressure tensor [245], equals the instantaneous kinetic pressure of the system (p). The contribution of the diagonal components of the pressure tensor to the shear viscosity in Eq. (3.29) is 4/3. Therefore, the contribution of all 9 components of the traceless pressure tensor results in the factor 10 in the denominator of Eq. (3.29). Eq. (3.30) uses twice the number of samples as Eq. (3.28). Thus, better statistics can be obtained for the same computational requirement.

BULK VISCOSITY

Bulk viscosity is a mysterious quantity—a transport coefficient, a property of the continuum description of a flow—that points to the molecular world [27]. It is related to the equilibration of the energy of intramolecular degrees of freedom (rotations, vibrations) with translational energy [23, 24]. For CO_2, the bulk viscosity can be a thousand times larger than the shear viscosity [246]. The reason for such large bulk viscosity values lies in the fact that many molecular collisions are needed to equilibrate the vibrational energy. Clearly, the value of the bulk viscosity depends on how fast energy transfer occurs, and hence the value of the bulk viscosity is frequency dependent [27]. In MD simulations, the frequency dependent bulk viscosity can be computed from the van Hove correlation function [99]. At zero frequency, the bulk viscosity can be computed from the fluctuations in the kinetic pressure (δp) [36]:

$$\delta p(t) = p(t) - \langle p \rangle \tag{3.31}$$

where p is the instantaneous pressure and $\langle p \rangle$ is the ensemble-averaged pressure. Accordingly, the Einstein relation for the bulk viscosity is [36, 247]:

$$\begin{aligned}
\eta_{\mathrm{b}} &= \lim_{t\to\infty} \frac{1}{2t}\frac{V}{k_{\mathrm{B}}T}\left\langle \left(\int_0^t \delta p(t')\,\mathrm{d}t'\right)^2 \right\rangle \\
&= \lim_{t\to\infty} \frac{1}{2t}\frac{V}{k_{\mathrm{B}}T}\left\langle \left(\int_0^t \left(p(t') - \langle p \rangle\right)\mathrm{d}t'\right)^2 \right\rangle \\
&= \lim_{t\to\infty} \frac{1}{2t}\frac{V}{k_{\mathrm{B}}T}\left\langle \left(\int_0^t p(t')\,\mathrm{d}t' - \langle p \rangle\, t\right)^2 \right\rangle \\
&= \lim_{t\to\infty} \frac{1}{2t}\frac{V}{k_{\mathrm{B}}T}\left\langle \left(\int_0^t p(t')\,\mathrm{d}t\right)^2 - 2\langle p \rangle\, t\left(\int_0^t p(t')\,\mathrm{d}t\right) + \left(\langle p \rangle\, t\right)^2 \right\rangle
\end{aligned} \tag{3.32}$$

3.2.3. THERMAL CONDUCTIVITY

The thermal conductivity (λ) describes the rate of heat conduction as a result of the temperature gradient in the system [14]. λ can be computed from the components of the energy current/heat flux (J_α) [36]:

$$\lambda_{\mathrm{T}} = \lim_{t\to\infty} \frac{1}{2t}\frac{V}{k_{\mathrm{B}}T^2}\left\langle \left(\int_0^t J_\alpha(t')\,\mathrm{d}t'\right)^2 \right\rangle \tag{3.33}$$

For a system with two-body interactions, the total heat flux is computed from [248, 249]:

$$\boldsymbol{J} = \boldsymbol{J}_{\mathrm{kinetic}} + \boldsymbol{J}_{\mathrm{potential}} = \frac{1}{2}\sum_{k=1}^{N_t} \boldsymbol{v}_k \left[m\boldsymbol{v}_k^2 + \sum_{j=1, j\neq k}^{N_t} \left(\phi_{jk} + \boldsymbol{r}_{jk}\cdot\boldsymbol{f}_{jk}\right)\right] \tag{3.34}$$

where N_t is the total number of atoms in the system. $\boldsymbol{v}_k$ is the velocity vector of atom k. ϕ_{jk}, $\boldsymbol{r}_{jk}$, and $\boldsymbol{f}_{jk}$ are the interaction potential, distance, and force between the two atoms j and k. It is important to note here that Eq. (3.34) is valid for two-body interaction potentials, which has also been implemented in LAMMPS. This is an important limitation of LAMMPS for computing the thermal conductivity. For a detailed discussion on thermal conductivity computation of systems with N-body interactions, the reader is referred to the work of Kinaci et al. [249]. Another limitation of LAMMPS is the incompatibility of heat flux calculation with rigid molecules. Based on observation of different MD simulations performed for these systems, intramolecular interactions are not correctly incorporated for the calculation of the heat flux, which results in wrong computation of the thermal conductivity.

3.2.4. ORDER-n ALGORITHM

The order-n algorithm can be used to efficiently sample correlation functions for the computation of transport properties [35, 250]. In the conventional sampling method [35, 117], time-correlation functions or MSDs are sampled at a fix frequency. For long simulations, a large memory capacity as well as a high computational demand may be needed to capture both fast and slow decaying processes. The order-n algorithm can significantly lower the memory requirements and the computational time by introducing multiple-origin sampling. The main idea is based on sampling time-correlation functions or MSDs at different sampling frequencies. Therefore, several blocks for each sampling frequency with individual buffers are created. For every simulation timestep it is examined if a buffer has to be updated. The oldest element within the buffer is used as the origin to compute the time-correlation function or MSD. The computed quantity is added to an array which will be used to obtain the ensemble-averaged MSD. Afterwards, the oldest element of the buffer is discarded and all other elements are shifted one step to create a space for the newest system property. This procedure is repeated until the end of the simulation and for all blocks. In Fig. 3.2, a schematic representation of the order-n algorithm is presented for 4 buffers of 5 elements with corresponding sampling frequencies of 1, 5, 25 and 125 timesteps. In this figure, the minimum sampling rate is equal to the timestep of the simulation, however, lower sampling frequencies can be used. More details of the original order-n algorithm and the improved algorithm which is used in this implementation can be found in the work of Dubbeldam et al. [117].

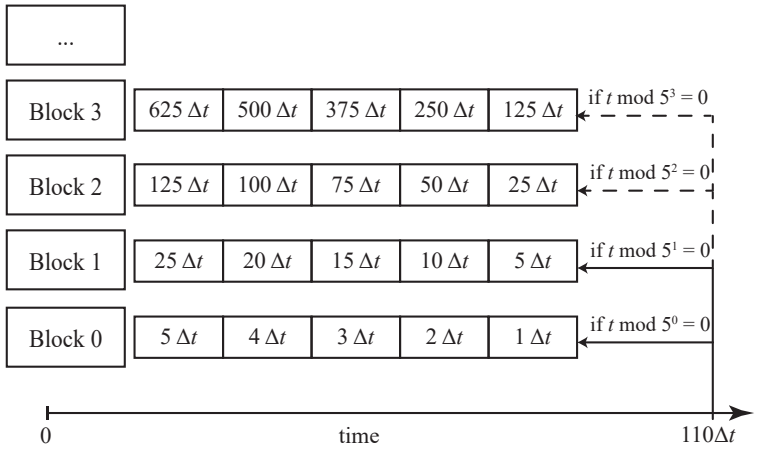

Figure 3.2: Sampling scheme of the order-n algorithm [117]. Several blocks (4 blocks shown here) are used to sample system properties at different timescales. Thus, both fast and slow decaying processes can be sampled [117]. Each block consists of several block (buffer) elements to store the sampled MSD (5 block elements here). The minimum sampling frequency should be a multiple of the timestep. Every timestep, it is examined if the system properties for each block should be sampled. In this example, at timestep 110, system properties are sampled only for the zero-th and first blocks. The next sampling for both the second and third blocks occurs at timestep 125. With the current configuration, MSD for timescales between 1 (fast) and 625 (slow) timesteps can be sampled. For larger timescales, more blocks are required. The computed samples through the whole simulation are then used to compute the ensemble-averaged square displacement, from which the corresponding transport property is calculated.

3.3. CODE STRUCTURE

The OCTP plugin consists of child-classes of the "compute" and "fix" parent-classes. Information on the source code structure of LAMMPS along with instructions for modifications and extensions can be found in the online manual [217]. Consistent with the structure of LAMMPS input commands [217], optional arguments can be specified to adjust the parameters of the plugin. Such arguments include the choice of transport properties to be calculated, details of the order-n algorithm (e.g. the number of blocks), and the names and the format of the output files. A detailed description of all available options is presented in the documentation of the OCTP plugin [218].

When OCTP is invoked, the dynamical variables of the system are sampled using the relevant "compute" commands and stored in memory according to the order-n algorithm. For the computation of self- and MS diffusion coefficients, the positions (i.e., already-integrated velocities) of atoms are sampled. For the bulk and shear viscosities, and thermal conductivity, the components

of the pressure tensor and heat flux are sampled, respectively. These quantities for viscosities and thermal conductivity are then integrated according to the Simpson's rule [251] in the OCTP plugin and the results are stored in memory. It is important to note that the dynamical variables for the viscosity and thermal conductivity should be sampled rather frequently, in the range of 1-10 timesteps. Less frequent sampling would yield unreliable transport coefficients, as the accuracy of numerical integration depends on the time intervals at which a property is sampled.

Although there is a generic command for computing RDFs in LAMMPS, it does not provide RDFs beyond the cutoff radius and finite-size effects are not considered. To address these issues, a new "compute" command is implemented in the OCTP plugin to compute RDFs. The finite-size effects of RDFs are calculated according to the work of van der Vegt and co-workers [238, 239]. RDFs are also computed beyond the cutoff radius and up to $\sqrt{2}/2$ of the box length. In the study by Theodorou and Suter [252], it is shown that the calculation of RDFs can be extended up to $\sqrt{3}/2$ of the box length. For a cubic simulation box, the volume of the truncated sphere with a radius of r in a cubic box with a side length of a can be obtained from the following relations [253]:

$$V_{\text{truncated}}(r) = \begin{cases} \frac{4\pi}{3} r^3 & 0 < r \leq \frac{a}{2} \\ -\frac{\pi}{12}\left(3 - 36r^2 + 32r^3\right) & \frac{a}{2} < r \leq \frac{\sqrt{2}a}{2} \\ -\frac{\pi}{4} + 3\pi r^2 + \sqrt{4r^2 - 2} + f_1(r) + f_2(r) & \frac{\sqrt{2}a}{2} < r \leq \frac{\sqrt{3}a}{2} \end{cases} \tag{3.35}$$

where $f_1(r) = \left(1 - 12r^2\right) \arctan\sqrt{4r^2 - 2}$, and $f_2(r) = \frac{16}{3} r^3 \arctan\frac{2r\left(4r^2 - 3\right)}{\sqrt{4r^2 - 2}\left(4r^2 + 1\right)}$ [253]. Close to the upper limit of $\sqrt{3}/2$ of the box length, the computed RDFs are prone to high statistical uncertainties [252, 253]. The van der Vegt correction [238, 239] combined with the large-distance sampling of RDFs (i.e. beyond the cutoff radius) facilitates the computation of thermodynamic factors using the approach of Krüger and co-workers [123, 124].

For each transport property, the OCTP plugin generates output files containing the correlation time and the corresponding MSD ($\langle (A(t) - A(0))^2 \rangle$). At timescales where the MSD becomes a linear function, the transport property (i.e., the coefficient of proportionality) is obtained by linear regression. The commands used in the LAMMPS input file as well as the output files generated by the OCTP plugin are explained in detail in the online documentation [218]. For more information on the calculation of transport properties using the Einstein relations, the reader is referred to the relevant textbooks [35, 36, 42], the review article by Zwanzig [98], and to other relevant articles on computing diffusivities [107, 250, 254–256], viscosities [242, 247, 257–259], and thermal conductivities [249].

3.4. CASE STUDIES

To illustrate the application of the OCTP plugin, two case studies are investigated here: (1) A binary mixture of water methanol at ambient conditions, and (2) the finite-size effects of transport properties of a Lennard-Jones (LJ) fluid close to the critical point.

3.4.1. BINARY MIXTURE OF WATER AND METHANOL

MD simulations were performed to compute self- and MS diffusion coefficient, shear viscosity, and thermal conductivity of an equimolar mixture of water-methanol ($x_{\text{methanol}} = 0.5$) at 298 K and 1 atm. The SPC/E water model [260] and the TraPPE-UA force field [77] for methanol are used. Non-bonded interactions are truncated at a cutoff radius of 10 Å. Analytic tail corrections are included for the calculation of energy and pressure. The Lorentz-Berthelot mixing rules are used for the interactions of unlike atoms [36]. Long-range electrostatic interactions are considered using the particle-particle particle-mesh (PPPM) method with a relative precision of 10^{-6} [36, 217]. The length of each simulation is 1 ns. Dynamical variables are sampled every 1000, 5, and 5 timesteps, for diffusion coefficients, viscosities, and thermal conductivity, respectively.

In Fig. 3.3, MSDs for the self-diffusion coefficients, Onsager coefficients, shear viscosity, and thermal conductivity are shown in log-log plots. Prior to analyzing the data, two points should be discussed. First, at long correlation times, less samples of system properties can be collected. This insufficient number of samples causes large statistical uncertainties in computed MSDs. In Fig. 3.3b, the effect of large statistical uncertainties can be vividly seen in the irregular and scattered plots of Onsager coefficients at correlation times above 20 ps. Thus, MSDs computed at large correlation times with a small number of samples should be discarded. Second, as shown in Fig. 3.2, the order-n algorithm uses several blocks to sample system properties at different rates. The last element of each block has the same correlation time as the first element of the next block. As frequencies of sampling for two consecutive blocks are different, the computed MSDs for the same correlation time may slightly differ. At large correlation times where the number of samples is small, this difference is large enough to be observed as a jump at a time corresponding to the transition from a block to another. In Fig. 3.3c, such a jump can be seen at 100 ps. As the number of samples increases, this difference between the MSDs of the same correlation time from two consecutive blocks decreases. Considering these two points, linear regression should be performed at the smallest correlation time for which MSD is a linear function of time (i.e., a slope of unity in the log-log plot) [109]. For all

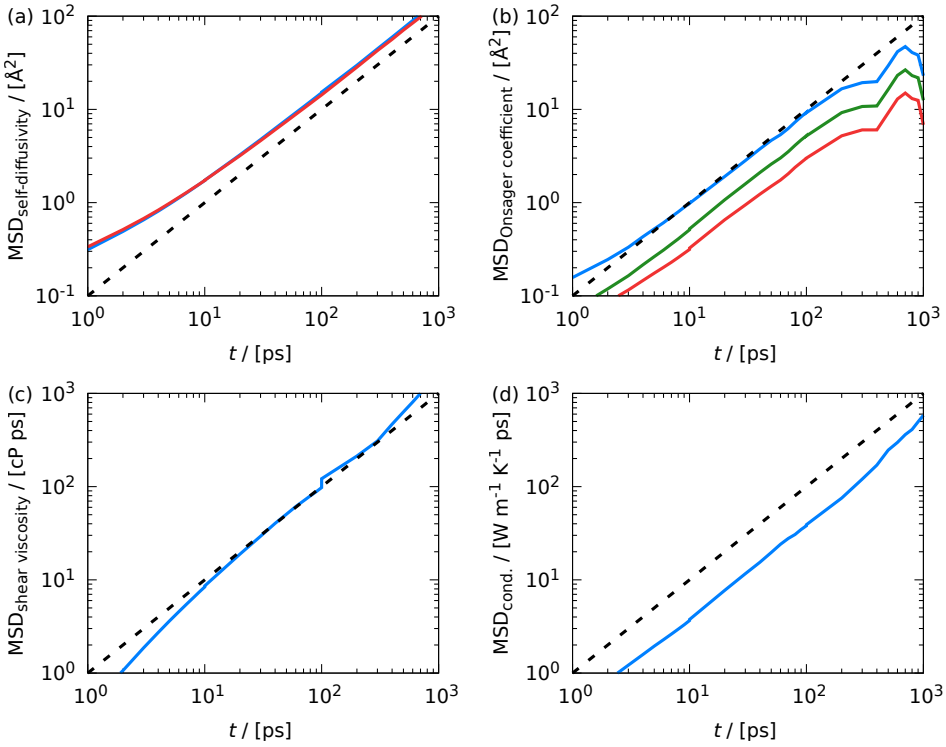

Figure 3.3: Computed MSD as a function of the correlation time for (a) self-diffusivities of water (blue) and methanol (red), (b) Onsager coefficients of water-water (blue), water-methanol (green), and methanol-methanol (red), (c) shear viscosity, and (d) thermal conductivity. The mixture consists of equal mole fractions of water and methanol at 298 K and 1 bar. Transport coefficients can be obtained by performing linear regression at timescales at which the slope of MSD in these log-log plots is equal to 1 (dashed lines) [117].

MSDs, a slope of unity is observed beyond 50 ps. Therefore, transport properties are computed by performing a linear regression at correlation times between 50 ps and 100 ps.

To validate that the new plugin is implemented correctly, the transport properties of the water-methanol mixture computed from the OCTP plugin are compared with the results from the conventional Green-Kubo method. As computed with OCTP, the self-diffusivity of water and methanol is 1.50×10^{-9} m^2s^{-1} and 1.48×10^{-9} m^2s^{-1}, respectively, the MS mutual diffusivity is 2.2×10^{-9} m^2s^{-1}, the shear viscosity is 0.83 cP, and the thermal conductivity is 0.39 $Wm^{-1}K^{-1}$. Based on the Green-Kubo method, the self-diffusivity of water and methanol is 1.61×10^{-9} m^2s^{-1} and 1.48×10^{-9} m^2s^{-1}, respectively, the MS mutual diffusivity

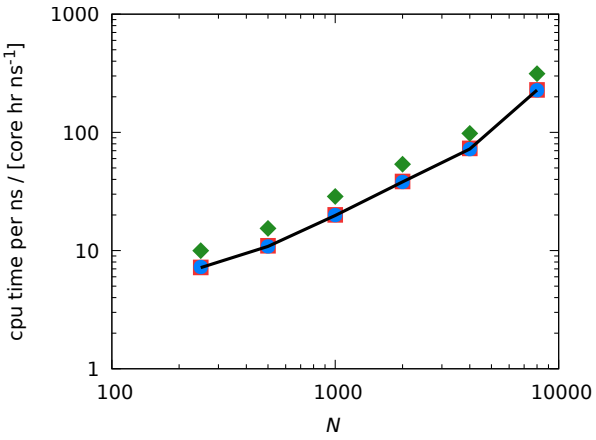

Figure 3.4: Computational requirements and size scalability of the OCTP plugin for simulations to compute diffusion coefficients (blue circles), viscosities (red squares), and thermal conductivity (green diamonds) for different system sizes of an equimolar mixture of water-methanol. The black line indicates computational requirements for simulations without invoking OCTP. The total number of molecules ranges from 250 to 8000 molecules. $T = 298$ K and $P = 1$ atm. All simulations were performed in parallel on a 32-core processor.

is 2.1×10^{-9} m^2s^{-1}, the shear viscosity is 0.85 cP, and the thermal conductivity is 0.38 $Wm^{-1}K^{-1}$. The agreement between the two methods is very good (within approximately 5%).

To demonstrate the computational efficiency and size scalability for the calculation of each transport property with the new OCTP plugin, MD simulations were performed for 6 system sizes (i.e., 250, 500, 1000, 2000, 4000, and 8000 molecules) on a 32-core processing unit (Intel® Xeon® Processor E5-2697A v4 @ 2.60 GHz). The results are presented in Fig. 3.4 for a water-methanol mixture ($x_{\text{methanol}} = 0.5$). Diffusion and viscosity calculations consume less than 2% of the total computational resources, while thermal conductivity calculation consumes approximately 45%. The increased computational requirement for the calculation of thermal conductivity is justified from the intensive calculation of the per-atom properties needed, regardless of the sampling scheme implemented. As mentioned earlier, in the OCTP plugin transport coefficient calculations can be switched on or off individually. Therefore the user can optimize the simulations by switching on only the properties needed. Based on these results, one can conclude that the new plugin is highly efficient for on-the-fly calculations of transport coefficients.

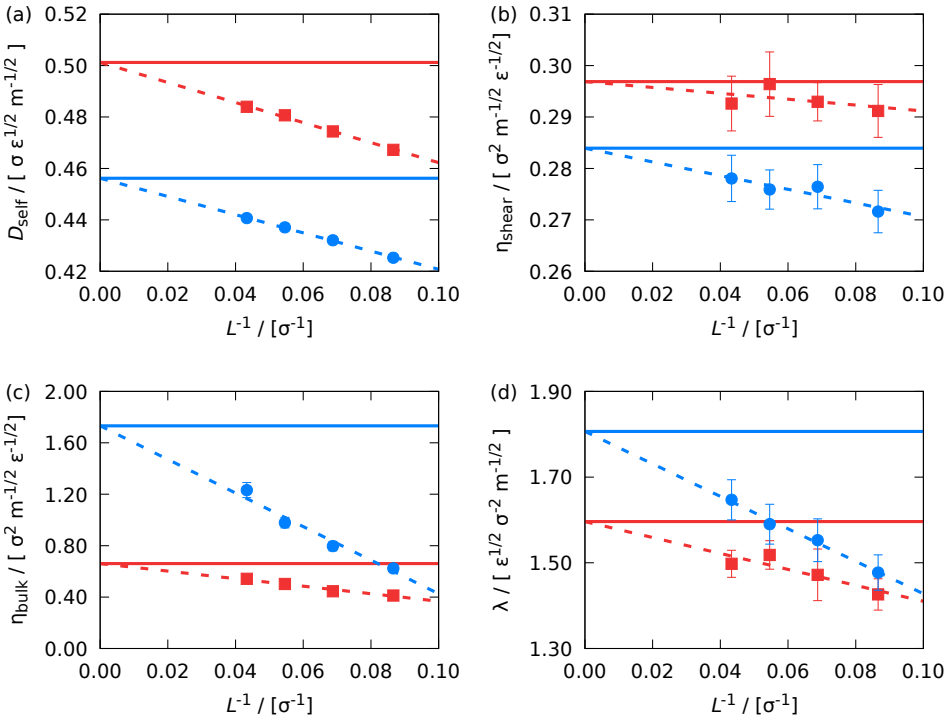

Figure 3.5: (a) Self-diffusivities, (b) shear viscosities, (c) bulk viscosities, and (d) thermal conductivities of a LJ fluid close to the critical point (T_c = 0.937 and ρ_c = 0.320 [261]) as a function of the simulation box length (L). Blue circles and red squares are the computed finite-size transport properties at reduced temperatures of 1.00 and 1.10, respectively. The reduced density is 0.325. The dashed lines indicate extrapolation to the thermodynamic limit, and the solid lines show the values of the transport properties at the thermodynamic limit. Error bars correspond to 95% confidence intervals. Properties are reported in reduced units [36].

3.4.2. FINITE-SIZE EFFECTS OF TRANSPORT PROPERTIES CLOSE TO THE CRITICAL POINT

It is important to note that transport properties computed from MD simulations may depend on the system size and this system size dependency should be corrected to obtain the values in the thermodynamic limit [118, 120, 262, 263]. Especially close to the critical point, transport properties can show considerable finite-size effects [264]. The OCTP plugin is used to investigate the finite-size effects of the self-diffusion coefficient, shear viscosity, bulk viscosity, and ther-

mal conductivity of a LJ fluid close to its critical point. In these simulations, the shifted-force 12-6 LJ potential with a cutoff radius (r_c) of 2.5σ is used to ensure that both potential and force are continuous at the cutoff [36]:

$$U_{\text{LJ,shifted-force}}\left(r_{ij}\right) = \begin{cases} U_{\text{LJ}}\left(r_{ij}\right) - U_{\text{LJ}}\left(r_c\right) - \left(r_{ij} - r_c\right)\left(\frac{\mathrm{d}U_{\text{LJ}}}{\mathrm{d}r_{ij}}\right)_{r_{ij}=r_c} & r \leq r_c \\ 0 & r > r_c \end{cases} \tag{3.36}$$

where r_{ij} is the distance between two particles i and j, σ and ϵ are the LJ size and energy parameters. All properties are reported in reduced units where $\sigma = 1$, $\epsilon = 1$, mass = 1 [36]. For this LJ potential, the critical temperature (T_c) is 0.937 and the critical density (ρ_c) is 0.320 [261])

To study the finite-size effects of this LJ fluid, a density of 0.325 and two temperatures of 1.0 and 1.1 are considered. MD simulations were performed in NVE ensembles, corresponding to the specified temperatures and density. Four system sizes are considered: 500, 1000, 2000, and 4000 LJ particles. At least 5 independent simulations were performed for each system size to compute 95% confidence intervals.

In Fig. 3.5, the finite-size transport properties are shown : (a) self-diffusivity, (b) shear viscosity, (c) bulk viscosity, and (d) thermal conductivity. Except for the shear viscosity, all transport properties show a strong system-size dependency. Bulk viscosity shows the maximum finite-size effect, for which the value in the thermodynamic limit is almost three times the value computed from a system of 500 LJ particles at a temperature of 1.0. By increasing the temperature from 1.0 to 1.1, which corresponds to a state point further from the critical point, the finite-size effects of the bulk viscosity and thermal conductivity decrease considerably. This decrease can be observed for the shear viscosity, although this quantity shows small finite-size effects. However, the finite-size effects of the self-diffusivity do not decrease by increasing the temperature. For both simulations with $T = 1.0$ and $T = 1.1$, the density is the same, and the finite-size effects observed are almost comparable. This shows that other factors may play a role in defining finite-size effects of diffusion coefficients. This subject will be discussed in detail in Chapters 4 and 5.

3.5. CONCLUSIONS

A new plugin implemented in LAMMPS, called OCTP, is presented for on-the-fly computations of the self-diffusivity, Onsager coefficients (to compute the mutual diffusion coefficients), bulk and shear viscosities, and thermal conductivity of pure fluids and mixtures in equilibrium Molecular Dynamics [218]. This is the first implementation in LAMMPS that uses the Einstein relations combined

with the order-n algorithm for the efficient sampling of dynamic variables. The OCTP plugin yields all transport coefficients in a single simulation, has low cpu and storage requirements, and is easy to use since it follows the native LAMMPS input file format. In addition, this plugin features a tool for calculating the radial distribution function of the fluid beyond the cutoff radius, while taking into account system size effects. This precise RDF calculation can be used to calculate the thermodynamic factor, Γ, and thus the Fick mutual diffusivity. The transport properties for an equimolar mixture of water-methanol were computed at 298 K and 1 bar. Furthermore, the finite-size effects of transport properties of a Lennard-Jones fluid close to the critical points was studied. It was found that the computational requirements of this plugin are low and can be used for efficient on-the-fly calculations of transport properties. This plugin will be used in all the other chapters to compute transport coefficients.

4

FINITE-SIZE EFFECTS OF BINARY MUTUAL DIFFUSION COEFFICIENTS

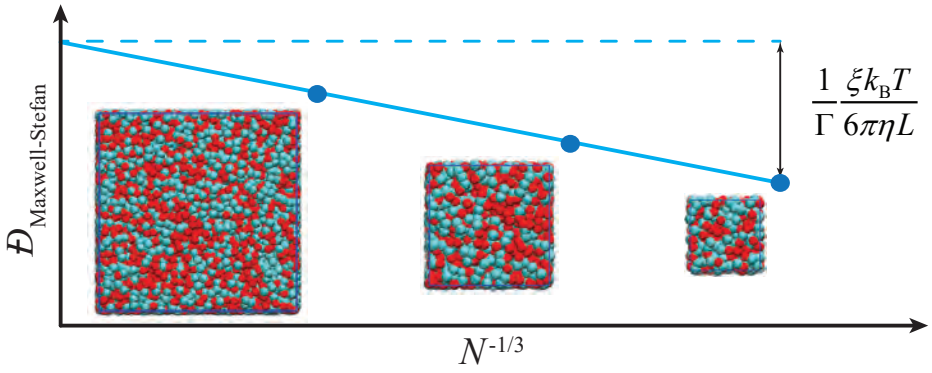

This chapter is based on the papers: S.H. Jamali, L. Wolff, T.M. Becker, A. Bardow, T.J.H. Vlugt, and O.A. Moultos, *Finite-size Effects of Binary Mutual Diffusion Coefficients from Molecular Dynamics*, Journal of Chemical Theory and Computation, **14**, 2667-2677 (2018) [263].

4.1. INTRODUCTION

An important advantages of MD is the possibility of investigating transport phenomena in complex systems such as transport properties of nonideal fluids and permeation of gases/liquids in nanoporous membranes [196, 265–269]. Due to the intrinsic inclusion of the nonideal behavior of mixtures, MD simulations have the potential to foster the deep understanding of diffusion phenomena [270–272] and verify empirical correlations for predicting diffusivities [128, 225, 229, 273, 274]. It is important to note that even with modern computers, the number of molecules considered in a typical MD simulation is orders of magnitude lower than the thermodynamic limit. Thus, it is important to take into account finite-size effects when calculating diffusion coefficients. Simulations of thermodynamic and transport properties for systems close to critical points [264, 275, 276] and phase transitions [277–279] have clearly shown that corrections for the finite size effects should be applied. In the previous chapter, finite-size effects of transport properties of a Lennard-Jones (LJ) fluid close to the critical point were studied. For state points far from the critical point, the finite-size effects of the shear viscosity, bulk viscosity, and thermal conductivity is much smaller compared to state points close to the critical point. However, other factors rather than being close to the critical point affect the system-size dependency of the self-diffusivity.

It has been shown that self-diffusion coefficients computed from MD simulations for a liquid scale linearly with $N^{-1/3}$, where N is the number of molecules in the simulation box [119]. Yeh and Hummer [118] performed a detailed investigation of system-size dependency of self-diffusivities for LJ particles and water molecules. These authors found that the finite-size effects originate from hydrodynamics and derived a correction term (here denoted by "YH correction"). By adding this term to the computed self-diffusivity by MD simulation, the self-diffusivity in the thermodynamic limit can be accurately determined. Nonetheless, no study has focused on the finite-size effects of Maxwell-Stefan (MS) or Fick mutual diffusivities as well as non-infinitely diluted mixtures. In this chapter, the system-size dependency of mutual diffusion coefficients is investigated for binary mixtures. It will be shown that depending on the nonideality of the mixture, there can be significant differences between the simulated (finite size) and real (thermodynamic limit) MS diffusion coefficients.

This chapter is organized in five sections. In Section 4.2, theoretical aspects of self and MS diffusion are briefly discussed. In Section 4.3, details of the MD simulations and the studied mixtures are explained. A detailed analysis of the results of the MD simulations and the proposed correction term to finite-size mutual diffusivities is provided in Section 4.4. Finally, the conclusions of this study are summarized in Section 4.5.

4.2. THEORY

In the previous chapter (Section 3.2), the Einstein relations for computing self, MS, and Fick diffusivity were provided. These equations are used in MD simulations to compute diffusion coefficients that depend on the size of the simulation box. In this section, the available finite-size correction term for the self-diffusivity and the Darken equations are described. These two will help develop a finite-size correction term for mutual diffusion coefficients (i.e., MS and Fick diffusivion coefficients).

4.2.1. FINITE-SIZE EFFECTS OF SELF-DIFFUSIVITIES

Self-diffusion coefficients computed from MD simulations depend strongly on the number of molecules, N, in the simulation box. More specifically, it was shown that self-diffusivity scales linearly with $1/N^{1/3}$, which is equivalent to $1/L$ [119]. Yeh and Hummer [118] studied the size dependence of computed self-diffusion coefficients and derived an analytic correction term to compensate for the observed system-size effects. The correction term was developed based on the hydrodynamic theory for a spherical particle in a Stokes flow with imposed periodic boundary conditions. These authors showed that the difference between the self-diffusivity in an infinite (non-periodic) and a finite (periodic) system is due to the difference in hydrodynamic self-interactions [118, 119, 280]. For the rest of this thesis, the correction term is referred to as the "YH correction". Accordingly, the self-diffusion coefficient of species i in the thermodynamic limit ($D^{\infty}_{i,\text{self}}$) can be estimated from the finite-size self-diffusion coefficient obtained from MD simulations ($D^{\text{MD}}_{i,\text{self}}$) by adding the YH correction (D^{YH}) [118]:

$$D^{\infty}_{i,\text{self}} = D^{\text{MD}}_{i,\text{self}} + D^{\text{YH}}\left(T,\eta,L\right) = D^{\text{MD}}_{i,\text{self}} + \frac{\xi k_{\text{B}} T}{6\pi\eta L} \tag{4.1}$$

where k_{B} is the Boltzmann constant, L is the side length of the simulation box, and η is the shear viscosity of the system at temperature T. ξ is a dimensionless constant equal to 2.837297 for cubic simulation boxes with periodic boundary conditions [118]. Similar to YH correction, equations have been derived for simulations in non-cubic boxes [281–283] and for confined fluids [284]. It is important to note that the YH correction does not explicitly depend on the intermolecular interactions, or the size and shape of molecules in a fluid as shown by several studies for systems of non-spherical molecules [214, 262, 285]. This means that all species of a multicomponent mixture experience identical finite-size effects, which can be corrected by the YH correction.

4.2.2. MAXWELL-STEFAN DIFFUSIVITIES AND THE DARKEN EQUATION

The Onsager coefficient of species i (Λ_{ii}, Eq. (3.2)) can be split into an autocorrelation term, which is the self-diffusivity of species i ($D_{i,\text{self}}$), and a crosscorrelation term (C_{ii}) [228, 270]:

$$\begin{aligned}\Lambda_{ii} = &\lim_{t\to\infty}\frac{1}{6Nt}\left\langle\left(\sum_{k=1}^{N_i}\left(\boldsymbol{r}_{k,i}(t)-\boldsymbol{r}_{k,i}(0)\right)^2\right)\right\rangle + \\ &\lim_{t\to\infty}\frac{1}{6Nt}\left\langle\left(\sum_{k=1}^{N_i}\left(\boldsymbol{r}_{k,i}(t)-\boldsymbol{r}_{k,i}(0)\right)\right)\cdot\left(\sum_{l=1,l\neq k}^{N_i}\left(\boldsymbol{r}_{l,i}(t)-\boldsymbol{r}_{l,i}(0)\right)\right)\right\rangle \\ &= x_i D_{i,\text{self}} + C_{ii}\end{aligned} \tag{4.2}$$

The Onsager coefficient of two different species (Λ_{ij}, where $i \neq j$) is a displacement crosscorrelation of the constituent two species (C_{ij}|):

$$\Lambda_{ij,i\neq j} = C_{ij} \tag{4.3}$$

Eqs. (3.4) and (3.5) are valid for both ideal and nonideal diffusing binary mixtures. For ideal diffusing binary mixtures, the crosscorrelation between the particles of the two species is rather small compared to the self-diffusivities. This means that in Eqs. (3.4), (4.2) and (4.3): $(x_2/x_1)C_{11} + (x_1/x_2)C_{22} - 2C_{12} \ll x_1 D_{1,\text{self}} + x_2 D_{2,\text{self}}$. Thus, the MS diffusivity (Eq. (3.4)) can be simplified to the Darken equation ($Đ_{\text{Darken}}$) [228, 229, 270]:

$$Đ_{\text{Darken}} = x_2 D_{1,\text{self}} + x_1 D_{2,\text{self}} \tag{4.4}$$

This equation indicates that the MS diffusivity of an ideal diffusing binary mixture with small crosscorrelations can be obtained from the self-diffusion coefficients of its constituent molecules in that mixture. A similar equation, called the predictive Darken-LBV, can defined for multicomponent mixtures [107, 229]. The definition of the Darken equation will help define a framework to develop a finite-size correction for MS diffusivities based on the YH correction, which is only applicable to self-diffusivities.

4.3. SIMULATION DETAILS

All simulations were performed in cubic simulation boxes. Periodic boundary conditions were imposed in all directions. All MD simulations were conducted with LAMMPS [126] (version 16 Feb. 2016). The initial configurations and LAMMPS input files were constructed with PACKMOL [286] and VMD [200]. All raw data of the simulations mentioned below are listed in the Supporting Information of the work of Jamali et al. [263].

Table 4.1: Specifications of the studied LJ systems. LJ particle type 1 has $\sigma_1 = \sigma = 1.0$, $\epsilon_1 = \epsilon = 1.0$, and mass = $m_1 = 1.0$ in reduced units [36]. k_{ij} is an adjustable parameter to the Lorentz-Berthelot mixing rules (Eq. (4.5)), controlling the nonideality of the mixtures.

Parameters	Values
Total number of particles	500, 1000, 2000, 4000
Independent simulations	10, 10, 5, 5
x_1	0.1, 0.3, 0.5, 0.7, 0.9
ϵ_2/ϵ_1	1.0, 0.8, 0.6, 0.5
σ_2/σ_1	1.0, 1.2, 1.4, 1.6
m_2/m_1	$(\sigma_2/\sigma_1)^3$
k_{ij}	0.05, 0.0, -0.3, -0.6

To study the finite-size effects of MS diffusion coefficients in binary mixtures two sets of MD simulations were carried out. The first set consists of binary LJ systems. All parameters and properties of these simulations are reported in dimensionless units with the ϵ and σ parameters of the first LJ species as the base units: $\sigma_1 = \sigma = 1$, $\epsilon_1 = \epsilon = 1$, and mass = $m_1 = m = 1$. The characteristics of the second species (ϵ_2, σ_2, and $m_2 = \sigma_2^3$), mole fractions (x), and adjustable parameters (k_{ij}; see below) of all studied LJ systems are listed in Table 4.1. The applied temperature T and pressure p in the simulations are 0.65 and 0.05, respectively. The number density of the studied systems is between 0.14 and 0.89. A time step of 0.001 is used for the integration of equations of motion. Displacement and stress correlation functions are computed for a total length of 200 million time steps. In total, 320 distinct LJ systems with four system sizes (500, 1000, 2000, and 4000 particles) are simulated. To create a sound dataset, systems in which phase separation occurs or a considerable deviation of the pressure or temperature from the specified conditions is observed are excluded from the data analysis. These systems correspond to a small fraction of the total dataset. The second set of MD simulations includes 9 binary mixtures consisting of molecular systems. An overview of these mixtures—consisting of methanol as the first component, and water, ethanol, acetone, methylamine, or carbon tetrachloride as the second component—is listed in Table 4.2. For each mixture, four system sizes (250, 500, 1000, and 2000 molecules) are considered. The temperature and pressure are specified to be 298 K and 1.0 atm. The total length of each simulation is 200 ns with an integration time step of 1 fs.

For LJ systems, LJ interactions are truncated and shifted to zero at a cutoff radius of 4σ [36]. For the interactions between dissimilar LJ particles (i and j), the Lorentz-Berthelot mixing rules with a modification factor (k_{ij}), controlling the nonideality of mixtures, are applied to the LJ parameters [36]:

Table 4.2: Specifications of all studied binary molecular systems. The first component for all mixtures is methanol. The mole fraction of the second component is specified in parentheses.

Parameters	Values
Total number of molecules	250, 500, 1000, 2000
Independent simulations	10, 10, 10, 10
Second component (mole fraction)	Water (0.1, 0.3, 0.5, 0.7, 0.9)
	Ethanol (0.5)
	Acetone (0.5)
	Methylamine (0.5)
	Carbon tetrachloride (0.1)

$$\epsilon_{ij} = \left(1 - k_{ij}\right)\sqrt{\epsilon_{ii}\cdot\epsilon_{jj}} \tag{4.5}$$

$$\sigma_{ij} = \frac{\sigma_{ii} + \sigma_{jj}}{2} \tag{4.6}$$

For the molecular systems, the SPC/E model [260] and the model proposed by Tummala et al. [287] are used for water and carbon tetrachloride molecules, respectively. The force field parameters for methanol [77], ethanol [77], acetone [78], methylamine [75, 79] are obtained from the Transferable Potential for Phase Equilibria (TraPPE) force field [75]. The LJ interactions are truncated at 12.0 Å and analytic tail corrections for energy and pressure are included [36]. The Lorentz-Berthelot mixing rules for dissimilar interaction sites are applied [36]. Long-range electrostatic interactions are taken into account by means of the particle-particle particle-mesh (PPPM) method with a relative precision of 10^{-6} [36].

To obtain the average properties and their 95% confidence intervals of each data point, at least five independent simulations were carried out. For better sampling of displacement and stress correlation functions, the order-n algorithm [35, 117] was used by employing the OCTP plugin for LAMMPS [210]. As explained in the Section 3.2, the thermodynamic factors were calculated from the RDFs of the constituent species using finite-size Kirkwood-Buff integrals [123]. The RDFs were computed from MD simulations of large systems in the canonical ensemble. These systems contain 25000 LJ particles (first set of simulations) and 13500 molecules (second set of simulations). The total length of simulations for computing the Kirkwood-Buff integrals is 10 million time steps for the LJ systems, and 10 ns for the molecular mixtures.

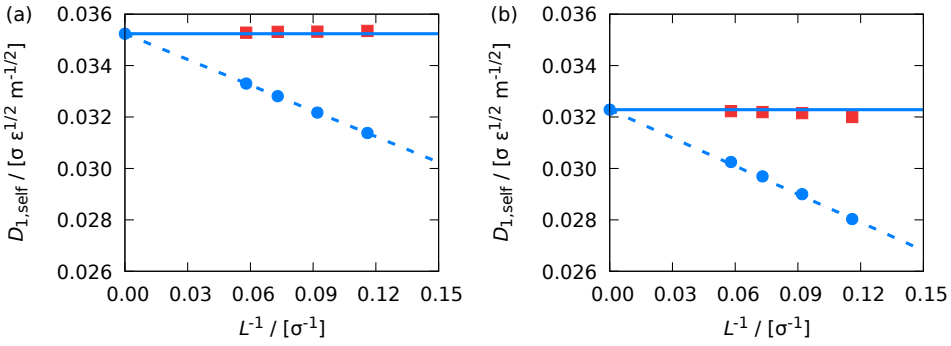

Figure 4.1: Self-diffusion coefficients of (a) species 1 and (b) species 2 of a binary LJ mixture (x_1 = 0.9) as a function of the simulation box length (L). Blue circles are the computed self-diffusion coefficients in finite systems and red squares are the corrected values using the YH correction term (Eq. (4.1)). The dashed lines indicate extrapolation to the thermodynamic limit and the solid lines show the extrapolated self-diffusivities. The second component has $\epsilon_2 = 0.5\epsilon_1$ and $\sigma_2 = 1.2\sigma_1$, and the adjustable parameter (k_{ij}) to the Lorentz-Berthelot mixing rules is 0. The error bars are smaller than the symbols.

4.4. RESULTS AND DISCUSSIONS

Previous studies on the system-size dependencies of self-diffusion coefficients are limited to pure fluids and infinitely diluted mixtures. Fig. 4.1 shows an example of the self-diffusivities of the two components of a binary LJ system as a function of the length of the simulation box (L). As in pure fluids, the computed self-diffusion coefficients vary linearly with the inverse of the simulation box length. The linear regression at $1/L = 0$ yields the self-diffusivity for an infinite system size ($D^{\infty}_{i,\text{self}}$), which is shown in the same figure as a horizontal line. The finite-size self-diffusivities corrected with D^{YH} (Eq. (4.1)) are plotted as red squares. As expected, the corrected self-diffusivities collapse on the horizontal line, indicating the validity of YH correction.

In Fig. 4.2, the differences between the infinite and finite-size self-diffusivities ($D^{\infty}_{i,\text{self}} - D^{\text{MD}}_{i,\text{self}}$) are plotted as a function of the YH correction (D^{YH}), for all entries in the dataset examined. For the majority of the cases, the YH correction term is able to predict the finite-size discrepancies very accurately. However, while the correction is almost perfect for molecular mixtures, a systematic overprediction of self-diffusivities can be observed for LJ systems. This overprediction becomes more pronounced as the difference between the size and the interaction energies of the species in the system increases. Out of the 250 LJ systems considered, 13 correspond to systems containing particles with large

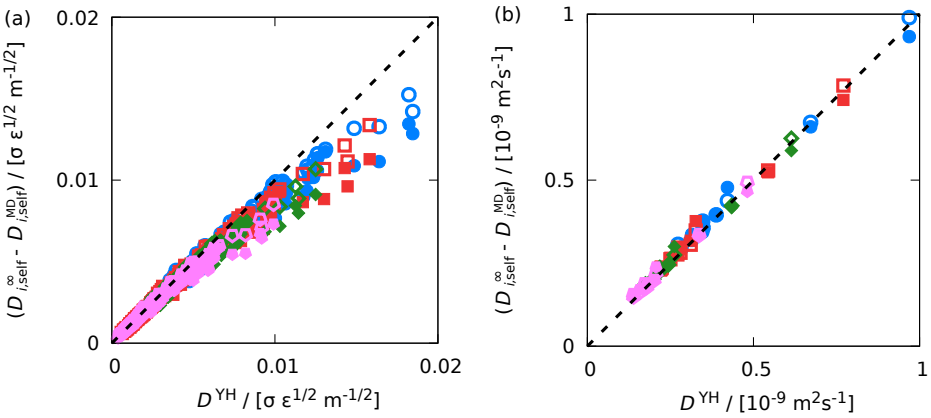

Figure 4.2: Finite-size corrections required for self-diffusion coefficients as a function of the YH correction (D^{YH}, Eq. (4.1)) for (a) LJ and (b) molecular mixtures computed with: 500 LJ particles/250 molecules (blue circles), 1000 LJ particles/500 molecules (red squares), 2000 LJ particles/1000 molecules (green diamonds), and 4000 LJ particles/2000 molecules (purple pentagons). Closed and open symbols represent the corrections to the self-diffusivity of species 1 and species 2, respectively. The dashed lines indicate perfect agreement.

dissimilarities in size (σ_2/σ_1 equal to 1.6 and 1.4) and interaction energy (ϵ_2/ϵ_1 equal to 0.5 and 0.6). The limitations of the YH correction will extensively be discussed in Chapter 5.

For a correct prediction of the finite-size effects of self-diffusion coefficients from the YH correction, it is important to investigate the system-size dependency of the shear viscosity. Previous studies by Yeh and Hummer [118] and Moultos et al. [262] revealed that the shear viscosity does not depend on the system size. The current extensive dataset of LJ and molecular systems makes it possible to thoroughly examine their conclusion. Fig. 4.3 shows a comparison of the shear viscosities for two different system sizes of all LJ (500 and 4000 LJ particles) and molecular systems (250 and 2000 molecules). In all cases, the shear viscosity computed from the smallest system size equals the shear viscosity obtained from the largest system size. This confirms the conclusion of the previous studies [118, 262] that shear viscosities computed in equilibrium MD simulations do not show any system-size dependency, except for conditions close to the critical point (see the second case study in Section 3.4).

Fig. 4.4 illustrates the finite-size effects of the Darken equation ($Đ_{\mathrm{Darken}}$, Eq. (4.4)) and MS diffusivities ($Đ_{\mathrm{MS}}$, Eq. (3.4)) for the same binary LJ mixture of Fig. 4.1. In Fig. 4.4a, using the YH correction, D^{YH}, for the finite-size effects

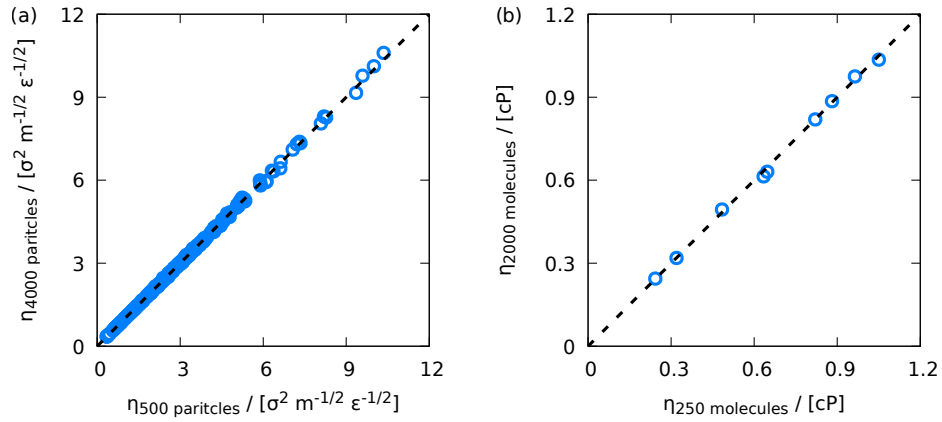

Figure 4.3: Comparison between the shear viscosities of the smallest and largest system sizes for the studied (a) LJ and (b) molecular systems, computed from equilibrium MD simulations. The dashed line indicates the equality of shear viscosities of the two system sizes.

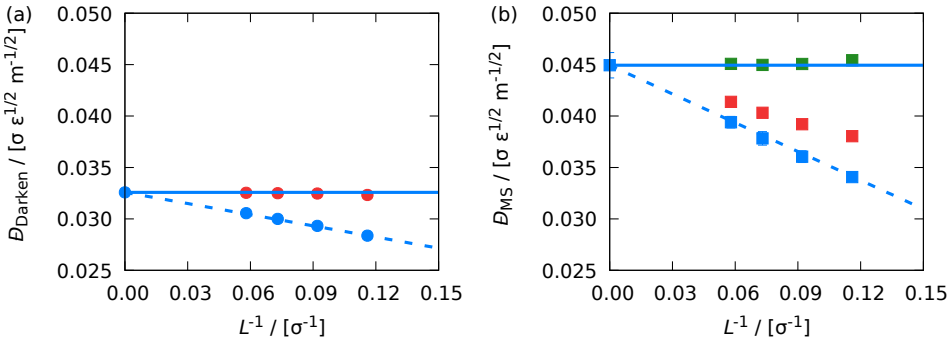

Figure 4.4: (a) Binary Darken and (b) MS diffusivities for a binary LJ mixture ($x_1 = 0.9$) as a function of the simulation box length (L). Blue circles and squares are the computed Darken (Eq. (4.4)) and MS (Eq. (3.4)) diffusivities, respectively. Darken diffusivities corrected by the YH relation (Eq. (4.1)) is shown with red circles. Red and green squares are the corrected MS diffusivities according to the YH (Eq. (4.1)) and the MSYH (Eq. (4.9))) respectively. The dashed lines show extrapolation to the thermodynamic limit and the solid lines show the extrapolated values. The second component has $\epsilon_2 = 0.5 \times \epsilon_1$ and $\sigma_2 = 1.2 \times \sigma_1$, and the adjustment parameter (k_{ij}) to the Lorentz-Berthelot mixing rules is 0. The error bars are smaller than the symbols.

of the self-diffusivities of species 1 and 2 (see Eq. (4.4)) accurately accounts for the finite-size effects of the Darken equation, $Đ_{\text{Darken}}$. In Fig. 4.4b, the same YH correction is used for the finite-size effects of MS diffusion coefficients, $Đ_{\text{MS}}$ (red squares). The red squares are systematically lower than the extrapolated MS diffusivity to the thermodynamic limit. This indicates that D^{YH} cannot always correct the finite effects of $Đ_{\text{MS}}$, especially for nonideal mixtures where the Darken equation and MS diffusivity are not equal. To further investigate this, the finite-size effect of the MS diffusivity can be obtained from Eqs. (3.5) and (4.2) as follows:

$$
\begin{aligned}
Đ^{\infty}_{\text{MS}} - Đ^{\text{MD}}_{\text{MS}} &= \left[\frac{\left(M_2 + x_1\left(M_1 - M_2\right)\right)^2}{x_1 x_2}\right]\frac{1}{M_2^2}\left(\Lambda^{\infty}_{11} - \Lambda^{\text{MD}}_{11}\right) \\
&= \frac{\alpha'}{M_2^2}\left[\left(x_1 D^{\infty}_{1,\text{self}} + C^{\infty}_{11}\right) - \left(x_1 D^{\text{MD}}_{1,\text{self}} + C^{\text{MD}}_{11}\right)\right] \\
&= \frac{\alpha'}{M_2^2}\left[x_1\left(D^{\infty}_{1,\text{self}} - D^{\text{MD}}_{1,\text{self}}\right) + \left(C^{\infty}_{11} - C^{\text{MD}}_{11}\right)\right] \\
&= \frac{\alpha'}{M_2^2}\left[x_1 D^{\text{YH}} + \left(C^{\infty}_{11} - C^{\text{MD}}_{11}\right)\right] \\
&= \frac{\alpha''}{M_1^2}\left[x_2 D^{\text{YH}} + \left(C^{\infty}_{22} - C^{\text{MD}}_{22}\right)\right]
\end{aligned}
\tag{4.7}
$$

where α' and α'' are constants (unknown at this point). $Đ^{\infty}_{\text{MS}}$ and $Đ^{\text{MD}}_{\text{MS}}$ are the MS diffusivities in the thermodynamic limit and finite-size systems, respectively. C^{∞}_{ii} and C^{MD}_{ii} are the infinite and finite-size displacement crosscorrelation functions of species i.

As shown in Fig. 4.4, in nonideal mixtures, the total displacement crosscorrelation function of all particles has a considerable contribution to the finite-size effect. At this point, one can hypothesizes that a modified YH correction term can be applied directly to the MS diffusion coefficients. Thus, the crosscorrelation terms of Eq. (4.7), $C^{\infty}_{ii} - C^{\text{MD}}_{ii}$, can be a function or simply a modification factor of the YH correction. Since the crosscorrelation terms are directly related to the nonideality of a mixture, it is expected that this modification factor should be a function of the thermodynamic factor (Γ) [272]:

$$
\begin{aligned}
Đ^{\infty}_{\text{MS}} - Đ^{\text{MD}}_{\text{MS}} &= \frac{\alpha'}{M_1^2}\left[x_2 D^{\text{YH}} + \left(C^{\infty}_{22} - C^{\text{MD}}_{22}\right)\right] \\
&= \frac{\alpha'}{M_1^2}\left[x_2 D^{\text{YH}} + \alpha'' D^{\text{YH}}\right] \\
&= \alpha(\Gamma) \times D^{\text{YH}}
\end{aligned}
\tag{4.8}
$$

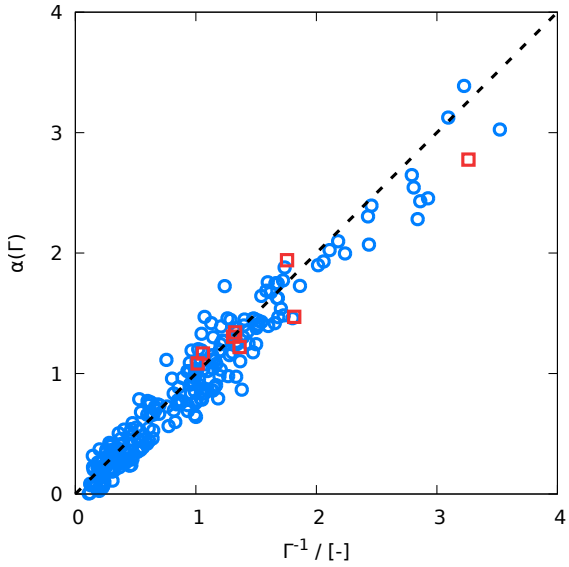

Figure 4.5: Modification factor to the YH correction (α) as a function of the thermodynamic factor (Γ) for nonideal mixtures according to Eq. (4.8). Blue circles and red squares show the modification factors for the LJ and molecular systems, respectively. The thermodynamic factor for ideal mixtures equals 1. The dashed line indicates perfect agreement.

where $\alpha(\Gamma)$ is the modification factor to the YH correction, accounting for the finite-size effects of the MS diffusion coefficient. In the example shown in Fig. 4.4, the thermodynamic factor of the mixture, Γ, is 0.35 and the modification factor required to scale the YH correction from the red squares to the green squares is roughly 3, which is approximately equal to $1/\Gamma$. To examine if $1/\Gamma$ is a suitable modification of the YH correction for correcting the finite-size effect of MS diffusion coefficients a phenomenological approach is followed: In Fig. 4.5, $1/\Gamma$ is compared to the required modification factor to D^{YH} for all LJ (blue circles) and molecular (green diamonds) systems. The agreement observed suggests that $1/\Gamma$ is a suitable modification factor to the YH correction for MS diffusion coefficients. Hence, Eq. (4.8) can be rewritten as:

$$Đ^{\infty}_{\mathrm{MS}} - Đ^{\mathrm{MD}}_{\mathrm{MS}} = \alpha D^{\mathrm{YH}} \approx \left(\frac{1}{\Gamma}\right) D^{\mathrm{YH}} \tag{4.9}$$

In the rest of the thesis, the last term (D^{YH}/Γ) is called the "Maxwell-Stefan Yeh and Hummer" (MSYH) correction ($Đ^{\mathrm{MSYH}} = D^{\mathrm{YH}}/\Gamma$). The results shown in Fig. 4.5 suggest that by describing the correction for MS as a function of only Γ seems to be sufficient, however the possibility that other (still unknown) factors contribute to the correction cannot be ruled out.

By combining Eqs. (3.6) and (4.9), the finite-size correction to the Fick diffusion coefficient for a binary mixture can be calculated from:

$$D^{\infty}_{\mathrm{Fick}} - D^{\mathrm{MD}}_{\mathrm{Fick}} = \Gamma Đ^{\infty}_{\mathrm{MS}} - \Gamma Đ^{\mathrm{MD}}_{\mathrm{MS}} = \Gamma\left(Đ^{\infty}_{\mathrm{MS}} - Đ^{\mathrm{MD}}_{\mathrm{MS}}\right) = \Gamma\left(\frac{1}{\Gamma}D^{\mathrm{YH}}\right) = D^{\mathrm{YH}} \tag{4.10}$$

where $D^{\infty}_{\mathrm{Fick}}$ and $D^{\mathrm{MD}}_{\mathrm{Fick}}$ are Fick diffusivities in infinite and finite-size systems, respectively. Interestingly, the same YH correction that is applied to self-diffusivities can mitigate the finite-size effects of Fick diffusion coefficients, regardless of the ideality or nonideality of the mixture.

In Fig. 4.6, the correction for the finite-size effects of MS diffusion coefficients ($Đ^{\infty}_{\mathrm{MS}} - Đ^{\mathrm{MD}}_{\mathrm{MS}}$) are compared to the predicted MSYH correction ($Đ^{\mathrm{MSYH}}$) for the studied LJ (Fig. 4.6a) and molecular systems (Fig. 4.6b). As expected from Fig. 4.5, a rather good agreement can be seen for both sets. These results suggest that $Đ^{\mathrm{MSYH}}$ works equally good for simple systems such as LJ systems and for non-spherical molecular systems with long-range electrostatic interactions. As proposed by Moultos et al. [262], a minimum number of 250 molecules is used for all molecular systems. For a smaller number of molecules, the shape and anisotropic structure of constituent molecules may play a role and affect the accuracy of the YH correction. Since no outlier is observed for the molecular systems in Fig. 4.6b, the same criterion for the minimum number of molecules seems to be applicable to the MSYH correction.

While the proposed MSYH correction (see Fig. 4.6) seems to perform fairly accurate, two important points should be noted:

1. The MSYH correction overpredicts the finite-size effects of MS diffusivities for LJ systems. This is consistent with the earlier observations for self-diffusivities (Fig. 4.2a). The MSYH correction is based on the YH correction (Eq. (4.9)), so any overprediction of D^{YH} affects $Đ^{\mathrm{MSYH}}$. To show the cause of this overprediction, the same comparison as in Fig. 4.6, between the required corrections, is considered. However, instead of the analytic YH correction, the differences between the computed infinite and finite-size Darken diffusivities are used (see Fig. 4.7). For molecular mixtures, no difference is noticed. This is expected since the YH correction performs well according to Fig. 4.2b. Note that the overprediction observed in Fig. 4.2a and Fig. 4.6a are not present in Fig. 4.7a and the data points are symmetrically distributed on both sides of the diagonal line. This indicates that

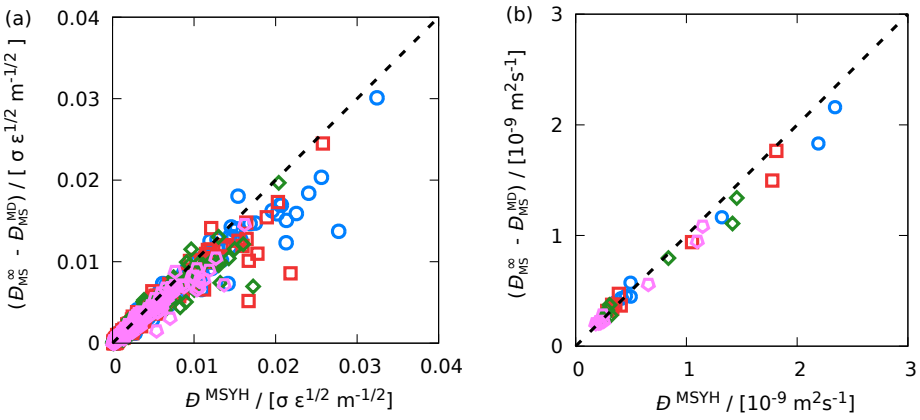

Figure 4.6: Correction needed for the MS diffusion coefficients versus the the MSYH correction term ($Đ^{MSYH}$, Eq. (4.9)) for (a) LJ and (b) molecular systems computed with: 500 LJ particles/250 molecules (blue circles), 1000 LJ particles/500 molecules (red squares), 2000 LJ particles/1000 molecules (green diamonds), and 4000 LJ particles/2000 molecules (purple pentagons). The dashed lines show perfect agreement.

the less accurate predictions by the YH correction resulted in the overpredictions shown in Fig. 4.6, and that the proposed modification of Eq. (4.9) does not introduce any systematic deviations.

2. The data points shown in Figs. 4.5 to 4.7 for MS diffusivities are more scattered compared to those of self-diffusion coefficients illustrated in Fig. 4.2. The cause can be the large statistical uncertainties of thermodynamic factors and finite-size MS diffusivities as well as the extrapolation of MS diffusion coefficients ($Đ_{MS}$) to the thermodynamic limit. These influences are expected to contribute to the scattered data in Figs. 4.5 and 4.6.

As the MSYH correction is related to the YH correction via the thermodynamic factor, three possible scenarios for studying the significance of the MSYH correction can be conceived: (1) In case of $\Gamma = 1$, the behavior of the mixture is ideal. The YH correction can directly be applied to self, MS, and Fick diffusivities. (2) For $0 < \Gamma < 1$, the constituent species of the mixture tend to self-associate and the cross-interactions are less pronounced. Since Γ is smaller than 1, the modification factor makes the MSYH correction larger than the YH correction. (3) For associating mixtures with thermodynamic factors larger than 1, the correction

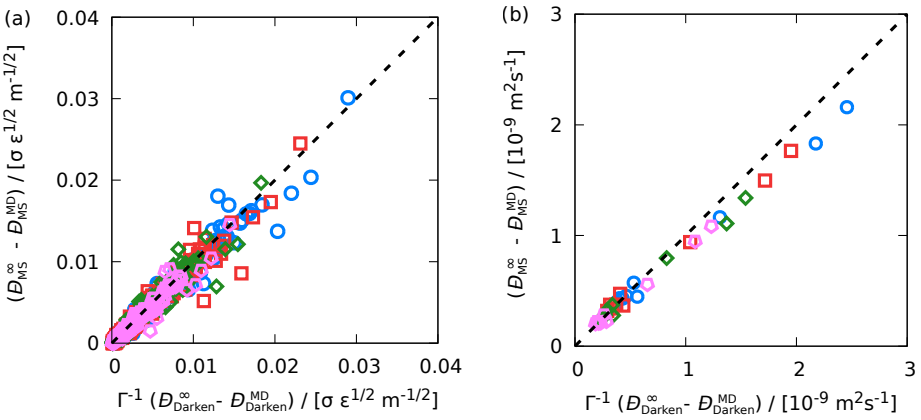

Figure 4.7: Correction needed for the MS diffusion coefficients versus the extrapolated Darken equation with the modification factor included ($\Gamma^{-1}(Đ^{\infty}_{\text{Darken}} - Đ^{\text{MD}}_{\text{Darken}})$) for (a) LJ and (b) molecular systems computed with: 500 LJ particles/250 molecules (blue circles), 1000 LJ particles/500 molecules (red squares), 2000 LJ particles/1000 molecules (green diamonds), and 4000 LJ particles/2000 molecules (purple pentagons). The dashed lines show perfect agreement.

decreases to smaller values than the YH correction. For mixtures with very large thermodynamic factors, the finite-size correction becomes negligible and overlaps with the statistical uncertainty of the computed MS diffusion coefficient.

To show the importance of the MSYH correction for systems with $0 < \Gamma < 1$, a mixture of methanol-carbon tetrachloride ($x_{\text{methanol}} = 0.90$) is considered. This mixture has a small thermodynamic factor approximately equal to 0.18. Accordingly, the modification factor to the YH correction for MS diffusivities would be approximately 6 ($\approx 1/0.18$). To investigate the magnitude of the finite-size effect, in Fig. 4.8 the Darken and MS diffusion coefficients of this mixture are shown for four system sizes. As expected, both the YH and MSYH corrections can accurately predict the finite-size diffusivities. Whereas the finite-size effect for the self-diffusivites is at most 20% of the uncorrected value, the finite-size effect for MS diffusivites can be as large as 60% of the computed values in the current MD simulations. The contribution of the finite-size effect becomes even more pronounced for $\Gamma \to 0$, i.e., close to demixing. Therefore, considering the MSYH correction is particularly important for such systems.

The finite-size effects of MS diffusivities are not limited to binary systems. A similar system-size dependency can be observed in ternary and multicomponent mixtures. In Fig. 4.9, finite-size MS diffusivities are plotted for the three MS diffusivities of a ternary mixture as a function of the size of the simulation box.

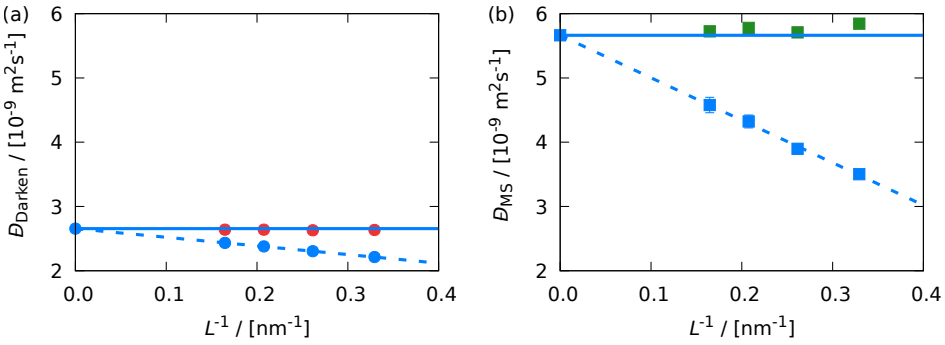

Figure 4.8: (a) Binary Darken and (b) MS diffusivities for a mixture of methanol-carbon tetrachloride ($x_{methanol}$ = 0.9) as a function of the simulation box (L). Blue circles and squares are the computed Darken (Eq. (4.4)) and MS (Eq. (3.4)) diffusivities, respectively. Red circles and green squares are the corrected diffusivities according to the YH (Eq. (4.1)) and MSYH (Eq. (4.9))) corrections, respectively. Dashed lines show extrapolation to the thermodynamic limit and solid lines are the extrapolated values.

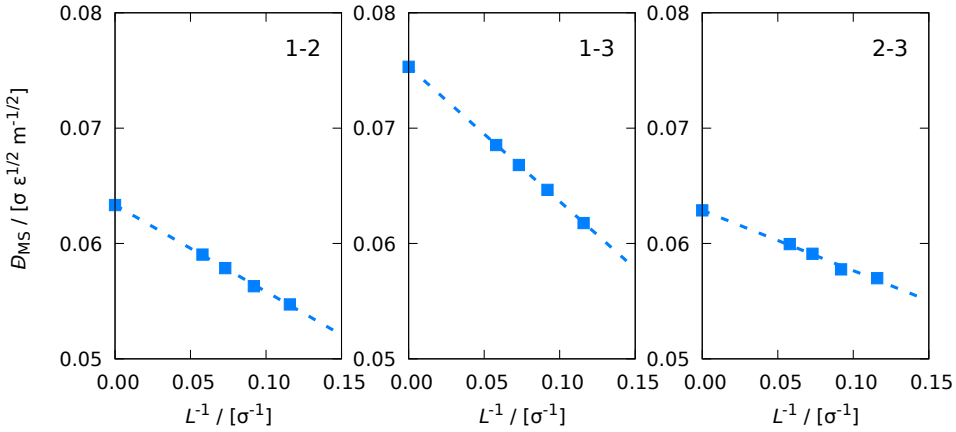

Figure 4.9: Finite-size MS diffusivities for a ternary LJ system (x_1 = 0.4, x_2 = 0.3, x_3 = 0.3) as a function of the simulation box (L) at a temperature of 0.65 and a pressure of 0.05. Subfigures 1-2, 1-3, and 2-3 indicate $Đ_{12}$, $Đ_{13}$, and $Đ_{23}$, respectively. Dashed lines show extrapolation to the thermodynamic limit. The LJ interaction parameters of species 1, 2, and 3 are $\epsilon_1 = \epsilon = 1.0$, $\epsilon_2 = 0.8$, and $\epsilon_3 = 0.6$, respectively. All species have the same size ($\sigma_1 = \sigma_2 = \sigma_3 = \sigma = 1.0$) and mass ($m_1 = m_2 = m_3 = 1.0$). Adjustable parameters to the Lorentz-Berthelot mixing rules (Eq. (4.5)) between species 1 and 2 (k_{12}), 1 and 3 (k_{13}), and 2 and 3 (k_{23}) are 0.05, 0.05, and 0.05, respectively. The elements of the thermodynamic factor matrix are: Γ_{11} = 0.559, Γ_{12} = −0.093, Γ_{21} = 0.062, and Γ_{22} = 0.847. Finite-size MS diffusivities are computed from 100 independent simulations. Error bars are smaller than the symbols.

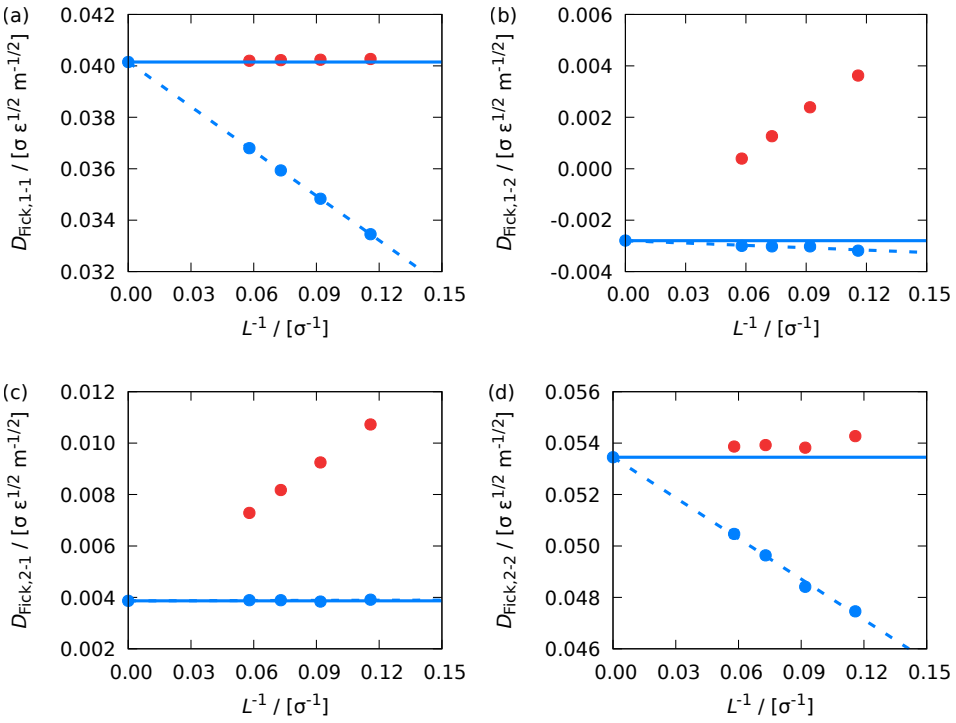

Figure 4.10: Finite-size Fick diffusivities (a) 1-1, (b) 1-2, (c) 2-1, and (d) 2-2 for a ternary LJ system ($x_1 = 0.4$, $x_2 = 0.3$, $x_3 = 0.3$) as a function of the simulation box (L) at the same conditions as in Fig. 4.9. Blue and Red circles indicate finite-size Fick diffusivies and corrected values by the YH correction, respectively. Dashed lines show extrapolation to the thermodynamic limit. The LJ interaction parameters of species 1, 2, and 3 are $\epsilon_1 = \epsilon = 1.0$, $\epsilon_2 = 0.8$, and $\epsilon_3 = 0.6$, respectively. All species have the same size ($\sigma_1 = \sigma_2 = \sigma_3 = \sigma = 1.0$) and mass ($m_1 = m_2 = m_3 = 1.0$). Adjustable parameters to the Lorentz-Berthelot mixing rules (Eq. (4.5)) between species 1 and 2 (k_{12}), 1 and 3 (k_{13}), and 2 and 3 (k_{23}) are 0.05, 0.05, and 0.05, respectively. Error bars are smaller than the symbols.

The mole fractions of the components of this system are: $x_1 = 0.4$, $x_2 = 0.3$, and $x_3 = 0.3$. All species have the same size ($\sigma_1 = \sigma_2 = \sigma_3 = \sigma = 1.0$) and mass ($m_1 = m_2 = m_3 = 1.0$). To create an asymmetric mixture, the LJ interaction parameters of species 1, 2, and 3 are $\epsilon_1 = \epsilon = 1.0$, $\epsilon_2 = 0.8$, and $\epsilon_3 = 0.6$, respectively. The adjustable parameter to the Lorentz-Berthelot mixing rules (k_{ij}) are: $k_{12} = 0.05$, $k_{13} = 0.05$, and $k_{23} = 0.05$. In Fig. 4.9, MS diffusion coefficients are shown for four system sizes (500, 1000, 2000, and 4000 molecules) and the extrapolated values to the thermodynamic limit. It can be seen that each MS diffusivity, $Đ_{ij}$, requires a different value of finite-size correction. It was shown in Eq. (4.10) that finite-size effect of Fick diffusivities for binary mixtures can be corrected by applying the YH correction. In Fig. 4.10, the Fick diffusion coefficients obtained from MS diffusivities and thermodynamic factors are shown. The elements of the thermodynamic factor matrix are: $\Gamma_{11} = 0.559$, $\Gamma_{12} = -0.093$, $\Gamma_{21} = 0.062$, and $\Gamma_{22} = 0.847$. From Fig. 4.10, it can be seen that the YH correction can correctly be used to correct finite-size effects of the diagonal elements of the Fick diffusion matrix. However, finite-size effects of the off-diagonal elements are very small and the YH correction should not be applied. From this figure, it may be concluded that off-diagonal elements of the Fick diffusion matrix do not show any system-size dependency while the finite-size effects of the diagonal elements can be corrected by using the YH correction. This is, however, an observation only for a single system. Further investigation is needed to confirm this observation and to provide guidelines for finite-size corrections to mutual diffusion coefficients of multicomponent mixtures.

4.5. CONCLUSIONS

Molecular Dynamics is a powerful tool to predict binary diffusion coefficients of nonideal mixtures. Even with modern computers, the number of molecules used in a typical simulation is orders of magnitude lower than the thermodynamic limit; therefore, it is important to take into account finite-size effects when calculating diffusion coefficients. Yeh and Hummer have developed a correction term (D^{YH}) to compensate for the finite-size effects of self-diffusion coefficients of pure fluids. This correction is a function of only the shear viscosity and the length of the simulation box. In this work, the applicability of this correction to a wide range of nonideal binary mixtures was verified. Based on the work of Yeh and Hummer, the Maxwell-Stefan YH correction, $Đ^{\mathrm{MSYH}}$, was presented for finite-size effects of computed Maxwell-Stefan diffusion coefficients, $Đ^{\mathrm{MSYH}} = D^{\mathrm{YH}}/\Gamma$, in which Γ is the thermodynamic factor. This correction is verified for a large set of Lennard-Jones systems as well as several molecular mixtures, and excellent predictions are obtained. For mixtures with a thermodynamic factor close to zero (i.e., close to demixing), this correction may become even larger than

the computed finite-size Maxwell-Stefan diffusion coefficient. This highlights the importance of the finite-size corrections. In future work, a similar correction may be derived for multicomponent mixtures, in which the formulation of Maxwell-Stefan diffusivities seems to be much more complex than those for binary mixtures.

5

COMPUTATION OF SHEAR VISCOSITIES FROM FINITE-SIZE SELF-DIFFUSIVITIES

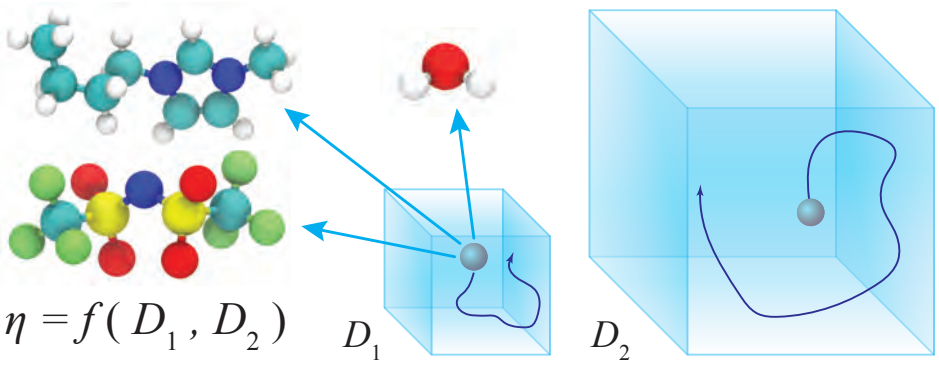

This chapter is based on the papers: S.H. Jamali, R. Hartkamp, C. Bardas, J. Soëhl, T.J.H. Vlugt, and O.A. Moultos, *Shear Viscosity Computed from the Finite-Size Effects of Self-Diffusivity in Equilibrium Molecular Dynamics*, Journal of Chemical Theory and Computation, **14**, 5959-5968 (2018) [259].

5.1. INTRODUCTION

In equilibrium Molecular Dynamics (EMD), the shear viscosity is computed from time correlations of the components of the stress tensor (see Eq. (3.28)) [36]. Since the stress tensor is defined for the entire simulation box, the shear viscosity is a property of the system as a whole. This means that an increase in the system size does not improve the statistical uncertainty of the computed shear viscosity [30]. Due to the slow relaxation of highly viscous fluids such as ionic liquids [288, 289] and deep eutectic solvents [290], and due to the large fluctuations in the components of the stress tensor [108] , very long MD simulations are required to sufficiently sample the stress tensor components.

Unlike the shear viscosity, the self-diffusivity is a single-molecule property and can be calculated from the mean squared displacement (MSD) of all individual molecules of the same species [35, 36, 107, 254]. The statistical uncertainties of self-diffusivities decrease as the number of molecules in the system increases [30, 250, 291]. The simulation length needed to obtain a linear relation between the MSD and time is much smaller than the length of an MD simulation required for computing the shear viscosity. Therefore, accurate self-diffusivities can be computed from short MD simulations with a large number of molecules. In the same short simulation, such a high accuracy cannot be achieved for the shear viscosity due to the smaller number of samples for the stress tensor components [30].

As shown in Chapter 4, in the case of transport properties, self-diffusion coefficients computed from MD simulations depend strongly on the system size while the shear viscosity does not show any system-size dependency [118, 262, 263]. Since there is an analytic relation to correct this finite-size effect (Eq. (4.1)), this relation can be used to compute the shear viscosity of a system if computed self-diffusivities for several system sizes are available. In the studies by Spångberg et al. [292], Kühne et al. [293], and others [281, 294, 295], the shear viscosities and self-diffusivities of water in the thermodynamic limit were calculated from Eq. (4.1). In these studies, several systems sizes were used to compute finite-size self-diffusivities, which were then fitted with a linear regression. However, the computation of shear viscosities from finite-size self-diffusivities has not been considered previously for multicomponent mixtures or highly viscous liquids. In this chapter, weighted least-squares linear regression analysis is used to develop a well-structured methodology for computing shear viscosities from finite-size effects of self-diffusivities. To allocate the available computational resources efficiently, a set of guidelines for choosing simulation parameters, such as the optimum number of system sizes and their size differences is provided. The application of the proposed method is verified for pure water, a large number of binary and ternary LJ systems, and the ionic liquid [Bmim][Tf_2N].

This chapter is organized in five sections. The proposed method is described in Section 5.2. In Section 5.3, details of MD simulations are briefly explained. The results of the MD simulations for pure water, binary and ternary LJ systems, and [Bmim][Tf_2N] are discussed in Section 5.2, along with a set of guidelines for the efficient use of the proposed method. The conclusions are provided in Section 5.5.

5.2. METHOD

To develop a systematic method to compute shear viscosities from the finite-size effects of self-diffusivities, the finite-size correction developed Eq. (4.1) can be rewritten in a linear form $y = ax + b$:

$$D_{\text{self}}^{\text{MD}} = \left(\frac{1}{\eta}\right)\left(-\frac{\xi k_{\text{B}} T}{6\pi L}\right) + D_{\text{self}}^{\infty} \tag{5.1}$$

where $-\xi k_{\text{B}} T/6\pi L$ and $D_{\text{self}}^{\text{MD}}$ are the independent and dependent variables, respectively. The intercept of this line with the vertical axis ($L \to \infty$) is the self-diffusivity in the thermodynamic limit, D_{self}^{∞}. The inverse of the slope is the shear viscosity of the fluid, η.

To compute the shear viscosity, this method uses self-diffusivities of at least two system sizes. For each system size, the average self-diffusivity and its variance can be estimated from the mean ($\bar{D}$) and sample variance (S^2) of the self-diffusivities computed from several independent simulations:

$$\bar{D} = \frac{1}{N_{\text{sim},j}} \sum_{k=1}^{N_{\text{sim},j}} D_k \tag{5.2}$$

$$S^2 = \frac{1}{N_{\text{sim},j} - 1} \sum_{k=1}^{N_{\text{sim},j}} \left(D_k - \bar{D}\right)^2 \tag{5.3}$$

where $N_{\text{sim},j}$ is the number of independent simulations for the j^{th} system size and D_k indicates the self-diffusivity computed from the k^{th} independent simulation for system size j. The parameters of interest ($1/\eta$ and $D_{\text{self}}^{\text{MD}}$) are then fitted to Eq. (5.1) with a weighted least-squares linear regression [251]. The linear regression analysis requires the standard errors ($S.E.$) of the average self-diffusivities for all system sizes. The inverse of squared standard errors are used as the weighting factors for each data point. Since no prior knowledge of these standard errors is available, the standard error of the self-diffusivity of each system size can be estimated from the sample variance:

$$S.E. = \sqrt{S^2 / N_{\text{sim},j}} \tag{5.4}$$

According to the work of Pranami and Lamm [250], multiple independent simulations are required to correctly compute the sample variance of the mean self-diffusivity. For a single MD simulation, the computed MSD depends on the initial configuration regardless of the simulation length. Weighted least-squares linear regression analysis yields both the averages and the variances of the parameters in Eq. (5.1). The self-diffusivity in the thermodynamic limit is a direct outcome of this analysis. The average shear viscosity is equal to the inverse of the average slope of the fitted line, $\bar{a}$. If this slope has a statistical uncertainty of δa, the statistical uncertainty of the shear viscosity, $\delta\eta$, can be calculated from error propagation:

$$\delta\eta = \frac{\delta a}{\bar{a}^2} \tag{5.5}$$

In Chapter 4, it is shown that that finite-size corrections to self-diffusivities of different species in a mixture are identical and equal to the YH correction (Eq. (4.1)) [263]. This conclusion is based on a detailed study of 250 binary LJ systems with a wide range of LJ energy (ϵ), size (σ), and mass (m) ratios. The results suggest that the shear viscosity of a mixture can be predicted from the finite-size effects of the self-diffusivity of each species regardless of the mass or size ratios. To maximize the statistical information of a single simulation, a new quantity is introduced: the average self-diffusivity (D_{avg}). This quantity is the arithmetic mean of the self-diffusion coefficients of all species, weighted by their corresponding mole fractions. By using the definition of the MSD in multi-component mixtures (Eq. (3.1)) [224, 226, 227], it can be shown that the average self-diffusivity, D_{avg}, is constructed from the self-diffusion of all molecules in the mixture:

$$\begin{aligned}
D_{\text{avg}} &= \sum_{i=1}^{n} x_i D_{i,\text{self}} \\
&= \sum_{i=1}^{n} x_i \left[\lim_{t\to\infty} \frac{1}{6t} \frac{1}{x_i N} \left\langle \sum_{j=1}^{N_i} \left(\boldsymbol{r}_{j,i}(t) - \boldsymbol{r}_{j,i}(0) \right)^2 \right\rangle \right] \\
&= \sum_{i=1}^{n} \left[\lim_{t\to\infty} \frac{1}{6t} \frac{1}{N} \left\langle \sum_{j=1}^{N_i} \left(\boldsymbol{r}_{j,i}(t) - \boldsymbol{r}_{j,i}(0) \right)^2 \right\rangle \right] \\
&= \lim_{t\to\infty} \frac{1}{6t} \frac{1}{N} \left\langle \sum_{i=1}^{n} \sum_{j=1}^{N_i} \left(\boldsymbol{r}_{j,i}(t) - \boldsymbol{r}_{j,i}(0) \right)^2 \right\rangle
\end{aligned} \tag{5.6}$$

where n and N are the total number of species and molecules in the mixture, respectively. x_i is the mole fraction of species i. Since the self-diffusivities of all species experience an identical finite-size effect [263], the same YH correction

(Eq. (4.1)) can be applied to D_{avg}:

$$\begin{aligned} D^{\infty}_{\text{avg}} &= \sum_{j=1}^{n} x_j D^{\infty}_{j,\text{self}} \\ &= \sum_{j=1}^{n} x_j \left(D^{\text{MD}}_{j,\text{self}} + D^{\text{YH}} \right) \\ &= D^{\text{MD}}_{\text{avg}} + D^{\text{YH}} \end{aligned} \tag{5.7}$$

By combining Eqs. (5.1) and (5.7), the shear viscosity of a mixture can be obtained from D_{avg}, similar to the approach used for pure liquids. Hereafter, the proposed method will be called the D-based method, and $\eta_{D\text{-based}}$ denotes the corresponding computed shear viscosity.

The D-based method can be used to compute shear viscosities of highly viscous systems such as ionic liquids and deep eutectic solvents. The shear viscosity of these systems can be as large as several hundred cP at room temperature [70, 290, 296, 297]. The length of MD simulations for computing self-diffusivities depends directly on how fast the constituent ions diffuse in the bulk liquid. In MD simulations, Fickian diffusion is observed at timescales in which a linear relation between the MSD and time (i.e., a slope of 1 on a log-log plot) is established [117]. However, this criterion does not ensure Gaussian diffusion, which corresponds to a Gaussian distribution for the displacement probability of ions [298]. Ionic liquids and deep eutectic solvents consist of highly associated pairs of ions and temporarily form cages [71]. While cage effects can also be present in simple fluids [42], it plays an important role in determining the minimum length of an MD simulation for ionic systems [71, 299]. As discussed in detail in the work of Casalegno et al. [71], for short timescales, each ion fluctuates around a certain position in the cage. Due to dynamical heterogeneity [71, 298, 300], a non-Gaussian distribution is observed for the diffusion probability of ions trapped in the cage. For longer timescales, ions jump from a cage to another. The displacement probability forms a Gaussian distribution corresponding to Gaussian diffusion [71]. According to Casalegno et al. [71], for room-temperature ionic liquids, a rough estimate of the timescale corresponding to Gaussian diffusion can be made based on a minimum average displacement of 1.5 nm for all constituent ions. This criterion ensures that the simulation time is sufficiently long for all ions to break the local ion cages and diffuse in the bulk liquid [299, 301]. This criterion can be used for room-temperature ionic liquids for performing long enough MD simulations to compute finite-size self-diffusivities with the D-based method.

Table 5.1: Specifications of 26 ternary LJ systems at a temperature of 0.65 and a pressure of 0.05. The LJ interaction parameters of species 1, 2, and 3 are $\epsilon_1 = \epsilon = 1.0$, $\epsilon_2 = 0.8$, and $\epsilon_3 = 0.6$, respectively. All species have equal sizes ($\sigma_1 = \sigma_2 = \sigma_3 = \sigma = 1.0$) and masses ($m_1 = m_2 = m_3 = 1.0$). All values are reported in reduced units [36]. x_i indicates the mole fraction of species i, where $x_1 = 0.4$, $x_2 = 0.3$, and $x_3 = 0.3$.

Parameters	Values
k_{12}	0.05, -0.3, -0.6
k_{13}	0.05, -0.3, -0.6
k_{23}	0.05, 0.0, -0.3, -0.6

5.3. SIMULATION DETAILS

To validate the D-based method, three different systems are considered: binary and ternary LJ systems, pure water, and the ionic liquid [Bmim][Tf_2N]. All MD simulations are carried out with LAMMPS (version 16 Feb. 2016) [126]. The order-n algorithm [117] is employed for an efficient sampling of time correlations for the calculation of self-diffusivities and shear viscosities by using the OCTP plugin, presented in Chapter 3, for LAMMPS [210]. All raw data of the simulations are reported in the Supporting Information of the work of Jamali *et al.* [259].

MD simulations of 250 binary and 26 ternary LJ systems were carried out. Simulation details of the 250 binary LJ systems are available in Section 4.3. For the interaction between dissimilar LJ particles (i and j), the Lorentz-Berthelot mixing rules with a modification factor (k_{ij}) is used (see Eq. (4.5)). The simulation parameters of ternary systems are provided in Table 5.1. All parameters are reported in reduced units, where $\sigma_1 = \sigma = 1$, $\epsilon_1 = \epsilon = 1$, and $m_1 = m = 1$ (mass) are the basis units [36]. All LJ interactions are truncated and shifted at a cutoff radius of 4σ. Simulations for two system sizes (500 and 4000 LJ particles) were performed at a reduced temperature of 0.65 and a reduced pressure of 0.05. The number densities of the ternary systems are in the range of 0.78 - 0.88. An integral timestep of 0.001 is used and the simulation length of the ternary systems is 100 million timesteps.

For the molecular systems, the initial configurations were made in PACKMOL [286] and the LAMMPS input files were created with VMD [200]. The three-site SPC/E model is used for water [260]. The force field parameters of [Bmim][Tf_2N] are obtained from the work of Zhang et al. [102]. The LJ interactions for water and the ionic liquid are truncated at 9 and 12 Å, respectively, with analytic tail corrections considered for energy and pressure [36]. The particle-particle particle-mesh (PPPM) method with a relative precision of 10^{-6} is used for the long-range electrostatic interactions [36]. The Verlet algorithm is used to integrate Newton's

equations of motion with a timestep of 1 fs. MD simulations for water performed at 298 K and 1 atm. MD simulations of [Bmim][Tf_2N] were performed at three temperatures of 300 K, 400 K, and 500 K and a pressure of 1 atm. The simulation times used for computing shear viscosities of water and [Bmim][Tf_2N] are 50 and 200 ns, respectively. Self-diffusivities of water and [Bmim][Tf_2N] are computed from independent simulations of 0.5 ns and 20 ns, respectively. Due to the slow relaxation of [Bmim][Tf_2N] at 300 K, MD simulations of 50 ns and 450 ns are needed to obtain the self-diffusivities and shear viscosity at this low temperature, respectively. The choice of these simulation lengths is made so that a minimum average displacement of 1.5 nm is obtained for all systems (as discussed thoroughly in Section 5.2).

5.4. RESULTS AND DISCUSSIONS

5.4.1. PURE WATER

A set of simulations consisting of seven system sizes 250, 500, 1000, 2000, 4000, 8000, and 16000 water molecules was carried out. The average self-diffusivities were obtained from 100 independent simulations of 0.5 ns for each system size. In Fig. 5.1a, the average self-diffusivities of water are shown as a function of the system size. These finite-size self-diffusivities lie on the fitted line to Eq. (5.1):

$$D_{\text{water,self}} = \left(-2.818N^{-1/3} + 2.870\right) / \left[10^{-9}\text{m}^2\text{s}^{-1}\right] \tag{5.8}$$

where N equals the number of water molecules in the simulation box. From the intercept with the vertical axis, the self-diffusivity of the SPC/E water model in the thermodynamic limit at 298 K and 1 atm is estimated to be 2.870 ± 0.004 $10^{-9}\text{m}^2\text{s}^{-1}$ and the shear viscosity 0.708 ± 0.014 cP. The shear viscosity of water computed from the Einstein relation (Eq. (3.28)) is 0.694 ± 0.010 cP. These two values are in excellent agreement, considering the wide range of shear viscosities reported in the literature for the SPC/E water model at the same conditions: 0.68 [294], 0.71 [292], 0.729 [302, 303], and 0.82 [304] cP. This agreement confirms the applicability of the D-based method for pure water.

The extensive data set of finite-size water self-diffusivities provides a suitable estimation of the variances (S^2) and the standard deviations (S) of self-diffusivities as a function of the system size. These standard deviations will be used in the next section for optimizing the D-based method. Fig. 5.1b shows the estimated standard deviations as a function of the number of molecules ($N^{-1/3}$). Since no prior knowledge of the functional form is available, an initial guess for the functional form would be a power-law function (aN^b) with two fitting parameters:

$$S_{\text{water}} = \left(2.53N^{-0.31}\right) / \left[10^{-10}\text{m}^2\text{s}^{-1}\right] \tag{5.9}$$

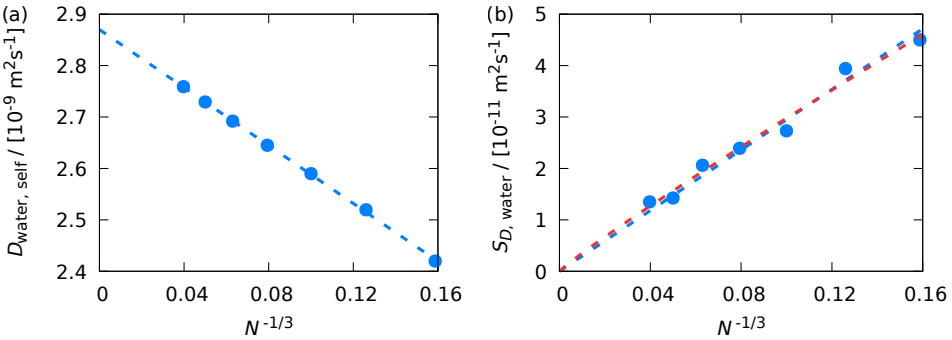

Figure 5.1: Computed (a) average finite-size self-diffusion coefficients of the SPC/E water model and (b) their estimated standard deviations at 298 K and 1 atm. Seven system sizes are considered: N = 250, 500, 1000, 2000, 4000, 8000, and 16000 water molecules. 100 independent simulations of 0.5 ns were performed for each system size to obtain the averages and standard deviations. The blue dashed lines in figure (a) is fitted with the weighted least-squares linear regression (Eq. (5.8)) to the YH equation (Eq. (5.1)). The red and blue dashed lines in subfigure (b) are fits to a power-law (Eq. (5.9)) and a linear function (Eq. (5.10)), respectively.

The exponent -0.31 and the linear arrangement of the data points in Fig. 5.1b suggest that the standard deviation can also be a linear function in $N^{-1/3}$, which decreases the number of fitting parameters to one ($aN^{-1/3}$) :

$$S_{\text{water}} = \left(2.95N^{-1/3}\right) / \left[10^{-10}\text{m}^2\text{s}^{-1}\right] \tag{5.10}$$

Both Eq. (5.10) and Eq. (5.8) will be used as a model for the normal distribution of finite-size self-diffusivities of water as a function of system size in the next part.

5.4.2. OPTIMIZATION

In this part, a set of optimum simulation parameters for which the computed shear viscosities have a minimum statistical uncertainty is proposed. The following parameters are considered: the number of system sizes, the size difference between systems, and the allocation of computational resources to each system size. The size difference between system i and system j is normalized by the size of the smallest system (system 1): $\left(N_j - N_i\right)/N_1$. According to the work of Moultos et al. [262], the smallest system should contain at least 250 molecules. This criterion ensures that the YH correction (Eq. (4.1)) provides an accurate prediction for the finite-size effects of self-diffusivities. As a constraint on the optimization problem, the total computational resources are fixed. The computational resources scale linearly with the number of independent simulations ($N_{\text{sim},i}$) and

polynomially with the number of molecules (N_i) in the simulation box, depending on computer hardware, the employed computational methods, and the scalability of MD simulations [36]. Thus, the ratio, α, between the computational resources allocated to system i and system j is:

$$\alpha = \frac{\text{computational resources of system } j}{\text{computational resources of system } i} = \frac{N_{\text{sim}\,j}}{N_{\text{sim},i}} \left(\frac{N_j}{N_i} \right)^{\gamma} \tag{5.11}$$

where γ indicates the scalability of MD simulations. Two values of γ are considered here for the scalability of MD simulations: $\gamma = 1$ and 2. For $\gamma = 1$, computational requirements grow linearly with the system size. For $\gamma = 2$, the growth in computational requirements is quadratic and thus faster than the linear growth. Current state-of-the-art MD packages [126, 305, 306] have a good computational scalability, γ, close to 1.

The simulation results presented for the SPC/E water model can be used as a basis for finding the optimum combination of the simulation parameters for the D-based method. Eqs. (5.1) and (5.10) are used to model the average and standard deviation of finite-size self-diffusivity of water as a function of system size. This model enables us to predict the self-diffusivity of water for a hypothetical MD simulation with a specified number of molecules. This can be achieved by generating a random number from a normal distribution with a mean self-diffusivity and a standard deviation determined by Eqs. (5.8) and (5.10). For a set of simulations with a number of system sizes and independent simulations per system size, a set of finite-size self-diffusivities is constructed and the corresponding shear viscosity is calculated from the D-based method. Since this shear viscosity depends on the set of finite-size self-diffusivities, the procedure should be repeated for many times and all shear viscosities are recorded in a histogram. For a specific set of simulation parameters, the data stored in the histogram yield an estimate for the variance (S^2) and standard deviation (S) of the shear viscosity. The aim of this optimization procedure is to find the simulation parameters that minimize the standard deviation (S) of the shear viscosity.

The first scenario considered here is the optimization for two system sizes. The simulation parameters studied are: (1) the normalized size difference ($(N_2 - N_1)/N_1$), and (2) the ratio between the computational resources allocated to system 1 and 2 (α). The objective function is the estimated standard deviation of shear viscosities normalized by S_{min}, the global minimum estimated standard deviation of the shear viscosity for a specified value of γ and all values of α and $(N_2 - N_1)/N_1$. In Fig. 5.2, the normalized estimated standard deviations (S/S_{min}) are shown for several values of α, ranging from 0.2 to 5.0, and the two values of γ. As can be seen in Fig. 5.2, a range of α between 1 and 2 yields the smallest value of S/S_{min}. This means that the number of independent simulations for each system

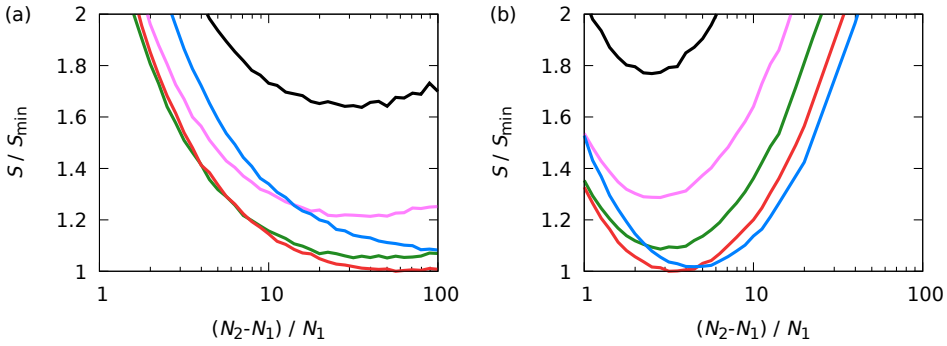

Figure 5.2: Normalized estimated standard deviation ($S/S_{\min}$) of the shear viscosity as a function of the normalized size difference between two systems ($(N_2-N_1)/N_1$). The total amount of computational resources is fixed. Different colors indicate various ratios (α) of the computational resources allocated to large and small system sizes (Eq. (5.11)): 0.2 (black), 0.5 (magenta), 1.0 (green), 2.0 (red), and 5.0 (blue). Two types of scalability for MD simulations are considered: (a) high scalability ($\gamma = 1$) and (b) low scalability ($\gamma = 2$).

size should be distributed in such a way that 50%-70% of the computational resources is allocated to the large system. Furthermore, it can be observed that the large system should be at least 4 times the small system. Depending on the scalability of MD simulations, the optimum normalized size difference ($(N_2-N_1)/N_1$) ranges from 3 ($\gamma = 2$) to 40 ($\gamma = 1$).

A similar investigation can be carried out for three system sizes. Here, α is set to 1, indicating that the computational resources are equally distributed between the three system sizes. In Fig. 5.3, normalized estimated standard deviations ($S/S_{\min}$) are shown as a function of the normalized size difference between the small and medium systems ($(N_2-N_1)/N_1$), and the medium and large systems ($(N_3-N_2)/N_1$). Fig. 5.3a ($\gamma = 1$) shows that a minimum cost function ($S/S_{\min}$) is achieved for $(N_2-N_1)/N_1 > 10$. This suggests that while the choice of the size difference between the small and medium systems is important, the size difference between the medium and large systems does not play a significant role. For very small values of the normalized size difference between the medium and large systems ($(N_3-N_2)/N_1 \rightarrow 0$), it can be deduced that the optimization problem reduces to a problem of two system sizes, which has already been discussed. In Fig. 5.3b, this is also observed for $\gamma = 2$. The optimum condition is achieved at $(N_2-N_1)/N_1 = 3$, which is in agreement with what is shown in Fig. 5.2b for two system sizes. This suggests that the optimum condition observed for three system sizes can also be achieved with two systems.

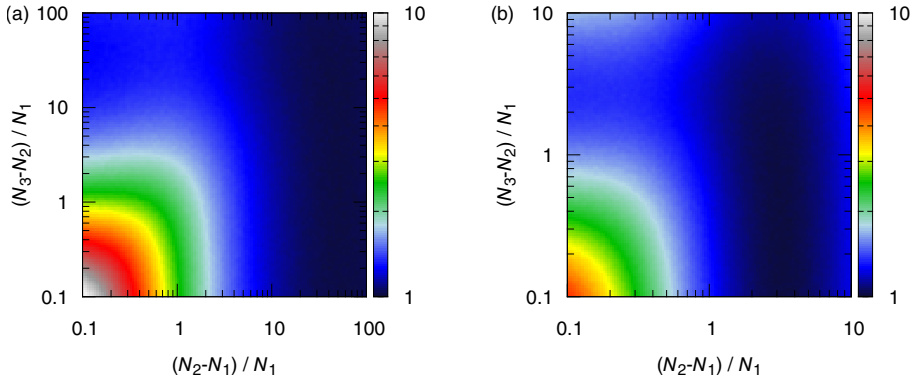

Figure 5.3: Normalized estimated standard deviations (S/S_{min}) of the shear viscosities as a function of the normalized size difference between small and medium systems ($(N_2 - N_1)/N_1$), and between medium and large system sizes ($(N_3 - N_2)/N_1$). A fixed amount of computational resources is equally distributed between the three system sizes. Two types of scalability for the MD simulations are considered: (a) high scalability ($\gamma = 1$) and (b) low scalability ($\gamma = 2$).

Based on the optimization results, the use of either two or three system sizes yields optimum shear viscosities. In the case of a limited amount of computational resources, adding more system sizes leads to a smaller number of independent simulations per system size. As a consequence, the limited number of independent simulations leads to poor sampling that may not yield an accurate average and standard deviation for self-diffusivities. This adversely affects the accuracy of average finite-size self-diffusivities and consequently the computed shear viscosity. Hence, the use of more than two system sizes is not justified. The choice of the optimum conditions may vary depending on the MD software [126, 305, 306] as well as the algorithms used in the software (e.g., handling of long-range electrostatic interactions, details of the neighbor lists [36]). These specifications determine the optimum size of the system and number of independent simulations according to the results shown in Fig. 5.2, and consequently affect the computational requirements of the D-based method.

5.4.3. LENNARD-JONES SYSTEMS

To examine the accuracy of the D-based method for multicomponent fluid mixtures, the shear viscosities of 250 binary and 26 ternary LJ systems were computed. The comparison between the D-based shear viscosities and those com-

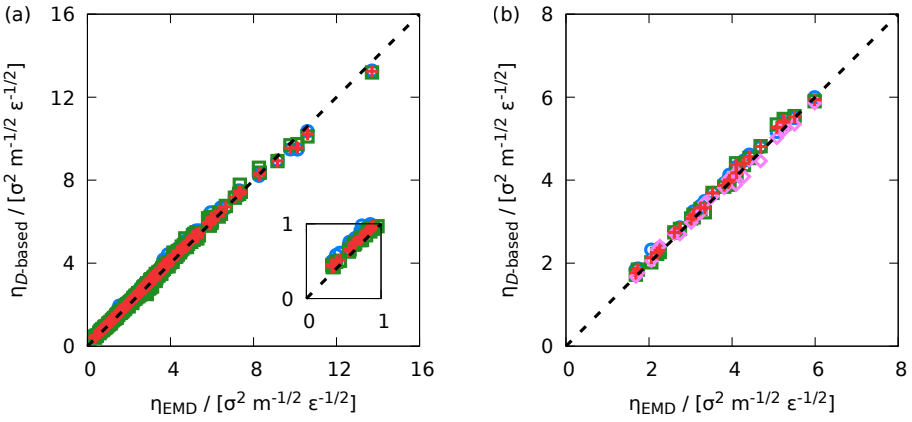

Figure 5.4: Comparison between the shear viscosities of (a) 250 binary and (b) 26 ternary LJ systems computed from the Einstein relation (η_{EMD}, Eq. (3.28)) and the D-based method ($\eta_{D\text{-based}}$, Eq. (5.1)) at a reduced temperature of 0.65 and a reduced pressure of 0.05. The D-based shear viscosities are computed from the self-diffusion coefficients of species 1 (blue circles), species 2 (green squares), and species 3 (purple diamonds; only for ternary systems) as well as the average self-diffusivity (Eq. (5.6), red crosses). Error bars are omitted for clarity.

puted from the Einstein relation (η_{EMD}, Eq. (3.28)) are shown in Fig. 5.4. By varying the characteristics of the studied LJ systems as mentioned in Tables 4.1 and 5.1, a wide range of shear viscosities is covered. While all data points show a good agreement between the two methods, the smallest deviation from the diagonal dashed lines is on average observed for the quantity D_{avg}, for both binary and ternary systems. This is expected since D_{avg} is constructed from the self-diffusivities of all species present in the mixture. Therefore, for multicomponent mixtures, D_{avg} should be used for calculating the shear viscosity rather than the self-diffusivity of only a single species.

In Fig. 5.4, the maximum deviation from the diagonal line, which represent perfect agreement between the D-based method and the Einstein relation, are observed for binary LJ systems with very low densities (inset of Fig. 5.4a). As discussed in Chapter 4, these outliers have very dissimilar size (σ_2/σ_1 of 1.4 or 1.6) and interaction (ϵ_2/ϵ_1 of 0.5 or 0.6) parameters. According to the work of Heyes et al. [307] for a hard-sphere fluid, the exponent $-1/3$ in $N^{-1/3}$ (i.e., L^{-1}) in Eq. (4.1) is valid only for a range of packing fractions. Since the validity of the YH correction have been shown for many real molecular liquids [118, 119, 262, 263], it is expected that the range of packing fractions for which the YH correction holds correspond to a liquid phase. From Fig. 5.5, a similar observation to the work of

Heyes et al. [307] can be made for LJ systems. In this figure, the normalized difference between the shear viscosities computed from the D-based method (using D_{avg}) and the Einstein relation is shown as a function of (a) the shear viscosity and (b) the density for all binary and ternary LJ systems. For LJ systems at high densities, a good agreement between the two methods is observed. For the systems with low densities/viscosities, shown also in the inset of Fig. 5.4, substantial deviations (up to 30%) between the D-based method and the Einstein relation are observed. Fig. 5.5 shows that as the density of a system decreases and thus hydrodynamic interactions become weaker, the scaling proposed by Yeh-Hummer does not hold anymore. At low densities, the finite-size effects of self-diffusivities do not scale as $N^{-1/3}$, and the exponent varies according to the packing fraction of the fluid (e.g., see the work of Heyes et al. [307].).

5.4.4. [BMIM][Tf_2N]

As a representative test case, shear viscosities of the ionic liquid [Bmim][Tf_2N] are calculated from the D-based method and the Einstein relation (Eq. (3.28)) at a pressure of 1 atm and three temperatures: 300 K, 400 K, and 500 K. MD simulations of 20 ns were performed for computing self-diffusivities of [Bmim][Tf_2N] at 400 K and 500 K. To fulfill the minimum average displacement criterion of 1.5 nm (explained in Section 2), the MD simulations at 300 K were carried out for 50 ns. According to the set of guidelines proposed for the D-based method, 40 and 8 independent MD simulations were performed for two systems of 150 and 1200 pairs of ions, respectively. In Fig. 5.6, the computed self-diffusivities for both [Bmim] and [Tf_2N] ions as well as D_{avg} are shown. It can be seen that the finite-size self-diffusivities of [Bmim] and [Tf_2N] greatly differ from each other, but the finite-size effects remain equal for both ions and D_{avg}. Therefore, shear viscosities computed from the slopes of the lines connecting finite-size self-diffusivities are equal within the error bars. Fig. 5.6 shows that the use of D_{avg} for the D-based method is not limited to molecular mixtures and that this quantity can be used for ionic systems as well.

Fig. 5.7 shows the computed shear viscosities of the ionic liquid as a function of temperature. The lines are the fits to the Vogel equation [14]:

$$\ln\left(\eta/[\mathrm{cP}]\right) = A + \frac{B}{T+C} \tag{5.12}$$

where A, B, and C are the coefficients of this equation. For all temperatures, a good agreement is observed between the D-based method, the Einstein relation (Eq. (3.28)), and the estimates of shear viscosities from the work of Zhang et al. [102]. This agreement confirms the applicability of the D-based method to complex and highly viscous mixtures of non-spherical molecules/ions. To compute

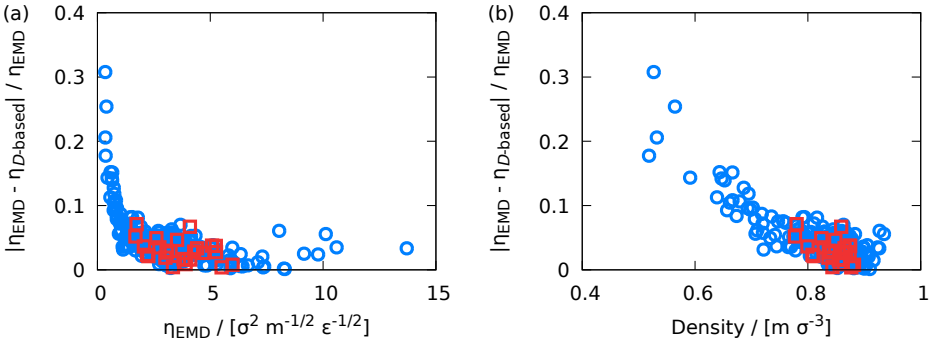

Figure 5.5: Normalized absolute difference between shear viscosities computed from the Einstein relation and the D-based method as a function of (a) the shear viscosity and (b) the density. Data are shown for binary (blue circles) and ternary (red squares) LJ systems at a temperature of 0.65 and a pressure of 0.05. The D-based method shear viscosities are computed from average self-diffusivities (D_{avg}).

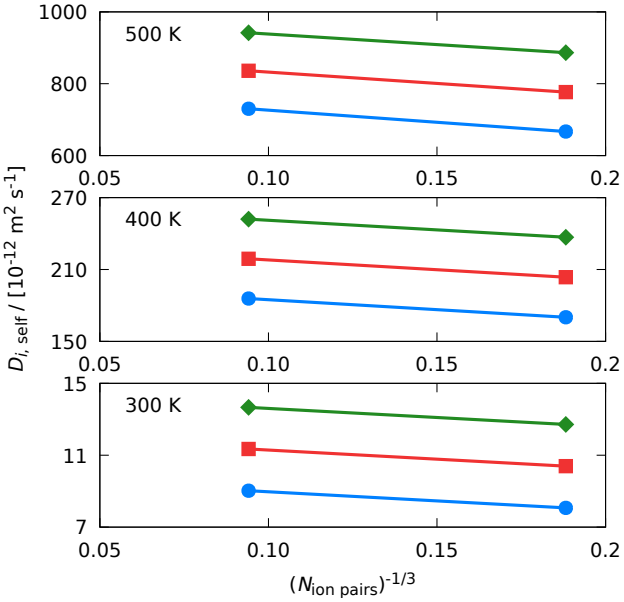

Figure 5.6: Computed self-diffusion coefficients of [Bmim][Tf_2N] at 300, 400, and 500 K and 1 atm. 40 and 8 independent simulations were performed for two system sizes of 150 and 1200 ion pairs, respectively. Self-diffusivities are shown for [Bmim] (blue circles), [Tf_2N] (green diamonds), and D_{avg} (red squares). The slope of the line connecting each two points yields the shear viscosity. The simulation length at 400 K and 500 K is 20 ns. Simulations at 300 K were performed for 50 ns. Error bars are smaller than the symbol sizes.

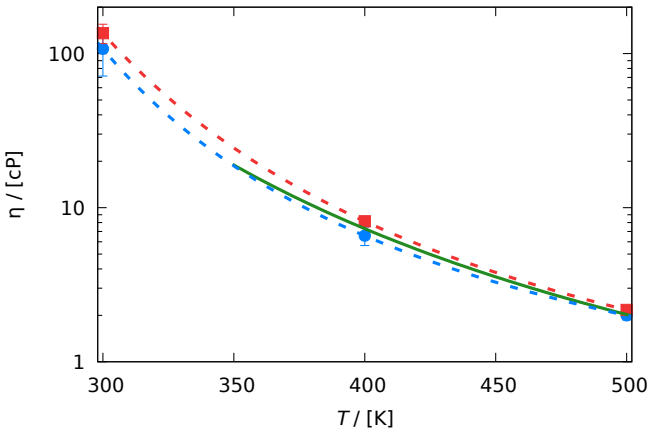

Figure 5.7: The shear viscosity of [Bmim][Tf_2N] as a function of temperature at 1 atm, computed from the D-based method (blue circles, Eq. (5.1)) and the Einstein relation (red squares, Eq. (3.28)). The lines are fits to the Vogel equation [14] (Eq. (5.12)) for the D-based method (blue dashed, Eq. (5.1)), Einstein relation (red dashed), and Green-Kubo relation (green solid; data extracted from the work of Zhang et al. [102]).

the shear viscosity of any ionic liquid or deep eutectic solvents, the set of guidelines for the D-based method along with the criterion on the minimum average displacement can be used to specify an optimum set of MD simulations.

5.5. CONCLUSIONS

A systematic methodology, called the D-based method, is proposed for accurately computing the shear viscosity of a liquid from the finite-size effects of self-diffusivities. The computational requirements of this method and the statistical uncertainty of the computed viscosity are comparable to the conventional methods, e.g., the Einstein relation. By performing weighted least-squares linear regression analysis, the shear viscosity can be computed from the slope of a line fitted to computed finite-size self-diffusivities. To obtain accurate shear viscosities at a minimum computational requirement, a set of guidelines for this method was proposed. The optimum number of system sizes is two, and depending on the available computational resources and the scalability of the MD simulations, the large system size should be 4 to 40 times the small system size. The number of independent simulations per system size should be assigned in such a way that 50% to 70% of the computational resources is allocated to the MD simulations of the large system. For multicomponent mixtures, the D-based method performs best when the average self-diffusivity of all species (D_{avg}) is used instead

of using the self-diffusivity of a single species. The D-based method was verified for pure water, a large number of binary and ternary Lennard-Jones systems, and an ionic liquid ([Bmim][Tf_2N]). The results of the D-based method were in good agreement with those obtained from the Green-Kubo and Einstein relations for all molecular systems. These results suggest that the D-based method can be a potential method for computing shear viscosities of highly viscous liquids and multicomponent mixtures.

6

Optimizing Intermolecular Interactions of Carbohydrates

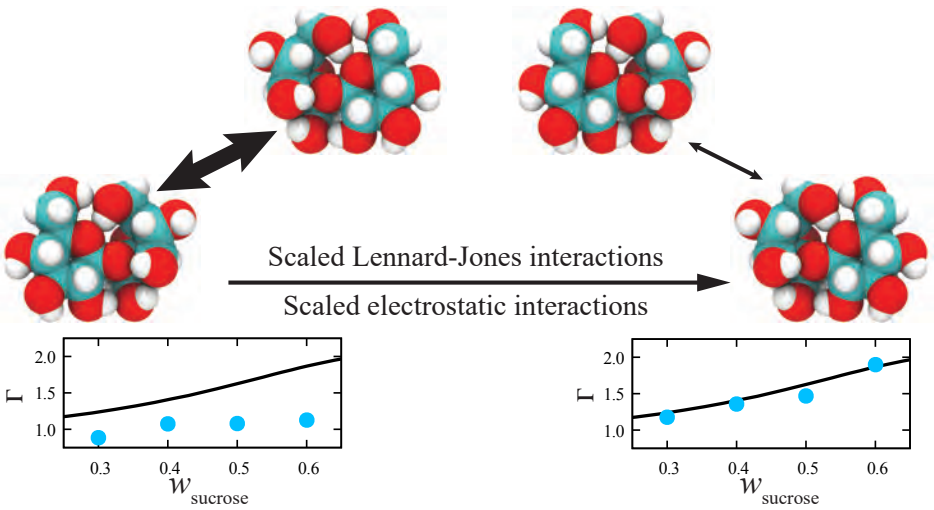

This chapter is based on the paper: S.H. Jamali, T. van Westen, O.A. Moultos, and T.J.H. Vlugt, *Optimizing Nonbonded Interactions of the OPLS Force Field for Aqueous Solutions of Carbohydrates: How to Capture Both Thermodynamics and Dynamics*, Journal of Chemical Theory and Computation, **14**, 6690-6700 (2018) [308].

6.1. INTRODUCTION

Saccharides define a class of carbohydrates considered vital for a wide range of biological- and industrial processes [69, 309]. Examples include the role of (poly-)saccharides or glyco-proteins in cryo- and lyo-preservation of biomaterials and foods [310–315], the regulation of the osmotic pressure in living cells [316], the interplay between saccharides and proteins in the cell membrane [317, 318], and the use as a feedstock for the production of biofuels and renewable chemicals in biotechnology [309]. Either in biology or in industrial applications, saccharides predominantly occur in aqueous solutions. To obtain a better understanding of the underlying mechanisms defining the biological function of a saccharide, or to obtain a better description of the thermophysical properties of saccharide solutions (as needed in technological applications), a molecular-level description of the interactions between sugars, water, and water-sugar is required. Classical molecular simulations provide a valuable tool for this; however, it is essential that the used force fields reproduce relevant volumetric, structural, and dynamic properties of the system of interest. For aqueous solutions of saccharides, this has proven a difficult task.

As several studies [50, 51, 319–322] have shown, a common problem when applying carbohydrate force fields such as CHARMM [90, 91, 323, 324], GLYCAM06 [325], GROMOS [73, 326], OPLS-AA [82, 83, 327], and MARTINI [328] to saccharide solutions is the overestimation of the sugar-sugar interactions, leading to strong sugar aggregation at elevated sugar concentrations. As a result, both thermodynamic properties (densities, activity coefficients, thermodynamic factors, second virial coefficients, etc.) and transport properties (shear viscosities, diffusion coefficients, etc.) of concentrated solutions are generally not well reproduced [50, 319–322]. Recent work showed that rescaling the sugar-sugar non-bonded interactions to lower values improves the description [89, 320, 321]. Basically, two strategies have been proposed. In the first approach (e.g., the work of Sauter and Grafmüller [50] and Lay et al. [321]), only the dispersion interactions—more precisely, the energy parameters for some of the Lennard-Jones (LJ) interactions between sugars—are modified. In the second approach (e.g., Batista et al. [320]), only the partial atomic charges of the sugars are scaled. The first approach improves the description of thermodynamic properties, such as the osmotic pressure and second virial coefficient [50, 321]. However, transport properties appear to be less affected by solely modifying the dispersion interactions (see the Supporting Information of the work of Lay et al. [321] for results on the viscosity of glucose solutions). Results obtained using the second approach indicate that rescaling partial atomic charges leads to considerable improvements in the description of transport properties, and suggest that thermodynamic properties (e.g., density) are also better described. The results of Batista

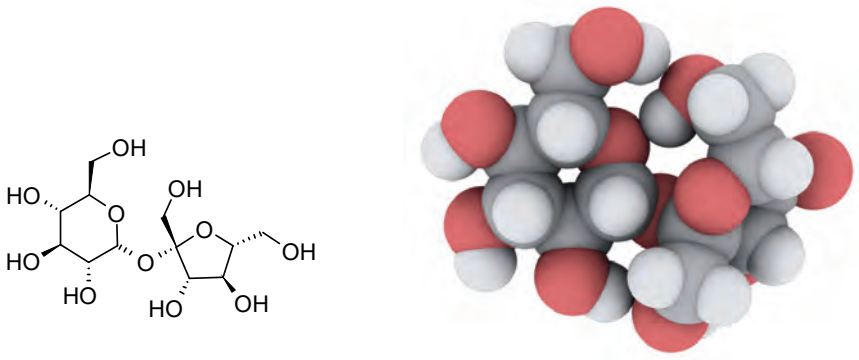

Figure 6.1: Schematic (left) and atomistic (right) representations of Sucrose. The atomistic representation was created using iRASPA [329].

et al. [320] are not conclusive, however, as mixture properties known to be more sensitive to changes in the partial charges (e.g., thermodynamic factors and osmotic coefficients) were not taken into account. Also, the only transport property studied was the viscosity, and diffusion coefficients were not considered.

In this chapter, a more complete analysis is presented on how the properties of aqueous carbohydrate solutions change when the LJ or electrostatic interactions are scaled, with the aim at elucidating whether scaling either dispersion interactions or partial electrostatic charges is sufficient to reproduce both, thermodynamic, and transport properties of concentrated aqueous saccharide solutions. The force fields of Batista et al. [320] (OPLS with scaled LJ interactions) and Lay et al. [321] (GLYCAM06 with scaled partial charges) are analyzed in more detail. The focus will be on the disaccharide sucrose (Fig. 6.1) as a relevant test case, as this molecule has many applications, ranging from biology to food science [310, 311, 313, 314]. The transferability of the refined OPLS force field is analyzed for D-glucose as a prototypical example of monosaccharides.

The results show that only scaling partial charges is insufficient to reproduce both thermodynamic and transport properties of concentrated aqueous saccharide solutions. Scaling only the dispersion interactions leads to significantly better agreement, with qualitative improvements in transport properties, as well as thermodynamic properties. Although scaling the LJ interactions improves the force field, obtaining quantitative agreement between experiments and computed properties of saccharide solutions may require a global optimization procedure of the force field, with different scaling factors for LJ interactions of different atom pairs. Since the choice of atom pairs is rather arbitrary, and an optimization of many force field parameters is difficult, here a different approach,

in which all LJ energy parameters and all partial atomic charges of the sugars are scaled simultaneously [89], can be proposed. This procedure only requires optimization of two parameters; one scaling factor for LJ interactions, and one scaling factor for partial atomic charges. For the optimization of sucrose non-bonded interaction parameters, the OPLS force field [82, 83] is used as a basis.

This chapter is organized as follows. In Section 6.2, the details of simulations are provided. In Section 6.3, a set of optimum scaling factors for non-bonded interaction parameters of the OPLS force field is obtained and the accuracy of the refined force field is investigated. The findings and main conclusions are summarized in the last section.

6.2. SIMULATION DETAILS

Force field-based equilibrium MD simulations were carried out to compute thermodynamic properties (i.e., liquid densities and thermodynamic factors) and transport properties (i.e., shear viscosities, self-, and Fick diffusion coefficients) of water-sucrose mixtures at 298 K and 1 atm. These thermodynamic properties are liquid densities and thermodynamic factors (Eq. (3.7)). The considered transport properties are self-diffusivities (Eq. (3.1)), Fick (mutual) diffusion coefficients (Eq. (3.6)), and shear viscosities (Eq. (3.28)). All finite-size effects in diffusion coefficients are corrected according to the details described in Chapter 4.

The software package LAMMPS [126] (version of 16 February 2016) was used to perform MD simulations. The OCTP plugin, presented in Chapter 3, was used to efficiently compute transport properties [210]. The molecular configurations of aqueous sucrose solutions were made in PACKMOL [286]. Five system sizes are considered with sucrose mass fractions (w_{sucrose}) of 20%, 30%, 40%, 50%, and 60%. These systems contained 6, 9, 12, 16, and 20 sucrose molecules combined with 456, 399, 342, 304, and 253 water molecules, respectively. These systems yield homogeneous liquid solutions, as sucrose crystallizes in mixtures with a mass fraction above 67% at 298 K [330]. The input files for these configurations are produced using VMD [200]. The same procedure was followed to construct LAMMPS input files for four aqueous glucose solutions. To create mixtures with glucose mass fractions (w_{glucose}) of 20%, 30%, 40%, and 50%, the systems contained 12, 18, 24, and 30 glucose molecules combined with 480, 420, 360, and 300 water molecules, respectively. At 298 K, α-D-glucose monohydrate forms in aqueous glucose solutions with mass fractions above 51% [331].

Two groups of force fields are considered for sucrose: GLYCAM06 [325] and OPLS-AA [82, 83]. The three-site SPC/Fw water model is used [332]. Non-bonded LJ interactions are truncated at a cutoff radius of 9 Å, and analytic tail corrections are included for the computation of energies and pressures [36]. The standard

mixing rules of the OPLS force field are applied for non-bonded LJ interactions between different atoms in different molecules, or atoms of the same molecule separated by at least 3 bonds [82]. The Lorentz-Berthelot mixing rules are considered for the GLYCAM06 force field [36]. The 1-4 non-bonded intramolecular interactions are scaled by a factor of 0.5 for the OPLS force field [82] and a factor of 0 for the GLYCAM06 force field [325]. Long-range electrostatic interactions are taken into account using the PPPM method with a relative precision of 10^{-6} [36]. The velocity-Verlet algorithm with a timestep of 1 fs is used to integrate the equations of motion [36].

Liquid densities are computed from an NPT ensemble, in which the temperature and pressure of the system are fixed by using the Nosé-Hoover thermostat and barostat [36]. All transport properties and thermodynamic factors are computed in an NVT ensemble, where the temperature is controlled by using the Nosé-Hoover thermostat [36]. The lengths of each simulation for computing transport and thermodynamic properties are 200 ns and (at least) 10 ns, respectively. To assert the the statistical uncertainties, 5 independent simulations were performed for each condition.

6.3. RESULTS AND DISCUSSIONS

In this section, several procedures for optimizing force fields of carbohydrate solutions are initially analyzed. The quality of a procedure is measured by the accuracy with which thermodynamic factors and shear viscosities are estimated. Once the optimal procedure is established, a refined OPLS force field for aqueous solutions of sucrose is developed and verified. The transferability of the refined force field to aqueous solutions of other carbohydrates is examined by considering glucose. The refined OPLS force field parameters for both sucrose and glucose are reported in the Supporting Information of the work of Jamali *et al.* [308]. A sample script for performing a simulation for the aqueous solution of each carbohydrate in LAMMPS is also provided.

6.3.1. ANALYSIS OF DIFFERENT OPTIMIZATION PROCEDURES

Batista et al. [320] studied the effects of non-bonded electrostatic interactions in the GROMOS $56A_{CARBO}$ and OPLS force fields for aqueous solutions of D-glucose. Their study concluded that the properties of diluted solutions can be predicted accurately based on the $56A_{CARBO}$ force field. At high glucose mass fractions ($w_{glucose} > 0.60$), the overestimated self-association of glucose molecules was shown to result in overestimation of shear viscosities by up to 650% [320]. To decrease the solute-solute interactions, all partial atomic charges of the glucose molecule were scaled by a factor 0.8. The estimation of shear viscosities of concentrated water-glucose mixtures was thereby improved significantly, with a

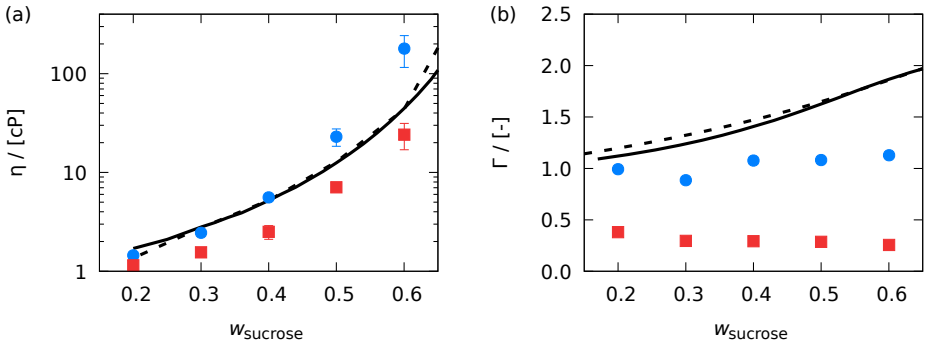

Figure 6.2: Computed (a) shear viscosities and (b) thermodynamic factors for water-sucrose mixtures as a function of the mass fraction of sucrose. The properties are computed based on the OPLS force field [82] (blue circles) and the OPLS force field with scaled partial atomic charges [320] (red squares), combined with the SPC/Fw water model [332]. Lines represent (a) experimental shear viscosities (solid [333], dashed [334]) and (b) thermodynamic factors (solid [335], dashed [336]). Error bars indicate 95% confidence intervals. No error bars are reported for the thermodynamic factors.

maximum deviation from experiments of 27% [320]. Besides an analysis on the density of the solution, these authors did not consider thermodynamic properties such as osmotic coefficients or thermodynamic factors to verify the performance of the optimized force field.

Inspired by the promising results of Batista et al. [320], a modified OPLS force field for which the partial atomic charges of sucrose are scaled by a factor 0.8 is studied. Similar to the work of Batista et al. [320], the LJ interactions parameters remain unchanged. In Fig. 6.2, thermodynamic factors and shear viscosities computed based on the original OPLS force field and the OPLS force field with scaled partial atomic charges are compared to experimental data at 298 K and 1 atm. In agreement with the results of Batista et al. [320], the overestimation of shear viscosities is decreased by scaling the electrostatic interactions. This is especially the case for mixtures of high concentrations of sucrose, where sucrose-sucrose interactions mainly determine the properties of the mixture. Thermodynamic factors are less accurately reproduced. The results show qualitatively incorrect changes as compared to the original OPLS force field, with larger deviations of thermodynamic factors from experiments. Estimated thermodynamic factors are closer to zero, meaning the self-association of sucrose has increased–not decreased. This suggests that merely scaling the partial atomic charges is insufficient to reproduce both thermodynamic and transport properties of carbohydrate solutions.

Another approach to optimizing a force field is to modify the LJ parameters of solute molecules. As a good rule of thumb, the size (σ) and energy (ϵ) parameters can be modified to improve the predictions of volumetric (e.g., liquid densities) and thermal (e.g., heat of vaporization) properties, respectively [69, 73, 327, 337]. In recent modifications of the MARTINI, CHARMM, and GLYCAM06 force fields for carbohydrate solutions [321, 322], only the energy parameters were changed. An example is the work of Lay et al. [321], in which the CHARMM and GLYCAM06 force fields were modified by altering some of the LJ energy parameters (ϵ_{ij}) defining the solute-solute interactions in aqueous solutions of glucose. Based on introducing modifications to carbon-carbon and carbon-oxygen interactions, accurate predictions of osmotic coefficients were obtained. However, shear viscosities were underestimated by about 60% [321].

The modified GLYCAM06 force field of Lay et al. is analyzed in more detail in Fig. 6.3. In this figure, computed thermodynamic factors and shear viscosities of water-sucrose mixtures are compared to results obtained based on the original GLYCAM06 force field. The modified energy parameters considerably improve the description of both properties, for a wide range of sucrose concentrations. Shear viscosities are especially well reproduced, showing a good agreement with experiments. The improved results for viscosity, as compared to those reported by Lay et al. [321], may be due to the use of the SPC/Fw water model instead of TIP3P. The TIP3P water model is known to provide poor estimates for the transport properties of water [291, 303, 338]. On the other hand, the SPC/Fw water model is one of the most accurate three-site models for estimating transport properties of water at ambient conditions [291, 332, 339]. The choice of a three-site water model is mainly due to the smaller computational requirements compared to more complex models such as four-site (e.g., TIP4P/2005 [340]), five-site (e.g., TIP5P-E [341]), and polarizable (e.g., HBP [342]) water models. An extensive comparison of the performance of different water models can be found in literature [291, 303, 337, 343]. Although thermodynamic factors are not as well described as shear viscosities, the observed increase in the thermodynamic factor is at least qualitatively correct. These results suggest that modifying the LJ energy parameters of solute molecules could be a sufficient procedure to develop a force field that accurately reproduces both thermodynamic and transport properties of carbohydrate solutions.

While the approach of Lay et al. seems effective, this approach may require the modification of the LJ energy parameters of many different atom pairs, each with its own scaling factor. The choice of atoms whose ϵ is changed requires a profound understanding of the interactions between the atoms of the carbohydrate, which is not always known a priori. This, combined with the fact that the optimization of many force field parameters usually proceeds by trial and error

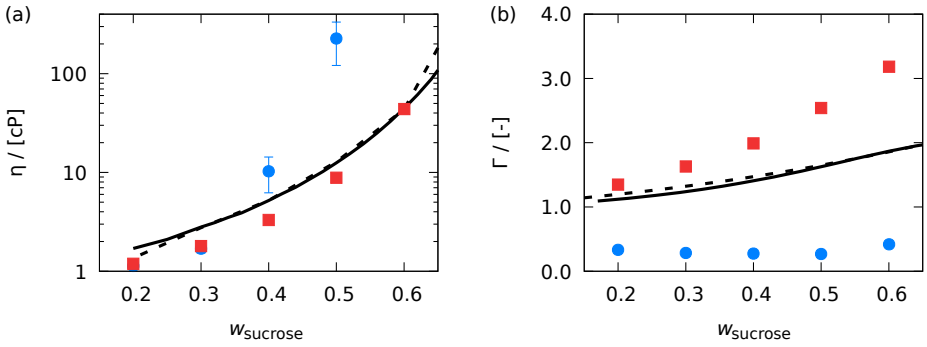

Figure 6.3: Computed (a) shear viscosities and (b) thermodynamic factors for water-sucrose mixtures as a function of the mass fraction of sucrose at 298 K and 1 atm. The properties are computed based on the GLYCAM06 force field [325] (blue circles) and a modified GLYCAM force field as proposed by Lay et al. [321] (red squares), in which some of the LJ sugar-sugar interactions are modified. The SPC/Fw water model was used [332]. Lines represent (a) experimental shear viscosities (solid [333], dashed [334]) and (b) thermodynamic factors (solid [335], dashed [336]). Error bars indicate 95% confidence intervals. No error bars are reported for the thermodynamic factors.

(and is thus computationally expensive), leads us to suggest a different approach. Based on the results shown in Figs. 6.2 and 6.3, scaling the partial atomic charges and LJ energy parameters of all atoms of the carbohydrate can be proposed to address the issue with the carbohydrate force fields. This can simultaneously improve the description of thermodynamic and transport properties, without requiring different scaling factors for different atom pairs. The non-bonded interaction parameters should be scaled in such a way that experimental data for at least one thermodynamic property (e.g., thermodynamic factors) and one transport property (e.g., shear viscosities) can be reproduced by the force field. The advantage of this approach over the method of Lay et al. [321] is a considerable reduction in the number of modification parameters to two: a single scaling factor for all LJ energy parameters of the carbohydrate, and a single scaling factor for all partial atomic charges of the carbohydrate.

6.3.2. REFINED OPLS FORCE FIELD

The optimization procedure proposed in the previous section is here applied to the OPLS force field, for aqueous solutions of sucrose. As in the previous section, thermodynamic factors and shear viscosities are considered as target properties. The following scaled LJ energy parameters (first number) and scaled partial atomic charges (second number) are considered:

- 1.0 and 1.0 (corresponding to the original OPLS force field)
- 1.0 and 0.8 (corresponding to the work of Batista et al. [320])
- 0.8 and 1.0
- 0.8 and 0.8

In Fig. 6.4, computed thermodynamic factors and shear viscosities are compared to experimental data. In agreement with what is shown in Fig. 6.2, scaling all partial atomic charges by a factor less than 1 decreases both the thermodynamic factors and shear viscosities. Scaling all LJ interactions by a factor less than 1 decreases the shear viscosities while increasing the thermodynamic factors. Adjusting LJ energy parameters can thus correct for a strong decrease in thermodynamic factors caused by scaling down partial atomic charges (as in Fig. 6.2). Of these four combinations, the best combination is for the scaling factors of 0.8 and 1.0 for the LJ energy parameters and partial atomic charges, respectively. By interpolating between the computed thermodynamic factors and shear viscosities, corresponding to the four combinations of scaling factors, the optimum combination is a scaling factor of 0.8 for the LJ energy parameters and 0.95 for the partial atomic charges. Hereafter, the OPLS force field with this combination of scaling factors will be referred to as the refined OPLS force field. The parameters of this refined OPLS force field can be found in the Supporting Information of the work of Jamali *et al.* [308].

To verify that the refined OPLS force field outperforms the original OPLS force field, several thermodynamic and transport properties of the water-sucrose mixtures are computed at 298 K and 1 atm. In Fig. 6.5, computed (a) liquid densities, (b) thermodynamic factors, (c) shear viscosities, (d) self-diffusivities of sucrose and (e) water, and (f) Fick diffusion coefficients are compared to experimental data for a wide range of concentrations. As compared to the original OPLS force field, thermodynamic properties (i.e., liquid densities and thermodynamic factors) computed using the refined OPLS force field show a considerably better agreement with experiments. In Fig. 6.5a, excellent agreement between computed liquid densities and experimental data is observed. Since the size (σ) parameters of the LJ potentials are unaltered, the differences between liquid densities computed using the original and refined OPLS force fields are small. These differences reach the maximum value of 1%, at a sucrose mass fraction of 60%. Since the original OPLS force field overestimates solute-solute interactions at high concentrations of sucrose, the sucrose molecules tend to aggregate and form more packed liquid structures. This increases the density of the liquid, leading to overestimation of computed densities. Due to this overestimation of solute-solute interactions by the original OPLS force field, the thermodynamic

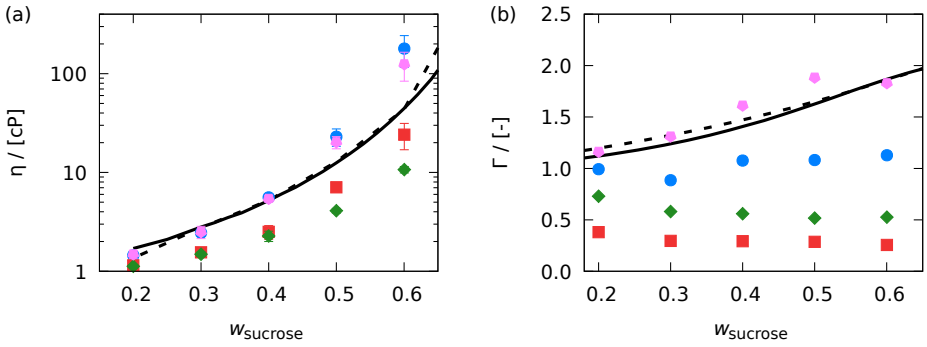

Figure 6.4: Computed (a) shear viscosities and (b) thermodynamic factors for water-sucrose mixtures as a function of the mass fraction of sucrose. All LJ energy (ϵ) parameters and partial atomic charges (q) of the OPLS force field [82] are scaled by respectively: 0.8 and 0.8 (green diamonds), 0.8 and 1.0 (purple pentagons), 1.0 and 0.8 (red squares), and 1.0 and 1.0 (blue circles). The SPC/Fw water model was used [332]. Lines represent (a) experimental shear viscosities (solid [333], dashed [334]) and (b) thermodynamic factors (solid [335], dashed [336]). Error bars indicate 95% confidence intervals. No error bars are reported for thermodynamic factors.

factors are underestimated (see Fig. 6.5b). The good agreement between computed thermodynamic factors and experimental data confirms an accurate description of the solute-solute and solute-water interactions by the refined OPLS force field.

As shown in Fig. 6.5c-f, transport properties computed using the refined OPLS force field are in excellent agreement with experimental data. At low sucrose concentrations, both the original and refined OPLS force fields yield similar values for the transport properties. Deviations become significant as the concentration of sucrose increases. In agreement with the work of Batista et al. [320], the shear viscosities (Fig. 6.5c) computed based on the original OPLS force field are overestimated by up to 300% at a sucrose mass fraction of 0.6. For the refined OPLS force field, this deviation reaches a maximum of 30%. Fig. 6.5d shows that the refined force field provides better estimates for the self-diffusion coefficients of sucrose at high sucrose mass fractions. This is due to less self-association, leading to higher mobility of sucrose molecules. In Fig. 6.5e, no significant differences between self-diffusion coefficients of water computed using the original and refined OPLS force fields are observed. Both force fields were combined with the SPC/Fw water model, which mainly determines the self-diffusivity of water. As the concentration of sucrose increases, the sucrose-water interactions gradually become more important in determining the properties of the medium in which water molecules diffuse. This leads to the small differences observed

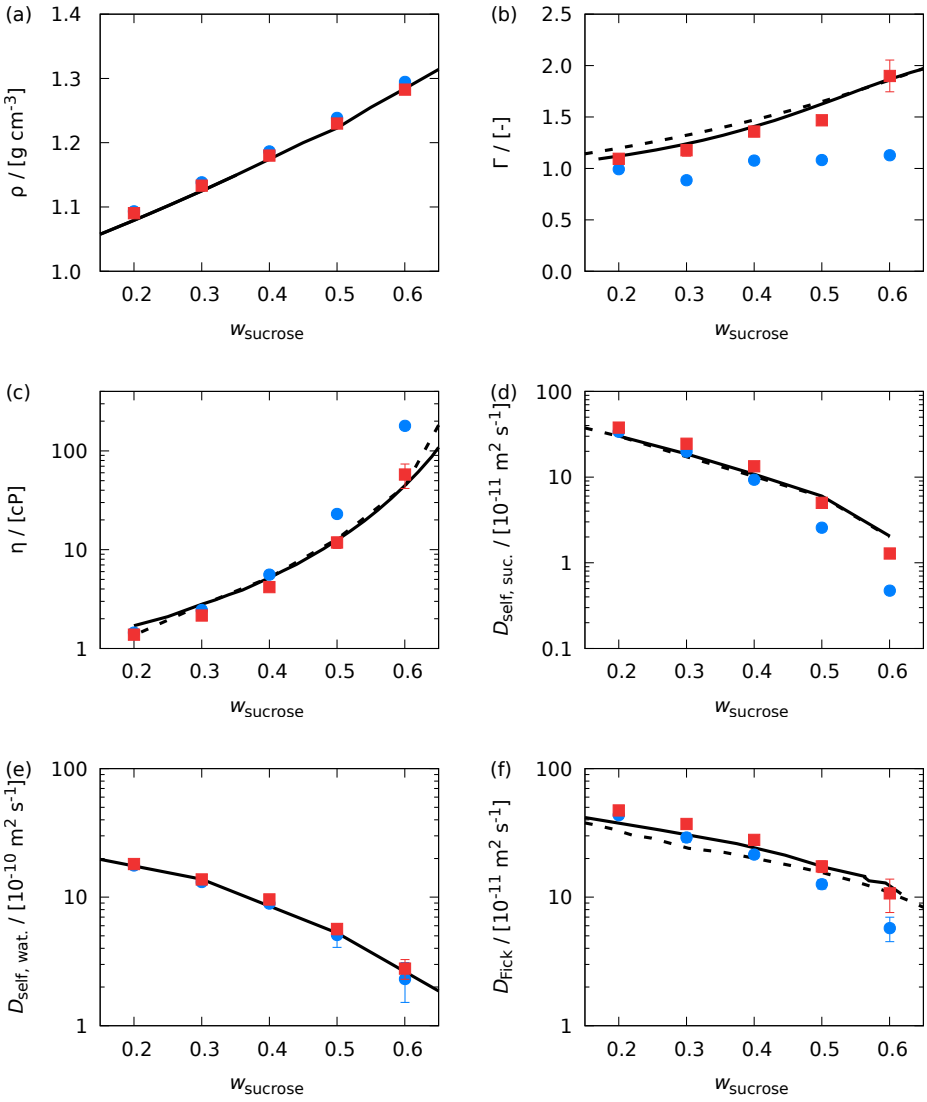

Figure 6.5: Computed (a) densities, (b) thermodynamic factors, (c) shear viscosities, (d) self-diffusivities of sucrose, (e) self-diffusivities of water, and (f) Fick (mutual) diffusion coefficients for water-sucrose mixtures as a function of the mass fraction of sucrose. Temperature and pressure are 298 K and 1 atm, respectively. The results of the original OPLS force field [82] are shown by blue circles. The results of refined OPLS force field (scaled LJ energy parameters and partial atomic charges of all atoms of sucrose by factors of 0.8 and 0.95, respectively) are shown by red squares. Lines represent experimental data for (a) densities (solid [344], dashed [345]) (b) thermodynamic factors (solid [335], dashed [336]) (c) shear viscosities (solid [333], dashed [334]), (d) self-diffusivities of sucrose (solid [334], dashed [346]), (e) self-diffusivities of water (solid [334]), and (f) Fick diffusion coefficients (solid [347], dashed [348]). Error bars indicate 95% confidence intervals.

between computed self-diffusivities at high sucrose mass fractions. In Fig. 6.5f, Fick diffusion coefficients are compared with experiments. Similar to what is observed for the shear viscosity, Fick diffusivities computed using the refined OPLS force field are significantly closer to experimental values than those computed based on the original OPLS force field.

To verify whether the optimum scaling factors for LJ energy parameters (0.8) and partial atomic charges (0.95) are transferable to other carbohydrates, MD simulations were performed for aqueous solutions of the monosaccharide D-glucose at 298 K and 1 atm. Since mixtures of glucose with mass fractions above 51% produce α-D-glucose monohydrate, the following mass fractions of water-glucose mixtures are considered: 20%, 30%, 40%, and 50%. D-glucose forms two anomers in an aqueous solution [2]. Simulation input files are constructed for a ratio 1:2 of α-D-glucose to β-D-glucose [321, 327, 349, 350]. Lay et al. [321] observed that the exact value of this ratio does not affect the outcome of MD simulations.

In Fig. 6.6, computed thermodynamic and transport properties of water-glucose mixtures are compared with experiments. The order of the subfigures is the same as in Fig. 6.5. The results shown in Fig. 6.6a and b clearly show that, compared to the original OPLS force field, the refined OPLS force field leads to a significantly better description of thermodynamic properties. Computed thermodynamic factors are larger than 1 and close to experimental values; the unphysical self-association of glucose molecules at elevated concentrations is thus resolved by using the refined OPLS force field. Fig. 6.6c-f show the transport properties for glucose-water mixtures (i.e., the shear viscosity, self-diffusivity of sucrose and water, and Fick diffusion coefficient). A good agreement between experimental data and computed transport properties is observed. At low mass fractions of glucose ($w_{\text{glucose}} \leq 0.4$), the original OPLS force field shows slightly better agreement with experimental data. However, it is important to note that, for these diluted solutions, the difference between the results obtained based on these two force fields is at most 40% (for self-diffusivity of glucose at a mass fraction of 40%). This is mainly due to the low concentration of glucose, which decreases the effect of the carbohydrate force field on mixture properties. As the mass fraction of glucose rises above 40%, the refined OPLS force field provides better estimates for transport properties. At these concentrations, the results computed based on the original OPLS force field deviate significantly from experiments [320].

By increasing the temperature of the water-glucose mixture, the solubility of glucose in water increases, and mixtures with higher mass fractions of glucose can be realized. For these concentrated solutions, the refined OPLS force field is expected to lead to significant improvements over the original OPLS force field.

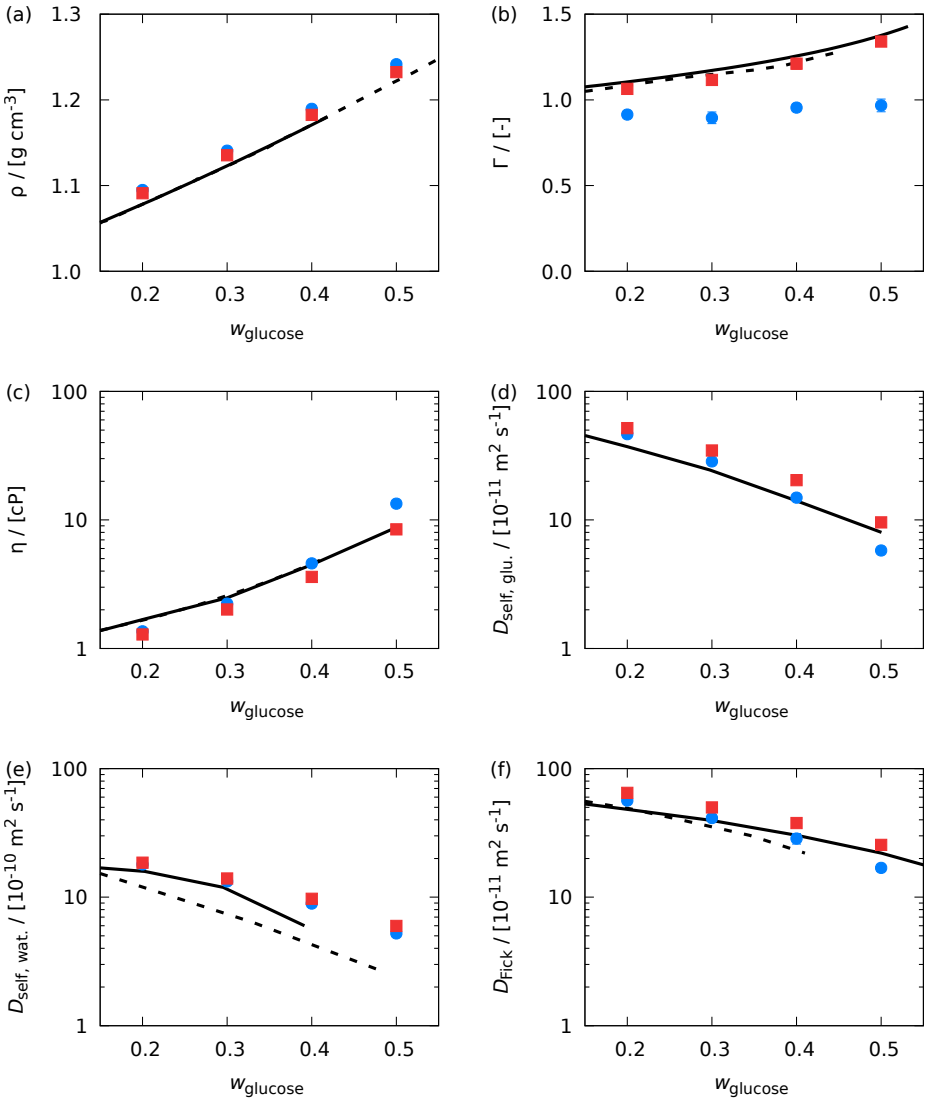

Figure 6.6: Computed (a) densities, (b) thermodynamic factors, (c) shear viscosities, and (d) self-diffusivities of glucose, (e) self-diffusivities of water, and (f) Fick (mutual) diffusion coefficients for water-glucose mixtures as a function of the mass fraction of glucose. Temperature and pressure are 298 K and 1 atm, respectively. The results of the original OPLS force field [82] are shown by blue circles. The results of the refined OPLS force field (scaled LJ energy parameters and partial atomic charges of all atoms of glucose by factors of 0.8 and 0.95, respectively) are shown by red squares. Solid lines represent represent experimental data for (a) densities (solid [351], dashed [352]), (b) thermodynamic factors (solid [353], dashed [354]), (c) shear viscosities (solid [355], dahsed [351]), (d) self-diffusivities of glucose (solid [352]), (e) self-diffusivities of water (solid [352], dashed [356]), and (f) Fick diffusion coefficients (solid [357], dahsed [358]). Error bars indicate 95% confidence intervals.

To verify this, the shear viscosity of an aqueous solution of glucose with a mass fraction of 60% was computed at 313.15 K and 1 atm. The shear viscosity computed based on the original and refined OPLS force fields is 32±4 cP and 15.0±1.5 cP, respectively. Compared to an experimental value of 13.08 cP for this mixture [355], the original OPLS force field leads to a considerable overestimation of the shear viscosity (of about 150%). The refined OPLS force field significantly improves the description at such a high glucose mass fraction.

6.4. CONCLUSIONS

For aqueous solutions of carbohydrates, most force fields predict self-aggregation of solute molecules due to the overestimation of solute-solute interactions. This overestimation results in large deviations of computed properties from experimental data, especially for concentrated solutions, which are relevant to food and biotechnological industries. To decrease the tendency of solute molecules to self aggregate, scaling the Lennard-Jones energy parameters (ϵ) and partial atomic charges (q) of the OPLS force field was proposed. In this way, accurate estimates were obtained for thermodynamic and transport properties of aqueous solutions of sucrose with mass fractions in the range 20%-60%. For this optimization, the three-site SPC/Fw water model was used. No modification in the bonded and non-bonded interaction parameters of the water model were applied. The optimum scaling factors for the Lennard-Jones energy parameters and partial atomic charges were obtained by reproducing experimental thermodynamic factors and shear viscosities of aqueous sucrose solutions. These factors are 0.8 and 0.95, respectively. For both the original and refined OPLS force fields, MD simulations were performed to calculate thermodynamic properties (i.e., liquid densities and thermodynamic factors) and transport properties (i.e., shear viscosities, self-diffusivities of water and sucrose, and Fick diffusion coefficients). Excellent agreement is observed between the properties computed based on the refined OPLS force field and experiments, for a wide range of sucrose concentrations. The transferability of the optimum scaling factors was verified by performing MD simulations of aqueous solutions of D-glucose. The computed thermodynamic and transport properties agree well with available experimental data, especially at high concentrations of glucose. This suggests that the scaling factors are transferable to other carbohydrates. By using the refined OPLS force field, accurate estimates for thermodynamic and transport properties can be obtained. While the proposed method for optimizing the non-bonded interactions of a force field was verified for the OPLS force field, this method may also be used for other force fields combined with other water models.

7

Optimizing Intramolecular Interactions of Crown-ethers

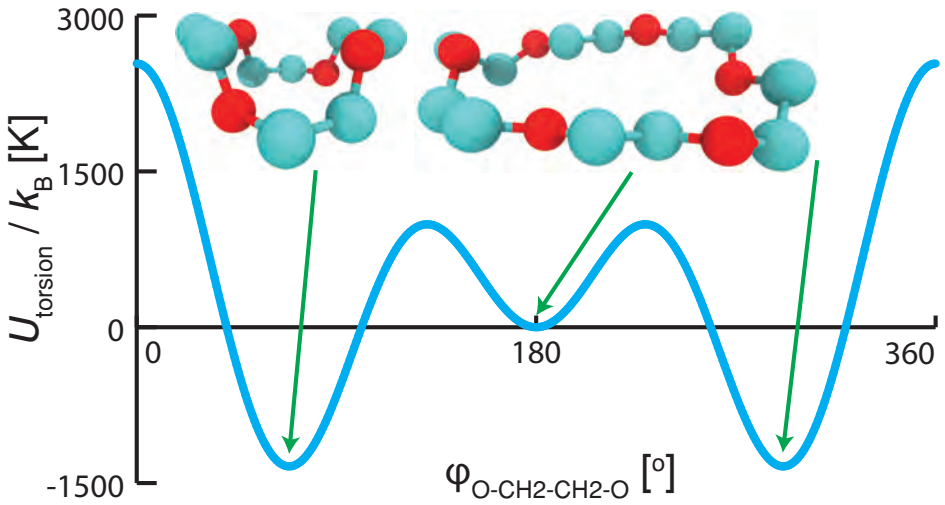

This chapter is based on the paper: S.H. Jamali, M. Ramdin, T.M. Becker, S.K. Rinwa, W. Buijs, and T.J.H. Vlugt, *Thermodynamic and Transport Properties of Crown-ethers: Force Field Development and Molecular Simulations.* Journal of Physical Chemistry B, **121**, 8367-8376 (2017) [214].

7.1. INTRODUCTION

Crown-ethers are macrocyclic polyethers discovered by Pedersen in the late 1960s [359]. Due to their strong ability to complex with cations and to solvate salts in aprotic solvents, crown-ethers have been used in phase-transfer catalysis, sensors, solvent extraction, analytical chemistry, biochemistry, and electrochemistry [359–364]. Recently, crown-ethers have been used to synthesize the first generation of porous liquids (PLs), which are liquids with permanent pores, a unique property not exhibited by conventional solvents [365–369]. Porous liquids can be created by mixing organic cage molecules with bulky solvents such as crown-ethers, which cannot enter the pores of the cage molecules, thereby the porosity of the cages in the mixture is maintained [365]. The pores can accommodate small guest molecules, which renders PLs interesting candidates for gas separation and storage [365, 370–374]. The performance of PLs in gas separation is strongly dependent on the transport and thermodynamic properties of the crown-ether solvent. In the past, some molecular simulation studies investigated the specific application of cation complexation with crown-ethers in (organic) solvents [375–383]. However, the feasibility of using crown-ethers as gas absorption solvents has not been experimentally or computationally explored so far.

In this chapter, molecular simulation is used to investigate the potential of crown-ethers for gas separation purposes. A schematic representation of the studied crown-ether molecules is shown in Fig. 7.1. The ligand cavity radii of 12-crown-4, 15-crown-5, and 18-crown-6 are 0.6 Å, 0.85 Å, and 1.3 Å, respectively [362]. Hence, crown-ethers can complex cations of similar size selectively, e.g., 12-crown-4 has a high affinity for Li^+, which has an ionic radius of 0.74 Å [362]. The affinity of crown-ethers is interesting to be studied for separating (neutral) gas molecules. To design a separation process, data on transport properties and gas solubilities are required. Molecular Dynamics (MD) simulations are used to compute densities, viscosities, and self-diffusion coefficients of 12-crown-4, 15-crown-5, and 18-crown-6 ethers, while Monte Carlo (MC) simulations are used to compute the solubility of CO_2, CH_4, and N_2 in 12-crown-4 and 15-crown-5.

Computed properties in molecular simulations are strongly dependent on the used force field. As mentioned earlier, many studies have studied the complexation of crown-ethers using MD simulations. Most of these studies [375, 377–379, 381–385] employed the AMBER [86] force field or its derivatives. Here, the Transferable Potentials for Phase Equilibria (TraPPE) force field is used [75]. Contrary to the all-atom AMBER force field, the united-atom TraPPE force field lumps hydrogen atoms in with the bonded carbon atoms. This means that the AMBER force field are computationally expensive for considering more interaction sites. Moreover, the parameters of the TraPPE force field are transferable

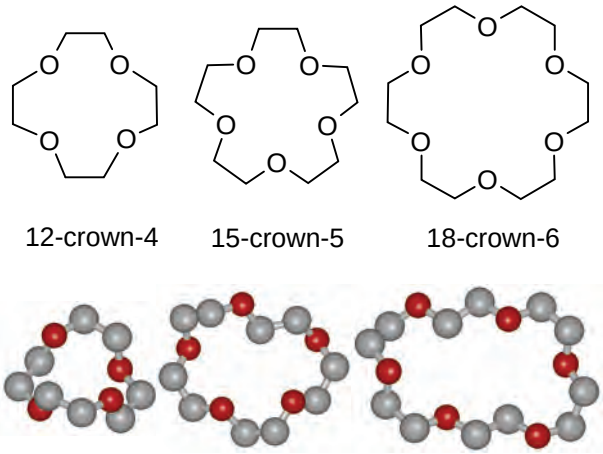

Figure 7.1: Schematic (top) and united-atom (bottom) representation of 12-crown-4, 15-crown-5, and 18-crown-6. CH_2 groups and oxygen atoms are illustrated in gray and red, respectively. The atomistic representation was created using iRASPA [329].

to other hydrocarbons and these parameters are compatible with natural gas or syngas components such as CO_2 [136] and H_2S [386]. The transferability of force field parameters as well as compatibility with the force field of molecules present in the gas treatment processes are the main merits of choosing this force field. However, the TraPPE force field was developed for linear ether molecules [78] and may not be extended to cyclic ether molecules such as 12-crown-4. Although 12-crown-4 forms a liquid at ambient temperatures, MD simulations based on the TraPPE force field predict a crystalline structure with all molecules fluctuating around their equilibrium positions. This can be seen in the snapshot and mean-squared displacement (MSD) plot of these molecules shown in Fig. 7.2. Therefore, the force field parameters for cyclic ether molecules are required to be adjusted here by using the Density Functional Theory (DFT) prior to be used in molecular simulation. All computed properties are compared with limited experimental data and overall a good agreement is found.

This chapter is organized as follows. In Section 7.2, a refined TraPPE force field is developed for cyclic ether molecules based on DFT quantum calculations. In Section 7.3, the details of MD and MC simulations are provided. The results of these simulations for computing thermodynamic and transport properties are discussed in Section 7.4. The findings and main conclusions are summarized in Section 7.5.

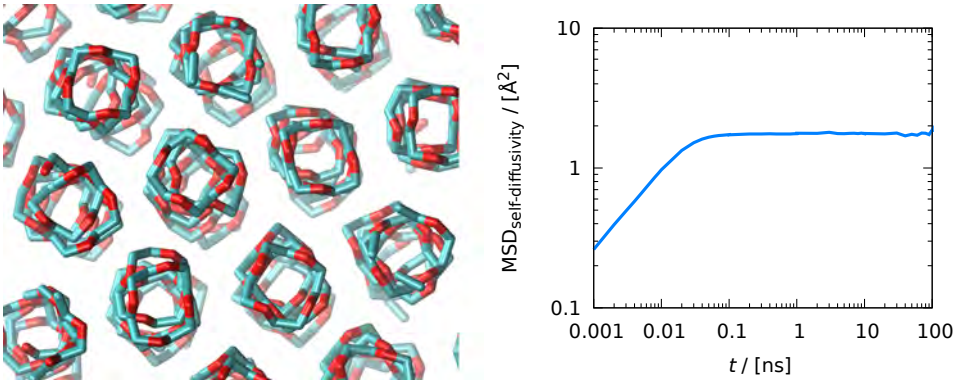

Figure 7.2: The crystalline structure of 12-crown-4 (left) and its mean-square displacement (right) at 363 K and 1 atm obtained from an MD simulation using original TraPPE force field. CH_2 groups and oxygen atoms are illustrated in cyan and red, respectively.

7.2. FORCE FIELD DEVELOPMENT

The united-atom (UA) TraPPE force field [78] for ethers seems to be a good starting point for the force field-based molecular simulations of crown-ethers. The force field parameters of ether groups were originally developed for linear molecules [78]. These parameters may not be transferable to cyclic molecules. This issue was also addressed by Keasler et al. [81] who fitted the TraPPE force field parameters of five or six-membered cyclic molecules. A similar approach can be adopted to define new force field parameters for crown-ethers, or generally for any ether group in cyclic molecules. The bond stretching and bond-angle bending potentials are considered to be identical to the TraPPE-UA force field as they do not vary significantly even for small five or six-membered cyclic molecules [81]. The non-bonded potential parameters of cyclic and linear molecules may slightly vary due to the different polarization of atoms in these two types of molecules. However, it is expected that this effect should become less significant as the diameter of the ring increases and the atoms in the ring are further located from each other [81]. Therefore, the original Lennard-Jones parameters and partial atomic charges provided by the TraPPE-UA force field will remain identical [78]. The only force field component requiring adjustment is the intramolecular torsional potential, specified by the alteration of the dihedral angle. A similar approach to the work of Keasler et al. [81] is used to obtain the force field parameters of the torsional potential. By scanning a wide range of variation for the torsion types present in a single molecule, the energy profile computed from the DFT calculations is fitted to a functional form for each torsion type. The TraPPE functional form of torsional potential for a dihedral angle

ϕ consists of a cosine series with four force constants (c_0, c_1, c_2, and c_3) [78]:

$$U_{\text{torsion}}(\phi) = c_0 + c_1\left[1+\cos(\phi)\right] + c_2\left[1-\cos(2\phi)\right] + c_3\left[1+\cos(3\phi)\right] \tag{7.1}$$

The torsional potential is fitted so that the total force field-based energy, including the bonded and non-bonded interactions, reproduces the DFT energy. Initially, the most stable conformer of a molecule is identified according to DFT calculations. This configuration has the minimum energy level out of all possible conformations of that molecule or, in other words, the highest Boltzmann probability. Constraining one of the dihedral angles in the molecule to a constant value and then relaxing the structure leads to a new shape and a new energy level based on DFT calculations. By modifying the dihedral angle for a range of values, different energy levels of the molecule can be scanned. The energy differences from the ground-state energy level are then computed from the DFT (ΔU_{DFT}) and molecular mechanics (ΔU_{ff}). DFT calculations are carried out at the B3LYP/6-31G* level in Spartan'14 [387]. The term ΔU_{ff} consists of all bonded and non-bonded energies that have been specified by the TraPPE force field except for the torsional potential. In this process, the relative energy of N_{conf} distinct configurations of the molecule is scanned. The force constants specified in Eq. (7.1) are then obtained by minimizing the absolute difference between the DFT and molecular mechanics energies ($\Delta\Delta U_i$) using the following objective function (O.F.):

$$\text{O.F.} = \frac{1}{N_{\text{conf}}}\sum_{i=1}^{N_{\text{conf}}} |\Delta\Delta U_i| \tag{7.2}$$

Crown-ethers have two torsion types: CH_2-CH_2-O-CH_2 and O-CH_2-CH_2-O (represented here as C-C-O-C and O-C-C-O), each of which requires four torsional potential parameters according to Eq. (7.1). Due to the ring structure of crown-ethers, modifying a dihedral angle also alters other degrees of freedom of the molecule, namely bond stretching, bond-angle bending, and dihedral-angle torsion. Therefore, all force field parameters should be fitted simultaneously. In total, 63 and 104 different configurations of 12-crown-4 and 18-crown-6 molecules are considered for this force field parameterization, respectively. The objective function (Eq. (7.2)) is minimized via the interior point method (the fmincon function) implemented in the MATLAB Optimization Toolbox [388]. For this dataset, the final value of the objective function is 110 K/k_{B} (0.92 kJ/mol). The fitted force constants are provided in Table 7.1 and the shape of the two torsion types over different dihedral angles is illustrated in Fig. 7.2.

The need for refitting force field parameters of the original TraPPE (linear ether TraPPE) force field became apparent when the TraPPE force field for linear ethers (linear ether TraPPE force field) could not reproduce the liquid form

Table 7.1: Dihedral parameters of the linear ether TraPPE force field and the refitted torsional potentials (see Eq. (7.1) for the functional form). All force constants (c_i) are in c_i/k_B / K.

Dihedral	Force field	c_0	c_1	c_2	c_3
C-C-O-C	TraPPE [78]	0.00	725.35	-163.75	558.20
	Refined TraPPE	136.4	1523.2	-613.4	473.0
O-C-C-O	TraPPE [78]	503.24	0.00	-251.62	1006.47
	Refined TraPPE	0.0	163.0	-964.7	1106.1

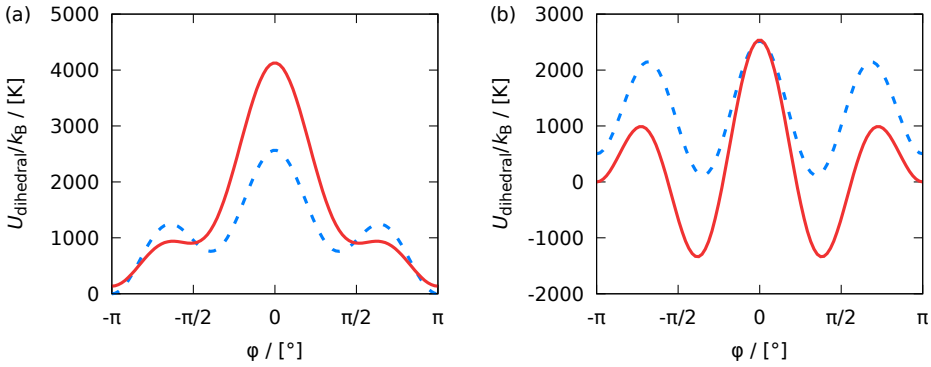

Figure 7.3: Newly fitted torsional potentials (solid red lines) to Table 7.1 for (a) C-C-O-C and (b) O-C-C-O dihedral angles, compared to the torsional potentials of the linear ether TraPPE force field (dashed blue lines) [78].

of 12-crown-4 at room or elevated temperatures (see Fig. 7.2). In order to reparameterize the torsional potentials of the force field, a set of configurations of 12-crown-4 was considered. Despite the better performance of this fitted torsional potential for 12-crown-4, the computed transport properties of 18-crown-6 deviated significantly by one order of magnitude from the experiments (not reported here). The reason can be found in the difference between the shape of 12-crown-4 and 18-crown-6 molecules (Fig. 7.1). 12-crown-4 is a small cyclic molecule, so it has only gauche orientations for its O-C-C-O dihedral angles. The gauche orientation is visible in its prevalent conformer (with a Boltzmann probability of 90% at 298 K) whose dihedral angles are equal to either -72° or +72° at the B3LYP/6-31G* DFT level. As the size of crown increases, the cyclic molecule can have at least one trans O-C-C-O dihedral angle, which is not present in smaller crowns. Therefore, the force constants fitted to the 12-crown-4 energy profile does not contain any information on the energy of the O-C-C-O dihedral angles

in the vicinity of $\phi = \pi$, which is present in the main conformer of 18-crown-6. The final force constants (Table 7.1) are obtained by fitting to the energy profiles of both 12-crown-4 and 18-crown-6.

To examine how accurately the new (refined TraPPE) force field can reproduce the torsional potential of DFT calculations, the torsional energies of the first ten conformers of the three crown-ethers were compared between the DFT and molecular mechanics. The cumulative Boltzmann probability of these ten conformers at 298 K for each molecule is at least 95%, encompassing a large portion of the possible crown-ether configurations. Initially, these conformers were relaxed using DFT calculations at the B3LYP/6-31G* level. The torsional energy of each dihedral angle ($U_{\text{dihedral,DFT}}$) is computed from Eq. (7.1) with the newly fitted parameters in Table 7.1. Each configuration was then relaxed using molecular mechanics based on the new force field. Similarly, the torsional energies of the relaxed configuration are also calculated from Eq. (7.1). Fig. 7.3 shows the comparison of these thirty conformers and their corresponding 150 O-C-C-O and 300 C-C-O-C torsional energy data points. Most of the dihedral angles and consequently their energy levels show small deviations. About 93% of the 450 dihedral angles shows a maximum deviation in the torsional energy of 250 K/k_B (0.5 kcal/mol) from DFT calculations. It is worth mentioning that the current force field parameters were obtained by varying the dihedral angles of only one conformer of 12-crown-4 and one conformer of 18-crown-6. However, the fitted parameters may in general be used for all crown-ethers. In the next stage, the accuracy of the force field parameters has to be verified by computing thermodynamic/transport properties of crown-ethers and compare them with experimental data.

7.3. SIMULATION DETAILS

Force field-based Molecular Dynamics (MD) and Monte Carlo (MC) simulations are two powerful methods to study the thermodynamic and transport properties of materials. RASPA [389, 390] and LAMMPS [126] are used for the MC and MD simulations, respectively. The force field parameters of crown-ethers [78], CH_4 [75], CO_2 [136, 391], and N_2 [136] define the intramolecular and intermolecular interaction potentials. The Lennard-Jones (LJ) potentials are truncated at 12 Å and analytic tail corrections are applied for the computation of energy and pressure. The Lorentz-Berthelot combining rules are applied for dissimilar interaction sites [36]. The long-range electrostatic interactions are included by means of the Ewald summation with a relative precision of 10^{-5} [35].

Equilibrium MD (EMD) simulations were carried to calculate the transport properties of crown-ethers with the help of the OCTP plugin [210] for LAMMPS [126]. Initial configurations were made in PACKMOL [286] and VMD [200] was

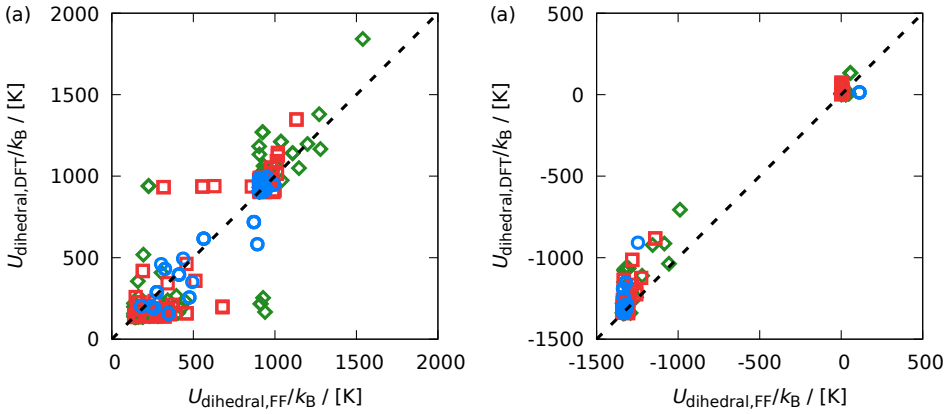

Figure 7.4: Comparison between torsional potentials computed for (a) C-C-O-C and (b) O-C-C-O dihedral angles of the first 10 conformers of 12-crown-4 (blue circles), 15-crown-5 (red squares), and 18-crown-6 (green diamonds), optimized using the DFT calculations and the newly fitted torsional potential.

used to create simulation input files for LAMMPS. The number of 12-crown-4, 15-crown-5, and 18-crown-6 molecules in a simulation box is 100, 80, and 80, respectively. The equations of motion are integrated by the velocity-Verlet algorithm with a timestep size of 1 fs [35]. The time correlations are sampled in the NVE ensemble with a total simulation length of 400 ns. The finite-size effects of self-diffusion coefficients are considered via the analytic correction proposed by Yeh and Hummer (Eq. (4.1)) [118].

Thermodynamic properties such as solubilities of gases in solvents are calculated using MC simulations. Computing the solubility of gases in non-volatile solvents requires an open ensemble in which a reservoir comes into contact with the simulation box containing the solvent. This is the osmotic ensemble in which the absorption isotherms of the gases in the low-volatile crown-ethers are computed [392]. In this ensemble, the temperature, pressure, the number of solvent molecules in the liquid, and the fugacity of the solute are kept fixed [392, 393]. The solubility of natural gas, synthesis gas, or acidic gas components in commercial solvents as well as ionic liquids have been studied in the literature [394–398]. The results of these studies were verified on the basis of the available experimental data. Good agreement between the experiments and simulations indicates the capability of MC simulations in predicting gas solubility data.

Four types of MC trial moves are used: translations, rotations, insertions/deletions of gas molecules, and volume changes. The probability of selecting the first two trial moves is 40% and the insertions/deletions trial move is 20%. The volume change trial move is chosen randomly every 1000 trial moves. Crown-ethers are cyclic molecules; it is therefore not possible in RASPA to use Configurational-Bias Monte Carlo (CBMC) trial moves to generate different configurations of the molecule. This means that all crown-ether molecules are considered to be rigid in MC simulations. The rigid configuration is obtained from the conformer with the highest Boltzmann probability based on the conducted DFT calculations. While this approach may work for small molecules, the importance of using flexible molecules becomes more pronounced as the size of the molecule increases. Therefore, the solubility of gases in 12-crown-4 and 15-crown-5 ethers are exclusively studied here. Each MC simulation consists of half a million equilibration MC cycles, followed by one million production MC cycles. It is one MC cycle that is equal to the number of particles in the system. The gas solubility at a given temperature and pressure is computed from 4 and 8 independent simulations of 12-crown-4 and 15-crown-5, respectively.

7.4. RESULTS AND DISCUSSIONS

The refined TraPPE force field is applied to calculate the thermodynamic and transport properties of three crown-ethers, that are 12-crown-4, 15-crown-5, and 18-crown-6. In this section, the properties of the pure crown-ethers as well as the vapor-liquid equilibrium (VLE) results of three natural gas components in 12-crown-4 and 15-crown-5 are reported.

7.4.1. PROPERTIES OF PURE CROWN-ETHERS

Fig. 7.5 shows the densities of the crown-ethers, computed for both the linear ether TraPPE and the refined TraPPE force fields and a comparison with the experimental densities. The refined TraPPE force field (closed symbols) provides an accurate estimate of the densities with less than 1% deviation from the experiments, for a wide range of temperatures. In comparison, the linear ether TraPPE force field estimates the experimental densities of 15-crown-5 and 18-crown-6 with deviations of 3%. Furthermore, the linear ether TraPPE force field substantially overpredicts the density of 12-crown-4 (approximately 1200 kg/m^3) as a crystalline structure with no Brownian motion of the 12-crown-4 molecules is observed. This explains that such a high density corresponds to a solid state rather than a liquid state at room/elevated temperatures. This considerable discrepancy between the simulations and the experiments was the main rationale behind the development of the refined TraPPE force field for cyclic ether molecules.

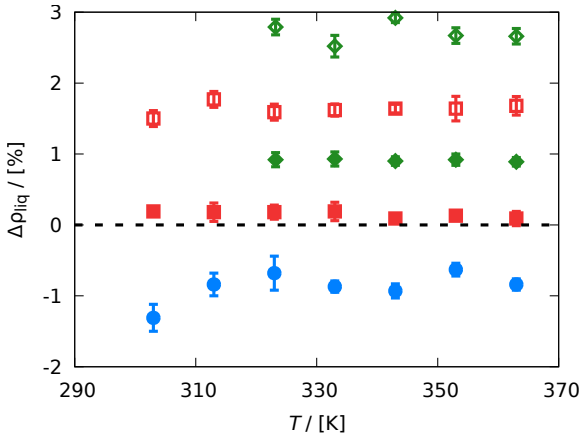

Figure 7.5: Relative error in calculated densities of 12-crown-4 (blue), 15-crown-5 (red), and 18-crown-6 (green) at different temperatures based on the linear ether TraPPE (open symbols) and the refined TraPPE (closed symbols) force fields.

In Fig. 7.6, computed self-diffusivities and shear viscosities of the crown-ethers at several temperatures are compared with experiments. As explained earlier, the original TraPPE force field for linear ether molecules predicts a solid state for 12-crown-4 at room or elevated temperatures. The agreement between the experiments and the simulation results for 15-crown-5 and 18-crown-6 is also rather weak. However, the results of the refined TraPPE force field correspond closely to the experiments. The maximum deviations in the viscosity of 12-crown-4 and 15-crown-5 are 10% and 20%, respectively. A maximum deviation of 57% in the viscosity of 18-crown-6 is observed at 333 K, and the deviation decreases to 15% as the temperature increases to 363 K. Evidently, the computed transport properties of 18-crown-6 are more sensitive to temperature than the experiments while the simulation results of 12-crown-4 and 15-crown-5 show a similar sensitivity to temperature as the experiments.

It is interesting to compare the viscosity of the crown-ethers with their linear counterparts, namely polyethylene glycol dimethyl ethers (PEGDME). PEGDMEs consist of ether groups like crown-ethers, except that they are linear molecules without any ring in their structure. PEGDMEs are used in industry as solvents for carbon capture and acid gas removal processes under the trade name of Selexol [399]. The viscosity of PEGDME is 3.18 cP at 333 K [400]. At the same temperature, the viscosities of 12-crown-4, 15-crown-5, and 18-crown-6 are 3.47, 6.40, and 8.94 cP, respectively [401]. At the same conditions, PEGDME has a comparable viscosity with 12-crown-4 and a lower viscosity than the other crown-ethers.

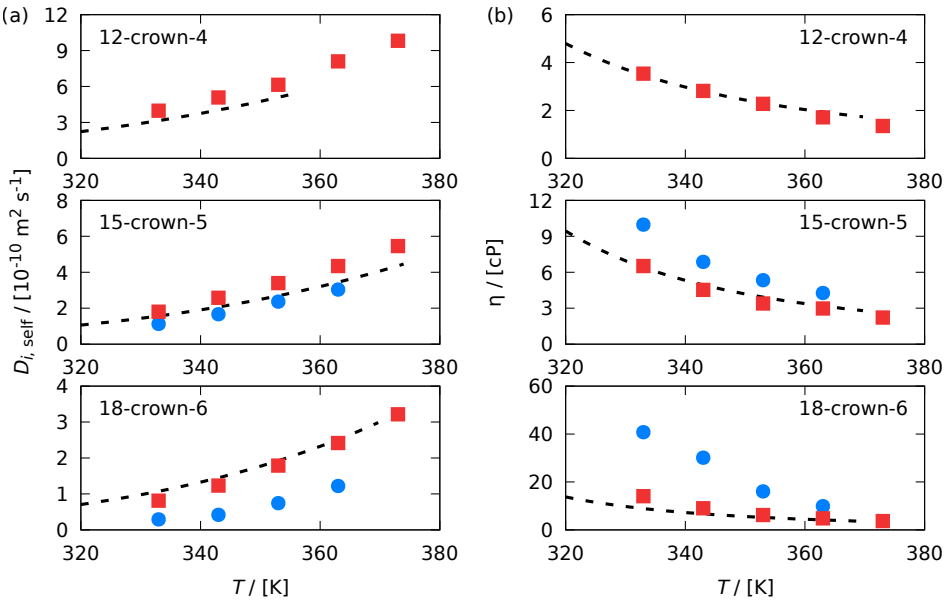

Figure 7.6: (a) Self-diffusivity and (b) shear viscosity (right) of the 12-crown-4, 15-crown-5, and 18-crown-6 as functions of temperature based on the linear ether TraPPE (blue circles) and the refined TraPPE (red squares) force fields. Dashed lines represent experimental data. The linear ether TraPPE force field predicts a solid system for 12-crown-4 for the shown temperatures.

7.4.2. SOLUBILITY OF NATURAL GAS COMPONENTS

The refined TraPPE force field developed in this chapter shows high accuracy in predicting the density and transport properties of pure crown-ethers. As this force field is based on the TraPPE force field and the only alteration is the parameters of the torsional potentials, it can be deduced that torsional potentials are important to correctly reproduce the structure and dynamics of the crown-ether molecules in the liquid phase.

MC simulations in the osmotic ensemble are employed to study the solubility of the main natural gas components, that are CH_4, CO_2, and N_2, in the crown-ethers. 100 molecules of 12-crown-4 or 80 molecules of 15-crown-5 were inserted initially in the simulation box, which is held in contact with the gas reservoir. As explained earlier, crown-ethers are considered non-volatile, and the number of crown-ether molecules remains constant. MC simulations were carried out for these three gases in 12-crown-4 and 15-crown-5 at four temperatures. Fig. 7.7 shows the absorption isotherms of the three gases at 333 K. It can be seen that

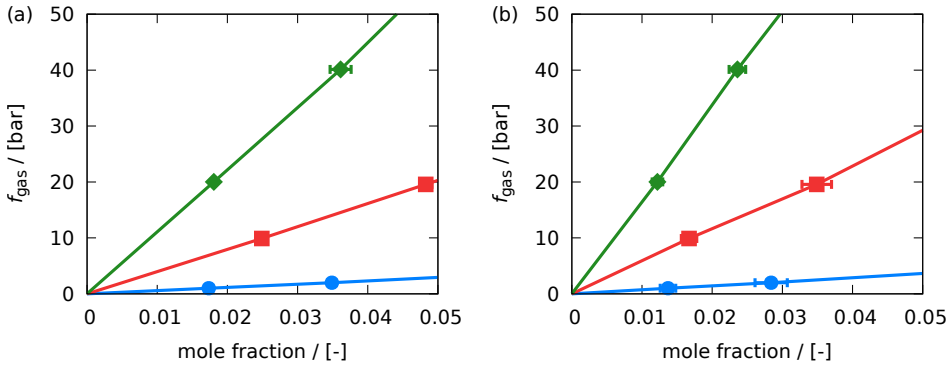

Figure 7.7: Solubility of CO_2 (blue circles/lines), CH_4 (red squares/lines), and N_2 (green diamonds/lines) in (a) 12-crown-4 and (b) 15-crown-5 at 333 K. Lines are a guide to the eyes.

CO_2 has the highest solubility for both 12-crown-4 and 15-crown-5 followed by CH_4 and N_2. Due to the large solubility difference, the separation of CO_2 from CH_4 and N_2 using crown-ethers is feasible.

The resultant solubility data are used to compute the Henry coefficients of the gases in the crown-ethers. The Henry coefficient for the absorption of a gas in a dilute mixture is defined as [402]:

$$H_{12} = \lim_{x \to 0} \frac{f_{\text{gas}}}{x} \tag{7.3}$$

where f_{gas} and x are the fugacity of the gas and the molefraction of the solute in the mixture, respectively. The computed Henry coefficients at different temperatures are provided in Table 7.2 and compared with the available experimental data. The agreement between the experiments and simulation results suggests that the rigid structure of the crown-ethers may have small influence on the solubility results. In addition, the Henry coefficients of the gases in the crown-ethers are compared to those of the linear PEGDMEs in Table 7.2. Both the linear and cyclic molecules have similar Henry coefficients, so a similar CO_2 removal performance as PEGDMEs is expected from the crown-ethers.

The ideal selectivity of two gases, for instance CO_2 and CH_4, in a solvent can be defined as the ratio of their Henry coefficients [402]:

$$S_{CO_2/CH_4} = \frac{H_{CH_4}}{H_{CO_2}} \tag{7.4}$$

Table 7.2: Henry coefficients of CO_2, CH_4, and N_2 in 12-crown-4, 15-crown-5, and PEGDME at different temperatures (T), computed from MC simulations. All Henry coefficients are in bar.

	T / [K]	CO_2	CH_4	N_2
12-crown-4	303	35.9 (33.6 [403])	390	1250 (1430 [403])
	313	43.2	400	1240
	333	58.9	410	1160
	353	76.8	420	1090
15-crown-5	308	45.9 (42.0 [403])	550	1620 (1240 [403])
	313	51.4	550	1690
	333	72.6	590	1670
	353	94.0	590	1770
PEGDME	313	(43 [404], 47 [405], 56.1 [406])	(387 [407])	(1680 [406])

Based on the data of Table 7.2, the ideal CO_2/CH_4 selectivity in 12-crown-4 (303 K), 15-crown-5 (308 K), and PEGDME (313 K) are 11.0, 13.2, and 8.2, respectively. The comparable CO_2/CH_4 selectivity of crown-ethers to PEGDMEs (Selexol) along with their low viscosity show the potential of crown-ethers for CO_2 separation from natural gas.

The Gibbs free energy ($\Delta_{abs}G$), enthalpy ($\Delta_{abs}H$), and entropy ($\Delta_{abs}S$) of absorption can be calculated from the Henry coefficients of the gases as functions of temperature [402]:

$$\Delta_{abs}G = RT\left[\ln\left(H_{12}/\text{bar}\right)\right] \tag{7.5}$$

$$\Delta_{abs}H = -RT^2\left[\frac{\partial \ln\left(H_{12}/\text{bar}\right)}{\partial T}\right] \tag{7.6}$$

$$\Delta_{abs}S = -RT\left[\frac{\partial \ln\left(H_{12}/\text{bar}\right)}{\partial T}\right] - R\ln\left(H_{12}/\text{bar}\right) \tag{7.7}$$

These equations can be analytically solved provided that a functional form for H_{12} is available as a function of temperature. A simple two-parameter equation can be used to specify the temperature dependency of Henry coefficients [402]:

$$\ln\left(H_{12}/[\text{bar}]\right) = a_0 + \frac{a_1}{T} \tag{7.8}$$

Fig. 7.8 shows the computed Henry coefficients and the fitted lines to Eq. (7.8). The Henry coefficients of low soluble gases (CH_4 and N_2) do not strongly depend on the temperature. This weak correlation results in a gradual slope of the lines for CH_4 and N_2, leading to low enthalpies of absorption, as reported in Table 7.3. The observed solubility trend ($CO_2 > CH_4 > H_2$) is consistent

Table 7.3: Thermodynamic parameters fitted to the Henry coefficients of CO_2, CH_4, and N_2 in 12-crown-4 and 15-crown-5, using Eq. (7.8). The Gibbs free energy ($\Delta_{abs}G$), enthalpy ($\Delta_{abs}H$), and entropy ($\Delta_{abs}S$) of absorptions are calculated from Eqs. (7.5) to (7.7).

		a_0 [-]	a_1 [K]	$\Delta_{abs}G$ [kJ/mol]	$\Delta_{abs}H$ [kJ/mol]	$\Delta_{abs}S$ [J/mol·K]
12-crown-4 (303 K)	CO_2	8.94	-1623	9.0	-13.5	-74.4
	CH_4	6.47	-153	15.0	-1.3	-53.8
	N_2	6.14	305	18.0	2.5	-51.0
15-crown-5 (308 K)	CO_2	9.48	-1736	9.4	-14.4	-78.8
	CH_4	6.68	-198	15.9	-1.6	-57.8
	N_2	7.93	-164	18.6	-1.4	-66.0

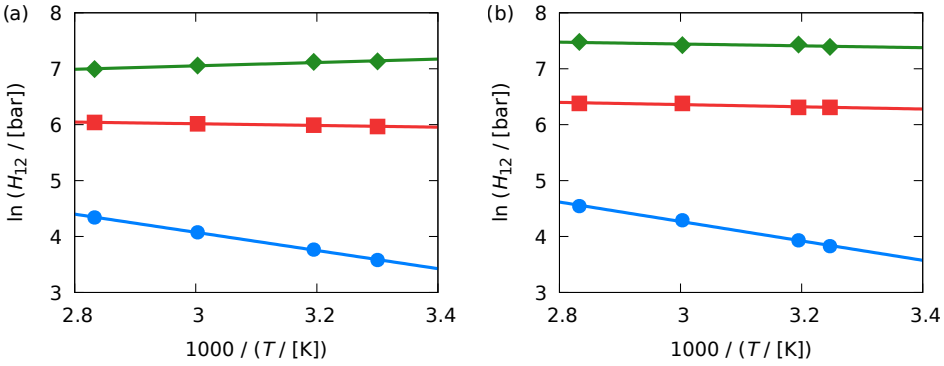

Figure 7.8: Henry coefficients of CO_2 (red squares/lines), CH_4 (blue circles/lines), and N_2 (green diamonds/lines) in 12-crown-4 (closed symbols/solid lines) and 15-crown-5 (open symbols/dashed lines) at different temperatures. The lines are fitted to Eq. (7.8) and the fitted parameters are listed in Table 7.3.

with the enthalpy of absorption of the gases in 12-crown-4 and 15-crown-5. For all the gases, the MC simulations predict a higher solubility in 12-crown-4 than in 15-crown-5. This is remarkable since the solubility of gases generally increases with increasing molecular weight of solvents. Since the enthalpy of absorption of the gases in 12-crown-4 and 15-crown-5 are similar, the difference in the solubilities can be caused by an entropic effect, which is consistent with the $\Delta_{abs}S$ values reported in Table 7.3. Therefore, it seems that the boat-like shape of 12-crown-4 (see Fig. 7.1) may be more favorable to accommodate gas molecules compared to the more flat-shaped 15-crown-5 molecules.

7.5. CONCLUSIONS

Crown-ethers, or cyclic molecules consisting of ether groups, have recently been proposed for gas separation processes as a proper solvent for porous liquids. This chapter investigated the thermodynamic and transport properties of several crown-ethers, which are 12-crown-4, 15-crown-5, and 18-crown-6, using force field-based molecular simulations. Since the TraPPE force field developed for linear ether molecules cannot be employed for cyclic molecules, a new set of torsional potential parameters were computed for crown-ethers from DFT calculations. The transferability of the developed force field should be comparable to the TraPPE force field, which means that the developed force field can be combined with other types of crown-ethers as well as other biomolecules defined by the TraPPE force field. MD simulations were carried out to compute the density, viscosity, and self-diffusion coefficient of the pure crown-ethers. Monte Carlo simulations were used to study the solubility of natural gas components, that are CH_4, N_2, and CO_2, in the crown-ethers. The computed thermodynamic and transport properties correspond closely to the experiments, suggesting the accuracy of the new force field, which is also transferable to other cyclic-ether molecules. Furthermore, the comparable transport properties and the CO_2/CH_4 selectivity of the studied crown-ethers, especially 12-crown-4, with polyethylene glycol dimethyl ethers indicate the potential of the crown-ether in gas treatment processes.

CONCLUSIONS

Force field-based Molecular Dynamics (MD) is a powerful tool to investigate dynamic processes and properties of fluids at a molecular level. This includes thermodynamic, transport, and structural properties of fluids and solids at different conditions. A classical force field is often used to describe interactions between different atoms and molecules. Therefore, the accuracy of the predictions by MD simulations strongly depends on both the force fields and the algorithms used to sample properties.

This thesis is structured into two main parts. In the first part, chapters 2 to 5, the computation of transport properties of fluids is studied using equilibrium (EMD) and non-equilibrium (NEMD) Molecular Dynamics. It is shown that both EMD and NEMD simulations provide important insight into the transport properties of fluids and the underlying processes affecting these properties. NEMD is used to study fluid permeation through a nanoporous medium. Zeolite nanosheet membranes are studied for water desalination applications. Similar to other 2-D hydrophobic nanoporous materials such as carbon nanotubes, the results show a high water permeability and a high salt rejection in zeolite nanosheets. It was observed that the performance of a zeolite nanosheet for water desalination directly correlates with its structural (e.g., pore-limited diameter) and energetic (i.e., free energy barrier) characteristics. These results facilitate future studies, including experimental studies, to investigate the potential of zeolite nanosheets for water desalination applications.

EMD simulations are generally used for the computation of transport properties of bulk fluids. As a part of this research, a new plugin, called OCTP, has been developed for LAMMPS, an MD software package, under the terms of the GNU General Public License v2.0. This plugin can be used in EMD simulations to obtain transport properties of a fluid, i.e., self-diffusivities, Maxwell-Stefan diffusion coefficients, shear viscosities, bulk viscosities, and thermal conductivities. This plugin is used to investigate finite-size effects of diffusion coefficients of liquids, as well as other transport properties close to the critical point. Knowledge on finite-size effects of computed properties is an important subject in the field of MD. Despite the exponential growth of computational power in the past decades, the typical size of simulation boxes is still limited to nanometers. This scale is much smaller than the thermodynamic limit. It was observed that all transport properties show finite-size effects close to the critical point. The correction proposed by Yeh and Hummer (Journal of Physical Chemistry B 108, 15873-15879 (2004)) for self-diffusion coefficients of liquids can accurately correct the finite-size effects. This correction holds for all pure and multicomponent liquids regardless of the difference in the size of constituent molecules. Based on this, a correction is developed for finite-size effects of Maxwell-Stefan mutual diffusion coefficients of binary liquid mixtures. For multicomponent mixtures,

a system-size dependence has been observed. However, an analytic correction could not (yet) be obtained due to the complexity of the governing equations. This could be the focus of the future investigation. A general analytic correction for multicomponent mixtures would eliminate the need to perform MD simulations for several system sizes and extrapolate mutual diffusion coefficients to the thermodynamic limit.

In the second part of this thesis, chapters 6 and 7, the focus is on the improvement of force fields parameters. The accuracy of a force field determines the accuracy of computed thermodynamic, structural, and transport properties from molecular simulation. For two systems of carbohydrate (mono- and disaccharides) and cyclic ether (crown-ether) molecules, the parameters of classical force fields are adjusted to provide accurate thermodynamic and transport properties. While different intermolecular and intramolecular potential parameters can be adjusted, an understanding of the limitation of the used force field helps to determine which interaction parameters should be modified. For systems of carbohydrates, strong intermolecular attraction between carbohydrate molecules results in aggregation of these molecules and consequently more viscous aqueous solutions. Scaling the energy parameters of Lennard-Jones interactions and electrostatic interactions consistently improves the performance of the force field. For crown-ethers, the original TraPPE force field was developed for linear ether molecules, so the intramolecular potential parameters, especially torsional potentials, are not be transferable to cyclic ether molecules. Refitting the torsional potential parameters to interactions obtained from quantum mechanics significantly improves the accuracy of the force field for computing transport and thermodynamic (solubility) properties. These two case studies show how to analyze shortcomings of a force field and help adjust the parameters of other force fields as well in a similar way.

BIBLIOGRAPHY

[1] R. B. Bird, *Transport Phenomena*, 2nd ed. (John Wiley & Sons, New York, 2007).

[2] A. L. Lehninger, D. L. Nelson, and M. M. Cox, *Lehninger Principles of Biochemistry*, 6th ed. (W.H. Freeman and Company, New York, 2013).

[3] S. Rahmstorf, *Thermohaline Circulation: The Current Climate,* Nature **421**, 699–699 (2003).

[4] N. D. Katopodes, *Free-Surface Flow: Environmental Fluid Mechanics*, 1st ed. (Butterworth-Heinemann, Oxford, 2018).

[5] S. Antman, J. Marsden, and L. Sirovich, eds., *Microflows and Nanoflows*, Interdisciplinary Applied Mathematics, Vol. 29 (Springer-Verlag, New York, 2005).

[6] J. Warnatz, U. Maas, and R. W. Dibble, *Combustion: Physical and Chemical Fundamentals, Modeling and Simulation, Experiments, Pollutant Formation*, 4th ed. (Springer, Berlin, 2006).

[7] B. Lautrup, *Physics of Continuous Matter: Exotic and Everyday Phenomena in the Macroscopic World*, 2nd ed. (CRC Press, New York, 2011).

[8] J. Millat, J. H. Dymond, and C. A. Nieto de Castro, *Transport Properties of Fluids Their Correlation, Prediction and Estimation* (Cambridge University Press, Cambridge, 1996).

[9] R. Taylor and R. Krishna, *Multicomponent Mass Transfer*, 1st ed. (John Wiley & Sons, New York, 1993).

[10] S. Kjelstrup and D. Bedeaux, *Non-equilibrium Thermodynamics of Heterogeneous Systems*, 1st ed., Series on Advances in Statistical Mechanics, Vol. 16 (World Scientific, Singapore, 2008).

[11] S. R. de Groot and P. Mazur, *Non-Equilibrium Thermodynamics* (Dover Publications, New York, 1962).

[12] S. Kjelstrup, D. Bedeaux, E. Johannessen, and J. Gross, *Non-equilibrium Thermodynamics for Engineers*, 1st ed. (World Scientific, Singapore, 2010).

[13] W. A. Wakehm, A. Nagashima, and J. V. Sengers, eds., *Experimental Thermodynamics, Vol. III: Measurement of the Transport Properties of Fluids* (Blackwell Scientific Publications, Oxford, 1991).

[14] B. E. Poling, J. M. Prausnitz, and J. P. O'Connel, *The Properties of Gases and Liquids*, 5th ed. (McGraw-Hill, Singapore, 2001).

[15] A. Bardow, W. Marquardt, V. Göke, H.-J. Koss, and K. Lucas, *Model-Based Measurement of Diffusion Using Raman Spectroscopy,* AIChE Journal **49**, 323–334 (2003).

[16] A. Bardow, V. Göke, H.-J. Koß, and W. Marquardt, *Ternary Diffusivities by Model-Based Analysis of Raman Spectroscopy Measurements,* AIChE Journal **52**, 4004–4015 (2006).

[17] S. Parez, G. Guevara-Carrion, H. Hasse, and J. Vrabec, *Mutual Diffusion in the Ternary Mixture of Water + Methanol + Ethanol and its Binary Subsystems,* Physical Chemistry Chemical Physics **15**, 3985 (2013).

[18] C. Peters, L. Wolff, T. J. H. Vlugt, and A. Bardow, *Diffusion in Liquids: Experiments, Molecular Dynamics, and Engineering Models,* in *Experimental Thermodynamics Volume X*, edited by D. Bedeaux, S. Kjelstrup, and J. Sengers (Royal Society of Chemistry, Croydon, 2015) Chap. 5, pp. 78–104.

[19] J. E. Goodrich and R. S. Porter, *A Rheological Interpretation of Torque-rheometer Data,* Polymer Engineering and Science **7**, 45–51 (1967).

[20] G. G. Fuller, C. A. Cathey, B. Hubbard, and B. E. Zebrowski, *Extensional Viscosity Measurements for Low-Viscosity Fluids,* Journal of Rheology **31**, 235–249 (1987).

[21] S. Bair, Y. Liu, and Q. J. Wang, *The Pressure-Viscosity Coefficient for Newtonian EHL Film Thickness With General Piezoviscous Response,* Journal of Tribology **128**, 624 (2006).

[22] R. Alcalde, G. García, M. Atilhan, and S. Aparicio, *Systematic Study on the Viscosity of Ionic Liquids: Measurement and Prediction,* Industrial & Engineering Chemistry Research **54**, 10918–10924 (2015).

[23] G. Emanuel, *Bulk Viscosity in the Navier-Stokes Equations,* International Journal of Engineering Science **36**, 1313–1323 (1998).

[24] R. E. Graves and B. M. Argrow, *Bulk Viscosity: Past to Present,* Journal of Thermophysics and Heat Transfer **13**, 337–342 (1999).

[25] A. S. Meijer, A. S. de Wijn, M. F. E. Peters, N. J. Dam, and W. van de Water, *Coherent Rayleigh-Brillouin Scattering Measurements of Bulk Viscosity of Polar and Nonpolar Gases, and Kinetic Theory,* Journal of Chemical Physics **133**, 164315 (2010).

[26] Z. Gu, W. Ubachs, W. Marques, and W. van de Water, *Rayleigh-Brillouin Scattering in Binary-Gas Mixtures,* Physical Review Letters **114**, 243902 (2015).

[27] S. H. Jamali, M. de Groen, O. A. Moultos, R. Hartkamp, T. J. H. Vlugt, W. Ubachs, and W. van de Water, *Rayleigh-Brillouin Light Scattering Spectra of CO_2 from Molecular Dynamics,* Journal of Chemical Physics **151**, 064201 (2019).

[28] A. P. Fröba, M. H. Rausch, K. Krzeminski, D. Assenbaum, P. Wasserscheid, and A. Leipertz, *Thermal Conductivity of Ionic Liquids: Measurement and Prediction,* International Journal of Thermophysics **31**, 2059–2077 (2010).

[29] S. Chapman and T. G. Cowling, *The Mathematical Theory of Non-Uniform Gases*, 3rd ed. (Cambridge, 1970).

[30] J. H. Dymond, *Hard-Sphere Theories of Transport Properties,* Chemical Society Reviews **14**, 317 (1985).

[31] Y. Rosenfeld, *Relation between the Transport Coefficients and the Internal Entropy of Simple Systems,* Physical Review A **15**, 2545–2549 (1977).

[32] Y. Rosenfeld, *Variational Soft-sphere Perturbation Theory and Conditions for a Grüneisen Equation of State for Dense Fluids,* Physical Review A **28**, 3063–3069 (1983).

[33] Y. Rosenfeld, *A Quasi-Universal Scaling Law for Atomic Transport in Simple Fluids,* Journal of Physics: Condensed Matter **11**, 5415–5427 (1999).

[34] C. Peters, J. Thien, L. Wolff, H.-J. Koß, and A. Bardow, *Quaternary Diffusion Coefficients in Liquids from Microfluidics and Raman Microspectroscopy: Cyclohexane + Toluene + Acetone + Methanol,* Journal of Chemical & Engineering Data , in press, https://doi.org/10.1021/acs.jced.9b00632 (2019).

[35] D. Frenkel and B. Smit, *Understanding Molecular Simulation: From Algorithms to Applications*, 2nd ed. (Academic Press, London, 2002).

[36] M. P. Allen and D. J. Tildesley, *Computer Simulation of Liquids*, 2nd ed. (Oxford University Press, Croydon, 2017).

[37] F. Llovell, R. M. Marcos, and L. F. Vega, *Free-Volume Theory Coupled with Soft-SAFT for Viscosity Calculations: Comparison with Molecular Simulation and Experimental Data,* Journal of Physical Chemistry B **117**, 8159–8171 (2013).

[38] O. Lötgering-Lin, A. Schöniger, W. Nowak, and J. Gross, *Bayesian Model Selection Helps To Choose Objectively between Thermodynamic Models: A Demonstration of Selecting a Viscosity Model Based on Entropy Scaling,* Industrial & Engineering Chemistry Research **55**, 10191–10207 (2016).

[39] O. Lötgering-Lin, M. Fischer, M. Hopp, and J. Gross, *Pure Substance and Mixture Viscosities Based on Entropy Scaling and an Analytic Equation of State,* Industrial & Engineering Chemistry Research **57**, 4095–4114 (2018).

[40] L. Wolff, S. H. Jamali, T. M. Becker, O. A. Moultos, T. J. H. Vlugt, and A. Bardow, *Prediction of Composition-Dependent Self-Diffusion Coefficients in Binary Liquid Mixtures: The Missing Link for Darken-Based Models,* Industrial & Engineering Chemistry Research **57**, 14784–14794 (2018).

[41] B. J. Alder and T. E. Wainwright, *Studies in Molecular Dynamics. I. General Method,* Journal of Chemical Physics **31**, 459–466 (1959).

[42] J.-P. Hansen and I. R. McDonald, *Theory of Simple Liquids*, 3rd ed. (Academic Press, Amsterdam, 2006).

[43] S. I. Sandler, *An Introduction to Applied Statistical Thermodynamics*, 1st ed. (John Wiley & Sons, Hoboken, 2010).

[44] B. J. Alder, D. M. Gass, and T. E. Wainwright, *Studies in Molecular Dynamics. VIII. The Transport Coefficients for a Hard-Sphere Fluid,* Journal of Chemical Physics **53**, 3813–3826 (1970).

[45] S. A. Adcock and J. A. McCammon, *Molecular Dynamics: Survey of Methods for Simulating the Activity of Proteins,* Chemical Reviews **106**, 1589–1615 (2006).

[46] D. E. Discher, V. Ortiz, G. Srinivas, M. L. Klein, Y. Kim, D. Christian, S. Cai, P. Photos, and F. Ahmed, *Emerging Applications of Polymersomes in Delivery: From Molecular Dynamics to Shrinkage of Tumors,* Progress in Polymer Science **32**, 838–857 (2007).

[47] A. Bunker, *Poly(Ethylene Glycol) in Drug Delivery, Why Does it Work, and Can We do Better? All Atom Molecular Dynamics Simulation Provides Some Answers,* Physics Procedia **34**, 24–33 (2012).

[48] N. C. Ekdawi-Sever, P. B. Conrad, and J. J. de Pablo, *Molecular Simulation of Sucrose Solutions near the Glass Transition Temperature,* Journal of Physical Chemistry A **105**, 734–742 (2001).

[49] S. H. Mushrif, S. Caratzoulas, and D. G. Vlachos, *Understanding Solvent Effects in the Selective Conversion of Fructose to 5-hydroxymethyl-furfural: A Molecular Dynamics Investigation,* Physical Chemistry Chemical Physics **14**, 2637 (2012).

[50] J. Sauter and A. Grafmüller, *Predicting the Chemical Potential and Osmotic Pressure of Polysaccharide Solutions by Molecular Simulations,* Journal of Chemical Theory and Computation **12**, 4375–4384 (2016).

[51] W. K. Lay, M. S. Miller, and A. H. Elcock, *Reparameterization of Solute-solute Interactions for Amino Acid-sugar Systems Using Isopiestic Osmotic Pressure Molecular Dynamics Simulations,* Journal of Chemical Theory and Computation **13**, 1874–1882 (2017).

[52] T. van Westen and R. D. Groot, *Predicting the Kinetics of Ice Recrystallization in Aqueous Sugar Solutions,* Crystal Growth & Design **18**, 2405–2416 (2018).

[53] B. Smit and T. L. M. Maesen, *Molecular Simulations of Zeolites: Adsorption, Diffusion, and Shape Selectivity,* Chemical Reviews **108**, 4125–4184 (2008).

[54] T. Bučko, L. Benco, J. Hafner, and J. G. Ángyán, *Monomolecular Cracking of Propane over Acidic Chabazite: An Ab Initio Molecular Dynamics and Transition Path Sampling Study,* Journal of Catalysis **279**, 220–228 (2011).

[55] F. Castro-Marcano and A. C. van Duin, *Comparison of Thermal and Catalytic Cracking of 1-heptene from ReaxFF Reactive Molecular Dynamics Simulations,* Combustion and Flame **160**, 766–775 (2013).

[56] A. Poursaeidesfahani, M. F. de Lange, F. Khodadadian, D. Dubbeldam, M. Rigutto, N. Nair, and T. J. H. Vlugt, *Product Shape Selectivity of MFI-type, MEL-type, and BEA-type Zeolites in the Catalytic Hydroconversion of Heptane,* Journal of Catalysis **353**, 54–62 (2017).

[57] Z. A. Makrodimitri, D. J. M. Unruh, and I. G. Economou, *Molecular Simulation of Diffusion of Hydrogen, Carbon Monoxide, and Water in Heavy n -Alkanes,* Journal of Physical Chemistry B **115**, 1429–1439 (2011).

[58] O. A. Moultos, I. N. Tsimpanogiannis, A. Z. Panagiotopoulos, and I. G. Economou, *Atomistic Molecular Dynamics Simulations of CO_2 Diffusivity in H_2O for a Wide Range of Temperatures and Pressures,* Journal of Physical Chemistry B **118**, 5532–5541 (2014).

[59] S. Budhathoki, J. K. Shah, and E. J. Maginn, *Molecular Simulation Study of the Performance of Supported Ionic Liquid Phase Materials for the Separation of Carbon Dioxide from Methane and Hydrogen,* Industrial & Engineering Chemistry Research **56**, 6775–6784 (2017).

[60] A. Otani, Y. Zhang, T. Matsuki, E. Kamio, H. Matsuyama, and E. J. Maginn, *Molecular Design of High CO_2 Reactivity and Low Viscosity Ionic Liquids for CO_2 Separative Facilitated Transport Membranes,* Industrial & Engineering Chemistry Research **55**, 2821–2830 (2016).

[61] *Industrial Fluid Properties Simulation Challenge (IFPSC),* `https://fluidproperties.org` (accessed 21 November 2019).

[62] L. Costigliola, U. R. Pedersen, D. M. Heyes, T. B. Schrøder, and J. C. Dyre, *Communication: Simple Liquids' High-Density Viscosity,* Journal of Chemical Physics **148**, 081101 (2018).

[63] M. A. Galvani Cunha and M. O. Robbins, *Determination of Pressure-Viscosity Relation of 2,2,4-trimethylhexane by All-atom Molecular Dynamics Simulations,* Fluid Phase Equilibria **495**, 28–32 (2019).

[64] R. A. Messerly, M. C. Anderson, S. M. Razavi, and J. R. Elliott, *Mie 16-6 Force Field Predicts Viscosity with Faster-than-exponential Pressure Dependence for 2,2,4-trimethylhexane,* Fluid Phase Equilibria **495**, 76–85 (2019).

[65] L. Zheng, J. M. Trusler, F. Bresme, and E. A. Müller, *Predicting the Pressure Dependence of the Viscosity of 2,2,4-trimethylhexane Using the SAFT Coarse-grained Force Field,* Fluid Phase Equilibria **496**, 1–6 (2019).

[66] K. Kremer and G. S. Grest, *Dynamics of Entangled Linear Polymer Melts: A Molecular-Dynamics Simulation,* Journal of Chemical Physics **92**, 5057–5086 (1990).

[67] M. Karplus and J. A. McCammon, *Molecular Dynamics Simulations of Biomolecules,* Nature Structural Biology **9**, 646–652 (2002).

[68] M. Karplus and J. Kuriyan, *Molecular Dynamics and Protein Function,* Proceedings of the National Academy of Sciences **102**, 6679–6685 (2005).

[69] E. Fadda and R. J. Woods, *Molecular Simulations of Carbohydrates and Protein-Carbohydrate Interactions: Motivation, Issues and Prospects,* Drug Discovery Today **15**, 596–609 (2010).

[70] H. Liu, E. Maginn, A. E. Visser, N. J. Bridges, and E. B. Fox, *Thermal and Transport Properties of Six Ionic Liquids: An Experimental and Molecular Dynamics Study,* Industrial & Engineering Chemistry Research **51**, 7242–7254 (2012).

[71] M. Casalegno, G. Raos, G. B. Appetecchi, S. Passerini, F. Castiglione, and A. Mele, *From Nanoscale to Microscale: Crossover in the Diffusion Dynamics within Two Pyrrolidinium-Based Ionic Liquids,* Journal of Physical Chemistry Letters **8**, 5196–5202 (2017).

[72] B. F. E. Curchod and T. J. Martínez, *Ab Initio Nonadiabatic Quantum Molecular Dynamics,* Chemical Reviews **118**, 3305–3336 (2018).

[73] C. Oostenbrink, A. Villa, A. E. Mark, and W. F. van Gunsteren, *A Biomolecular Force Field Based on the Free Enthalpy of Hydration and Solvation: The GROMOS Force-field Parameter Sets 53A5 and 53A6,* Journal of Computational Chemistry **25**, 1656–1676 (2004).

[74] T. Tsuneda, *Density Functional Theory in Quantum Chemistry*, 1st ed. (Springer, Tokyo, 2014).

[75] M. G. Martin and J. I. Siepmann, *Transferable Potentials for Phase Equilibria. 1. United-Atom Description of n-Alkanes,* Journal of Physical Chemistry B **102**, 2569–2577 (1998).

[76] M. G. Martin and J. I. Siepmann, *Novel Configurational-Bias Monte Carlo Method for Branched Molecules. Transferable Potentials for Phase Equilibria. 2. United-Atom Description of Branched Alkanes,* Journal of Physical Chemistry B **103**, 4508–4517 (1999).

[77] B. Chen, J. J. Potoff, and J. I. Siepmann, *Monte Carlo Calculations for Alcohols and Their Mixtures with Alkanes. Transferable Potentials for Phase Equilibria. 5. United-Atom Description of Primary, Secondary, and Tertiary Alcohols,* Journal of Physical Chemistry B **105**, 3093–3104 (2001).

[78] J. M. Stubbs, J. J. Potoff, and J. I. Siepmann, *Transferable Potentials for Phase Equilibria. 6. United-Atom Description for Ethers, Glycols, Ketones, and Aldehydes,* Journal of Physical Chemistry B **108**, 17596–17605 (2004).

[79] C. D. Wick, J. M. Stubbs, N. Rai, and J. I. Siepmann, *Transferable Potentials for Phase Equilibria. 7. Primary, Secondary, and Tertiary Amines, Nitroalkanes and Nitrobenzene, Nitriles, Amides, Pyridine, and Pyrimidine,* Journal of Physical Chemistry B **109**, 18974–18982 (2005).

[80] N. Lubna, G. Kamath, J. J. Potoff, N. Rai, and J. I. Siepmann, *Transferable Potentials for Phase Equilibria. 8. United-Atom Description for Thiols, Sulfides, Disulfides, and Thiophene,* Journal of Physical Chemistry B **109**, 24100–24107 (2005).

[81] S. J. Keasler, S. M. Charan, C. D. Wick, I. G. Economou, and J. I. Siepmann, *Transferable Potentials for Phase Equilibria–United Atom Description of Five- and Six-Membered Cyclic Alkanes and Ethers,* Journal of Physical Chemistry B **116**, 11234–11246 (2012).

[82] W. L. Jorgensen, D. S. Maxwell, and J. Tirado-Rives, *Development and Testing of the OPLS All-Atom Force Field on Conformational Energetics and Properties of Organic Liquids,* Journal of the American Chemical Society **118**, 11225–11236 (1996).

[83] W. Damm, A. Frontera, J. Tirado-Rives, and W. L. Jorgensen, *OPLS All-Atom Force Field for Carbohydrates,* Journal of Computational Chemistry **18**, 1955–1970 (1997).

[84] S. W. I. Siu, K. Pluhackova, and R. A. Böckmann, *Optimization of the OPLS-AA Force Field for Long Hydrocarbons,* Journal of Chemical Theory and Computation **8**, 1459–1470 (2012).

[85] E. Harder, W. Damm, J. Maple, C. Wu, M. Reboul, J. Y. Xiang, L. Wang, D. Lupyan, M. K. Dahlgren, J. L. Knight, J. W. Kaus, D. S. Cerutti, G. Krilov, W. L. Jorgensen, R. Abel, and R. A. Friesner, *OPLS3: A Force Field Providing Broad Coverage of Drug-like Small Molecules and Proteins,* Journal of Chemical Theory and Computation **12**, 281–296 (2016).

[86] S. J. Weiner, P. A. Kollman, D. A. Case, U. C. Singh, C. Ghio, G. Alagona, S. Profeta, and P. Weiner, *A New Force Field for Molecular Mechanical Simulation of Nucleic Acids and Proteins,* Journal of the American Chemical Society **106**, 765–784 (1984).

[87] W. D. Cornell, P. Cieplak, C. I. Bayly, I. R. Gould, K. M. Merz, D. M. Ferguson, D. C. Spellmeyer, T. Fox, J. W. Caldwell, and P. A. Kollman, *A Second Generation Force Field for the Simulation of Proteins, Nucleic Acids, and Organic Molecules,* Journal of the American Chemical Society **117**, 5179–5197 (1995).

[88] J. Wang, R. M. Wolf, J. W. Caldwell, P. A. Kollman, and D. A. Case, *Development and Testing of a General Amber Force Field,* Journal of Computational Chemistry **25**, 1157–1174 (2004).

[89] Y. Zhang, Y. Zhang, M. J. McCready, and E. J. Maginn, *Evaluation and Refinement of the General AMBER Force Field for Nineteen Pure Organic Electrolyte Solvents,* Journal of Chemical & Engineering Data **63**, 3488–3502 (2018).

[90] A. D. MacKerell, D. Bashford, M. Bellott, R. L. Dunbrack, J. D. Evanseck, M. J. Field, S. Fischer, J. Gao, H. Guo, S. Ha, D. Joseph-McCarthy, L. Kuchnir, K. Kuczera, F. T. K. Lau, C. Mattos, S. Michnick, T. Ngo, D. T. Nguyen, B. Prodhom, W. E. Reiher, B. Roux, M. Schlenkrich, J. C. Smith, R. Stote, J. Straub, M. Watanabe, J. Wiórkiewicz-Kuczera, D. Yin, and M. Karplus, *All-Atom Empirical Potential for Molecular Modeling and Dynamics Studies of Proteins,* Journal of Physical Chemistry B **102**, 3586–3616 (1998).

[91] O. Guvench, S. S. Mallajosyula, E. P. Raman, E. Hatcher, K. Vanommeslaeghe, T. J. Foster, F. W. Jamison, and A. D. MacKerell, *CHARMM Additive All-atom Force Field for Carbohydrate Derivatives and Its Utility in Polysaccharide and Carbohydrate-protein Modeling,* Journal of Chemical Theory and Computation **7**, 3162–3180 (2011).

[92] A. K. Rappe, C. J. Casewit, K. S. Colwell, W. A. Goddard, and W. M. Skiff, *UFF, a Full Periodic Table Force Field for Molecular Mechanics and Molecular Dynamics Simulations,* Journal of the American Chemical Society **114**, 10024–10035 (1992).

[93] C. I. Bayly, P. Cieplak, W. Cornell, and P. A. Kollman, *A Well-behaved Electrostatic Potential Based Method Using Charge Restraints for Deriving Atomic Charges: The RESP Model,* Journal of Physical Chemistry **97**, 10269–10280 (1993).

[94] D. S. Maxwell, J. Tirado-Rives, and W. L. Jorgensen, *A Comprehensive Study of the Rotational Energy Profiles of Organic Systems by Ab Initio MO Theory, Forming a Basis for Peptide Torsional Parameters,* Journal of Computational Chemistry **16**, 984–1010 (1995).

[95] P. Comba, *Inorganic and Bioinorganic Molecular Mechanics Modeling-the Problem of the Force Field Parameterization,* Coordination Chemistry Reviews **238-239**, 9–20 (2003).

[96] L.-C. Lin, K. Lee, L. Gagliardi, J. B. Neaton, and B. Smit, *Force-field Development from Electronic Structure Calculations with Periodic Boundary Conditions: Applications to Gaseous Adsorption and Transport in Metal-organic Frameworks,* Journal of Chemical Theory and Computation **10**, 1477–1488 (2014).

[97] P. S. Nerenberg and T. Head-Gordon, *New Developments in Force Fields for Biomolecular Simulations,* Current Opinion in Structural Biology **49**, 129–138 (2018).

[98] R. Zwanzig, *Time-Correlation Functions and Transport Coefficients in Statistical Mechanics,* Annual Review of Physical Chemistry **16**, 67–102 (1965).

[99] D. J. Evans and G. Morriss, *Statistical Mechanics of Nonequilibrium Liquids*, 2nd ed. (Cambridge University Press, Cambridge, 2008).

[100] M. H. J. Hagen, C. P. Lowe, and D. Frenkel, *Long Time Tails in Stress Correlation Functions,* in *25 Years of Non-Equilibrium Statistical Mechanics* (Springer Berlin Heidelberg, Berlin, Heidelberg, 2005) pp. 240–249.

[101] M. A. van der Hoef and D. Frenkel, *Long-time Tails of the Velocity Autocorrelation Function in Two- and Three-dimensional Lattice-gas Cellular Automata: A Test of Mode-coupling Theory,* Physical Review A **41**, 4277–4284 (1990).

[102] Y. Zhang, A. Otani, and E. J. Maginn, *Reliable Viscosity Calculation from Equilibrium Molecular Dynamics Simulations: A Time Decomposition Method,* Journal of Chemical Theory and Computation **11**, 3537–3546 (2015).

[103] E. J. Maginn, R. A. Messerly, D. J. Carlson, D. R. Roe, and J. R. Elliott, *Best Practices for Computing Transport Properties 1. Self-Diffusivity and Viscosity from Equilibrium Molecular Dynamics [Article v1.0],* Living Journal of Computational Molecular Science **1**, 1–20 (2019).

[104] C. M. Tenney and E. J. Maginn, *Limitations and Recommendations for the Calculation of Shear Viscosity using Reverse Nonequilibrium Molecular Dynamics,* Journal of Chemical Physics **132**, 014103 (2010).

[105] D. R. Wheeler and J. Newman, *Molecular Dynamics Simulations of Multicomponent Diffusion. 2. Nonequilibrium Method,* Journal of Physical Chemistry B **108**, 18362–18367 (2004).

[106] D. R. Wheeler and J. Newman, *Molecular Dynamics Simulations of Multicomponent Diffusion. 1. Equilibrium Method,* Journal of Physical Chemistry B **108**, 18353–18361 (2004).

[107] X. Liu, S. K. Schnell, J.-M. Simon, P. Krüger, D. Bedeaux, S. Kjelstrup, A. Bardow, and T. J. H. Vlugt, *Diffusion Coefficients from Molecular Dynamics Simulations in Binary and Ternary Mixtures,* International Journal of Thermophysics **34**, 1169–1196 (2013).

[108] B. Hess, *Determining the Shear Viscosity of Model Liquids from Molecular Dynamics Simulations,* Journal of Chemical Physics **116**, 209 (2002).

[109] T. Chen, B. Smit, and A. T. Bell, *Are Pressure Fluctuation-based Equilibrium Methods Really Worse than Nonequilibrium Methods for Calculating Viscosities?* Journal of Chemical Physics **131**, 246101 (2009).

[110] R. Hartkamp, S. Bernardi, and B. D. Todd, *Transient-Time Correlation Function Applied to Mixed Shear and Elongational Flows,* Journal of Chemical Physics **136**, 064105 (2012).

[111] D. Cohen-Tanugi and J. C. Grossman, *Water Desalination across Nanoporous Graphene,* Nano Letters **12**, 3602–3608 (2012).

[112] L.-C. Lin and J. C. Grossman, *Atomistic Understandings of Reduced Graphene Oxide as an Ultrathin-film Nanoporous Membrane for Separations,* Nature Communications **6**, 8335 (2015).

[113] D. Cohen-Tanugi, L.-C. Lin, and J. C. Grossman, *Multilayer Nanoporous Graphene Membranes for Water Desalination,* Nano Letters **16**, 1027–1033 (2016).

[114] J. D. Evans, D. M. Huang, M. R. Hill, C. J. Sumby, A. W. Thornton, and C. J. Doonan, *Feasibility of Mixed Matrix Membrane Gas Separations Employing Porous Organic Cages,* Journal of Physical Chemistry C **118**, 1523–1529 (2014).

[115] A. Ozcan, C. Perego, M. Salvalaglio, M. Parrinello, and O. Yazaydin, *Concentration Gradient Driven Molecular Dynamics: A New Method for Simulations of Membrane Permeation and Separation,* Chemical Science **8**, 3858–3865 (2017).

[116] J. Ramírez, S. K. Sukumaran, B. Vorselaars, and A. E. Likhtman, *Efficient on the Fly Calculation of Time Correlation Functions in Computer Simulations,* Journal of Chemical Physics **133**, 154103 (2010).

[117] D. Dubbeldam, D. C. Ford, D. E. Ellis, and R. Q. Snurr, *A New Perspective on the Order-n Algorithm for Computing Correlation Functions,* Molecular Simulation **35**, 1084–1097 (2009).

[118] I.-C. Yeh and G. Hummer, *System-Size Dependence of Diffusion Coefficients and Viscosities from Molecular Dynamics Simulations with Periodic Boundary Conditions,* Journal of Physical Chemistry B **108**, 15873–15879 (2004).

[119] B. Dünweg and K. Kremer, *Molecular Dynamics Simulation of a Polymer Chain in Solution,* Journal of Chemical Physics **99**, 6983–6997 (1993).

[120] D. P. Sellan, E. S. Landry, J. E. Turney, A. J. H. McGaughey, and C. H. Amon, *Size Effects in Molecular Dynamics Thermal Conductivity Predictions,* Physical Review B **81**, 214305 (2010).

[121] J. M. Young and A. Z. Panagiotopoulos, *System-Size Dependence of Electrolyte Activity Coefficients in Molecular Simulations,* Journal of Physical Chemistry B **122**, 3330–3338 (2018).

[122] J. I. Siepmann, I. R. McDonald, and D. Frenkel, *Finite-size Corrections to the Chemical Potential,* Journal of Physics: Condensed Matter **4**, 679–691 (1992).

[123] P. Krüger, S. K. Schnell, D. Bedeaux, S. Kjelstrup, T. J. H. Vlugt, and J.-M. Simon, *Kirkwood-Buff Integrals for Finite Volumes,* Journal of Physical Chemistry Letters **4**, 235–238 (2013).

[124] P. Krüger and T. J. H. Vlugt, *Size and Shape Dependence of Finite-volume Kirkwood-Buff Integrals,* Physical Review E **97**, 051301 (2018).

[125] N. Dawass, P. Krüger, S. K. Schnell, J.-M. Simon, and T. J. H. Vlugt, *Kirkwood-Buff Integrals from Molecular Simulation,* Fluid Phase Equilibria **486**, 21–36 (2019).

[126] S. Plimpton, *Fast Parallel Algorithms for Short-Range Molecular Dynamics,* Journal of Computational Physics **117**, 1–19 (1995).

[127] G. Moggridge, *Prediction of the Mutual Diffusivity in Binary Non-ideal Liquid Mixtures from the Tracer Diffusion Coefficients,* Chemical Engineering Science **71**, 226–238 (2012).

[128] G. Guevara-Carrion, T. Janzen, Y. M. Muñoz-Muñoz, and J. Vrabec, *Mutual Diffusion of Binary Liquid Mixtures Containing Methanol, Ethanol, Acetone, Benzene, Cyclohexane, Toluene, and Carbon Tetrachloride,* Journal of Chemical Physics **144**, 124501 (2016).

[129] Q. Zhu, C. D'Agostino, M. Ainte, M. Mantle, L. Gladden, O. Ortona, L. Paduano, D. Ciccarelli, and G. Moggridge, *Prediction of Mutual Diffusion Coefficients in Binary Liquid Systems with One Self-associating Component from Viscosity Data and Intra-diffusion Coefficients at Infinite Dilution,* Chemical Engineering Science **147**, 118–127 (2016).

[130] M. Hopp, J. Mele, and J. Gross, *Self-diffusion Coefficients from Entropy Scaling Using the PCP-SAFT Equation of State,* Industrial & Engineering Chemistry Research **57**, 12942–12950 (2018).

[131] G. Galliéro, C. Boned, and A. Baylaucq, *Molecular Dynamics Study of the Lennard-Jones Fluid Viscosity: Application to Real Fluids,* Industrial & Engineering Chemistry Research **44**, 6963–6972 (2005).

[132] S. Morioka, *The Transport Coefficients Described in the Dense Gas-Like Model,* Journal of Non-Crystalline Solids **363**, 152–160 (2013).

[133] O. Lötgering-Lin and J. Gross, *Group Contribution Method for Viscosities Based on Entropy Scaling Using the Perturbed-Chain Polar Statistical Associating Fluid Theory,* Industrial & Engineering Chemistry Research **54**, 7942–7952 (2015).

[134] M. Hopp, J. Mele, R. Hellmann, and J. Gross, *Thermal Conductivity via Entropy Scaling: An Approach That Captures the Effect of Intramolecular Degrees of Freedom,* Industrial & Engineering Chemistry Research **58**, 18432–18438 (2019).

[135] M. Hopp and J. Gross, *Thermal Conductivity from Entropy Scaling: A Group-Contribution Method,* Industrial & Engineering Chemistry Research **58**, 20441–20449 (2019).

[136] J. J. Potoff and J. I. Siepmann, *Vapor-Liquid Equilibria of Mixtures Containing Alkanes, Carbon Dioxide, and Nitrogen,* AIChE Journal **47**, 1676–1682 (2001).

[137] S. H. Jamali, T. J. H. Vlugt, and L.-C. Lin, *Atomistic Understanding of Zeolite Nanosheets for Water Desalination,* Journal of Physical Chemistry C **121**, 11273–11280 (2017).

[138] N. Ghaffour, T. M. Missimer, and G. L. Amy, *Technical Review and Evaluation of the Economics of Water Desalination: Current and Future Challenges for Better Water Supply Sustainability,* Desalination **309**, 197–207 (2013).

[139] C. J. Vörösmarty, P. Green, J. Salisbury, and R. B. Lammers, *Global Water Resources: Vulnerability from Climate Change and Population Growth,* Science **289**, 284–288 (2000).

[140] A. Mohammad, Y. Teow, W. Ang, Y. Chung, D. Oatley-Radcliffe, and N. Hilal, *Nanofiltration Membranes Review: Recent Advances and Future Prospects,* Desalination **356**, 226–254 (2015).

[141] L. F. Greenlee, D. F. Lawler, B. D. Freeman, B. Marrot, and P. Moulin, *Reverse Osmosis Desalination: Water Sources, Technology, and Today's Challenges,* Water Research **43**, 2317–2348 (2009).

[142] M. M. Pendergast and E. M. Hoek, *A Review of Water Treatment Membrane Nanotechnologies,* Energy & Environmental Science **4**, 1946–1971 (2011).

[143] D. Cohen-Tanugi, R. K. McGovern, S. H. Dave, J. H. Lienhard, and J. C. Grossman, *Quantifying the Potential of Ultra-permeable Membranes for Water Desalination,* Energy & Environmental Science **7**, 1134–1141 (2014).

[144] S. P. Surwade, S. N. Smirnov, I. V. Vlassiouk, R. R. Unocic, G. M. Veith, S. Dai, and S. M. Mahurin, *Water Desalination Using Nanoporous Single-layer Graphene,* Nature Nanotechnology **10**, 459–464 (2015).

[145] D. Cohen-Tanugi and J. C. Grossman, *Nanoporous Graphene as a Reverse Osmosis Membrane: Recent Insights from Theory and Simulation,* Desalination **366**, 59–70 (2015).

[146] S. Dervin, D. D. Dionysiou, and S. C. Pillai, *2D Nanostructures for Water Purification: Graphene and Beyond,* Nanoscale **8**, 15115–15131 (2016).

[147] Y. You, V. Sahajwalla, M. Yoshimura, and R. K. Joshi, *Graphene and Graphene Oxide for Desalination,* Nanoscale **8**, 117–119 (2016).

[148] B. Mi, *Graphene Oxide Membranes for Ionic and Molecular Sieving,* Science **343**, 740–742 (2014).

[149] L.-C. Lin, J. Choi, and J. C. Grossman, *Two-dimensional Covalent triazine Framework as an Ultrathin-film Nanoporous Membrane for Desalination,* Chemical Communications **51**, 14921–14924 (2015).

[150] M. Heiranian, A. B. Farimani, and N. R. Aluru, *Water Desalination with a Single-layer MoS_2 Nanopore,* Nature Communications **6**, 8616 (2015).

[151] M. Xue, H. Qiu, and W. Guo, *Exceptionally Fast Water Desalination at Complete Salt Rejection by Pristine Graphyne Monolayers,* Nanotechnology **24**, 505720 (2013).

[152] C. Zhu, H. Li, X. C. Zeng, E. G. Wang, and S. Meng, *Quantized Water Transport: Ideal Desalination through Graphyne-4 Membrane,* Scientific Reports **3**, 3163 (2013).

[153] J. Kou, X. Zhou, H. Lu, F. Wu, and J. Fan, *Graphyne as the Membrane for Water Desalination,* Nanoscale **6**, 1865–1870 (2014).

[154] K. Varoon, X. Zhang, B. Elyassi, D. D. Brewer, M. Gettel, S. Kumar, J. A. Lee, S. Maheshwari, A. Mittal, C.-Y. Sung, M. Cococcioni, L. F. Francis, A. V. McCormick, K. A. Mkhoyan, and M. Tsapatsis, *Dispersible Exfoliated Zeolite Nanosheets and Their Application as a Selective Membrane,* Science **334**, 72–75 (2011).

[155] X. Zhang, D. Liu, D. Xu, S. Asahina, K. a. Cychosz, K. V. Agrawal, Y. Al Wahedi, A. Bhan, S. Al Hashimi, O. Terasaki, M. Thommes, and M. Tsapatsis, *Synthesis of Self-pillared Zeolite Nanosheets by Repetitive Branching,* Science **336**, 1684–1687 (2012).

[156] W. J. Roth, P. Nachtigall, R. E. Morris, and J. Čejka, *Two-dimensional Zeolites: Current Status and Perspectives,* Chemical Reviews **114**, 4807–4837 (2014).

[157] M. Tsapatsis, *2-dimensional Zeolites,* AIChE Journal **60**, 2374–2381 (2014).

[158] M. Choi, K. Na, J. Kim, Y. Sakamoto, O. Terasaki, and R. Ryoo, *Stable Single-unit-cell Nanosheets of Zeolite MFI as Active and Long-lived Catalysts,* Nature **461**, 828–828 (2009).

[159] J. Dhainaut, T. J. Daou, Y. Bidal, N. Bats, B. Harbuzaru, G. Lapisardi, H. Chaumeil, A. Defoin, L. Rouleau, and J. Patarin, *One-pot Structural Conversion of Magadiite into MFI Zeolite Nanosheets Using Mononitrogen Surfactants as Structure and Shape-directing Agents,* CrystEngComm **15**, 3009 (2013).

[160] U. Díaz and A. Corma, *Layered Zeolitic Materials: An Approach to Designing Versatile Functional Solids,* Dalton Transactions **43**, 10292 (2014).

[161] Y. Luo, Z. Wang, S. Jin, B. Zhang, H. Sun, X. Yuan, and W. Yang, *Synthesis and Crystal Growth Mechanism of ZSM-22 Zeolite Nanosheets,* CrystEngComm **18**, 5611–5615 (2016).

[162] E. Verheyen, C. Jo, M. Kurttepeli, G. Vanbutsele, E. Gobechiya, T. I. Korányi, S. Bals, G. Van Tendeloo, R. Ryoo, C. E. Kirschhock, and J. A. Martens, *Molecular Shape-selectivity of MFI Zeolite Nanosheets in n-decane Isomerization and Hydrocracking,* Journal of Catalysis **300**, 70–80 (2013).

[163] Z. Ren, B. Li, L. Yue, N. Wu, K. Lv, C. Han, and J. Liu, *Hierarchical Porous Nano-MFI Zeolite-pillared Montmorillonite Clay Synthesized by Recrystallization for Hydrocracking of Residual Oil,* RSC Advances **5**, 46104–46108 (2015).

[164] L. Ren, Q. Guo, P. Kumar, M. Orazov, D. Xu, S. M. Alhassan, K. A. Mkhoyan, M. E. Davis, and M. Tsapatsis, *Self-pillared, Single-unit-cell Sn-MFI Zeolite Nanosheets and Their Use for Glucose and Lactose Isomerization,* Angewandte Chemie International Edition **54**, 10848–10851 (2015).

[165] Q. Sun, N. Wang, G. Guo, and J. Yu, *Ultrafast Synthesis of Nano-sized Zeolite SAPO-34 with Excellent MTO Catalytic Performance,* Chemical Communications **51**, 16397–16400 (2015).

[166] Y. Kim, J.-C. Kim, C. Jo, T.-W. Kim, C.-U. Kim, S.-Y. Jeong, and H.-J. Chae, *Structural and Physicochemical Effects of MFI Zeolite Nanosheets for the Selective Synthesis of Propylene from Methanol,* Microporous and Mesoporous Materials **222**, 1–8 (2016).

[167] T. Yutthalekha, C. Wattanakit, C. Warakulwit, W. Wannapakdee, K. Rodponthukwaji, T. Witoon, and J. Limtrakul, *Hierarchical FAU-type Zeolite Nanosheets as Green and Sustainable Catalysts for Benzylation of Toluene,* Journal of Cleaner Production **142**, 1244–1251 (2017).

[168] J. Schick, T. J. Daou, P. Caullet, J.-L. Paillaud, J. Patarin, and C. Mangold-Callarec, *Surfactant-modified MFI Nanosheets: A High Capacity Anion-exchanger,* Chemical Communications **47**, 902–904 (2011).

[169] S. K. Schnell, L. Wu, A. J. J. Koekkoek, S. Kjelstrup, E. J. M. Hensen, and T. J. H. Vlugt, *Adsorption of Argon on MFI Nanosheets: Experiments and Simulations,* Journal of Physical Chemistry C **117**, 24503–24510 (2013).

[170] I. Kabalan, G. Rioland, H. Nouali, B. Lebeau, S. Rigolet, M.-B. Fadlallah, J. Toufaily, T. Hamiyeh, and T. J. Daou, *Synthesis of Purely Silica MFI-type Nanosheets for Molecular Decontamination,* RSC Advances **4**, 37353 (2014).

[171] Y. Hu, J. Wei, Y. Liang, H. Zhang, X. Zhang, W. Shen, and H. Wang, *Zeolitic Imidazolate Framework/Graphene Oxide Hybrid Nanosheets as Seeds for the Growth of Ultrathin Molecular Sieving Membranes,* Angewandte Chemie International Edition **55**, 2048–2052 (2016).

[172] V. Kochkodan and N. Hilal, *A Comprehensive Review on Surface Modified Polymer Membranes for Biofouling Mitigation,* Desalination **356**, 187–207 (2015).

[173] C. Baerlocher, L. B. McCusker, and D. H. Olson, *Atlas of Zeolite Framework Types*, 6th ed. (Elsevier, Amsterdam, 2007).

[174] M. Treacy, I. Rivin, E. Balkovsky, K. Randall, and M. Foster, *Enumeration of Periodic Tetrahedral Frameworks. II. Polynodal Graphs,* Microporous and Mesoporous Materials **74**, 121–132 (2004).

[175] M. W. Deem, R. Pophale, P. A. Cheeseman, and D. J. Earl, *Computational Discovery of New Zeolite-Like Materials,* Journal of Physical Chemistry C **113**, 21353–21360 (2009).

[176] R. Pophale, P. A. Cheeseman, and M. W. Deem, *A Database of New Zeolite-like Materials,* Physical Chemistry Chemical Physics **13**, 12407 (2011).

[177] P. Bai, M. Y. Jeon, L. Ren, C. Knight, M. W. Deem, M. Tsapatsis, and J. I. Siepmann, *Discovery of Optimal Zeolites for Challenging Separations and Chemical Transformations Using Predictive Materials Modeling,* Nature Communications **6**, 5912 (2015).

[178] L. Li, J. Dong, T. M. Nenoff, and R. Lee, *Desalination by Reverse Osmosis Using MFI Zeolite Membranes,* Journal of Membrane Science **243**, 401–404 (2004).

[179] M. Kazemimoghadam and T. Mohammadi, *Synthesis of MFI Zeolite Membranes for Water Desalination,* Desalination **206**, 547–553 (2007).

[180] M. C. Duke, J. O'Brien-Abraham, N. Milne, B. Zhu, J. Y. Lin, and J. C. Diniz da Costa, *Seawater Desalination Performance of MFI Type Membranes Made by Secondary Growth,* Separation and Purification Technology **68**, 343–350 (2009).

[181] M. Kazemimoghadam, *New Nanopore Zeolite Membranes for Water Treatment,* Desalination **251**, 176–180 (2010).

[182] S. Khajavi, J. C. Jansen, and F. Kapteijn, *Production of Ultra Pure Water by Desalination of Seawater Using a Hydroxy Sodalite Membrane,* Journal of Membrane Science **356**, 52–57 (2010).

[183] H. Dong, X. Y. Qu, L. Zhang, L. H. Cheng, H. L. Chen, and C. J. Gao, *Preparation and Characterization of Surface-modified Zeolite-Polyamide Thin Film Nanocomposite Membranes for Desalination,* Desalination and Water Treatment **34**, 6–12 (2011).

[184] Y. Lin and M. C. Duke, *Recent Progress in Polycrystalline Zeolite Membrane Research,* Current Opinion in Chemical Engineering **2**, 209–216 (2013).

[185] B. Zhu, J. Kim, Y.-H. Na, I.-S. Moon, G. Connor, S. Maeda, G. Morris, S. Gray, and M. Duke, *Temperature and Pressure Effects of Desalination Using a MFI-type Zeolite Membrane,* Membranes **3**, 155–168 (2013).

[186] A. Garofalo, L. Donato, E. Drioli, A. Criscuoli, M. Carnevale, O. Alharbi, S. Aljlil, and C. Algieri, *Supported MFI Zeolite Membranes by Cross Flow Filtration for Water Treatment,* Separation and Purification Technology **137**, 28–35 (2014).

[187] B. Zhu, Z. Hong, N. Milne, C. M. Doherty, L. Zou, Y. Lin, A. J. Hill, X. Gu, and M. Duke, *Desalination of Seawater Ion Complexes by MFI-type Zeolite Membranes: Temperature and Long Term Stability,* Journal of Membrane Science **453**, 126–135 (2014).

[188] B. Zhu, D. T. Myat, J.-W. Shin, Y.-H. Na, I.-S. Moon, G. Connor, S. Maeda, G. Morris, S. Gray, and M. Duke, *Application of Robust MFI-type Zeolite Membrane for Desalination of Saline Wastewater,* Journal of Membrane Science **475**, 167–174 (2015).

[189] H. Huang, X. Qu, H. Dong, L. Zhang, and H. Chen, *Role of NaA Zeolites in the Interfacial Polymerization Process towards a Polyamide Nanocomposite Reverse Osmosis Membrane,* RSC Advances **3**, 8203–8207 (2013).

[190] S. G. Kim, D. H. Hyeon, J. H. Chun, B.-H. Chun, and S. H. Kim, *Nanocomposite Poly(Arylene Ether Sulfone) Reverse Osmosis Membrane Containing Functional Zeolite Nanoparticles for Seawater Desalination,* Journal of Membrane Science **443**, 10–18 (2013).

[191] M. M. Pendergast, A. K. Ghosh, and E. Hoek, *Separation Performance and Interfacial Properties of Nanocomposite Reverse Osmosis Membranes,* Desalination **308**, 180–185 (2013).

[192] S. Hosseini, S. Rafiei, A. Hamidi, A. Moghadassi, and S. Madaeni, *Preparation and Electrochemical Characterization of Mixed Matrix Heterogeneous Cation Exchange Membranes Filled with Zeolite Nanoparticles: Ionic Transport Property in Desalination,* Desalination **351**, 138–144 (2014).

[193] H. Dong, L. Zhao, L. Zhang, H. Chen, C. Gao, and W. Winston Ho, *High-flux Reverse Osmosis Membranes Incorporated with NaY Zeolite Nanoparticles for Brackish Water Desalination,* Journal of Membrane Science **476**, 373–383 (2015).

[194] P. Cay-Durgun, C. McCloskey, J. Konecny, A. Khosravi, and M. L. Lind, *Evaluation of Thin Film Nanocomposite Reverse Osmosis Membranes for Long-term Brackish Water Desalination Performance,* Desalination **404**, 304–312 (2017).

[195] Z. E. Hughes, L. A. Carrington, P. Raiteri, and J. D. Gale, *A Computational Investigation into the Suitability of Purely Siliceous Zeolites as Reverse Osmosis Membranes,* Journal of Physical Chemistry C **115**, 4063–4075 (2011).

[196] K. N. Han, S. Bernardi, L. Wang, and D. J. Searles, *Water Diffusion in Zeolite Membranes: Molecular Dynamics Studies on Effects of Water Loading and Thermostat,* Journal of Membrane Science **495**, 322–333 (2015).

[197] Y. Liu and X. Chen, *High Permeability and Salt Rejection Reverse Osmosis by a Zeolite Nano-membrane,* Physical Chemistry Chemical Physics **15**, 6817 (2013).

[198] J. Lin and S. Murad, *A Computer Simulation Study of the Separation of Aqueous Solutions Using Thin Zeolite Membranes,* Molecular Physics **99**, 1175–1181 (2001).

[199] S. Turgman-Cohen, J. C. Araque, E. M. V. Hoek, and F. A. Escobedo, *Molecular Dynamics of Equilibrium and Pressure-driven Transport Properties of Water through LTA-type Zeolites,* Langmuir **29**, 12389–12399 (2013).

[200] W. Humphrey, A. Dalke, and K. Schulten, *VMD: Visual Molecular Dynamics,* Journal of Molecular Graphics **14**, 33–38 (1996).

[201] F. S. Emami, V. Puddu, R. J. Berry, V. Varshney, S. V. Patwardhan, C. C. Perry, and H. Heinz, *Force Field and a Surface Model Database for Silica to Simulate Interfacial Properties in Atomic Resolution,* Chemistry of Materials **26**, 2647–2658 (2014).

[202] I. S. Joung and T. E. Cheatham, *Determination of Alkali and Halide Monovalent Ion Parameters for Use in Explicitly Solvated Biomolecular Simulations,* Journal of Physical Chemistry B **112**, 9020–9041 (2008).

[203] A. Sartbaeva, S. a. Wells, M. M. J. Treacy, and M. F. Thorpe, *The Flexibility Window in Zeolites,* Nature Materials **5**, 962–965 (2006).

[204] P. Schatzberg, *Molecular Diameter of Water from Solubility and Diffusion Measurements,* Journal of Physical Chemistry **71**, 4569–4570 (1967).

[205] T. F. Willems, C. H. Rycroft, M. Kazi, J. C. Meza, and M. Haranczyk, *Algorithms and Tools for High-Throughput Geometry-based Analysis of Crystalline Porous Materials,* Microporous and Mesoporous Materials **149**, 134–141 (2012).

[206] D. A. McQuarrie, *Statistical Mechanics,* 1st ed. (University Science Books, Sausalito, 2000).

[207] Y. Marcus, *Ionic Radii in Aqueous Solutions,* Journal of Solution Chemistry **12**, 271–275 (1983).

[208] L. Tzanis, B. Marler, H. Gies, and J. Patarin, *High-Pressure Water Intrusion Investigation of Pure Silica ITQ-7 Zeolite,* Journal of Physical Chemistry C **117**, 4098–4103 (2013).

[209] T. Humplik, R. Raj, S. C. Maroo, T. Laoui, and E. N. Wang, *Effect of Hydrophilic Defects on Water Transport in MFI Zeolites,* Langmuir **30**, 6446–6453 (2014).

[210] S. H. Jamali, L. Wolff, T. M. Becker, M. de Groen, M. Ramdin, R. Hartkamp, A. Bardow, T. J. H. Vlugt, and O. A. Moultos, *OCTP: A Tool for on-the-Fly Calculation of Transport Properties of Fluids with the Order-n Algorithm in LAMMPS,* Journal of Chemical Information and Modeling **59**, 1290–1294 (2019).

[211] I. Economou, P. Krokidas, V. Michalis, O. Moultos, I. Tsimpanogiannis, and N. Vergadou, *The Role of Molecular Thermodynamics in Developing Industrial Processes and Novel Products That Meet the Needs for a Sustainable Future,* in *The Water-Food-Energy Nexus: Processes, Technologies, and Challenges* (CRC Press, Boca Raton, 2017) Chap. 13, pp. 633–660.

[212] H. Berendsen, D. van der Spoel, and R. van Drunen, *GROMACS: A Message-passing Parallel Molecular Dynamics Implementation,* Computer Physics Communications **91**, 43–56 (1995).

[213] J. C. Phillips, R. Braun, W. Wang, J. Gumbart, E. Tajkhorshid, E. Villa, C. Chipot, R. D. Skeel, L. Kalé, and K. Schulten, *Scalable Molecular Dynamics with NAMD,* Journal of Computational Chemistry **26**, 1781–1802 (2005).

[214] S. H. Jamali, M. Ramdin, T. M. Becker, S. K. Rinwa, W. Buijs, and T. J. H. Vlugt, *Thermodynamic and Transport Properties of Crown-Ethers: Force Field Development and Molecular Simulations,* Journal of Physical Chemistry B **121**, 8367–8376 (2017).

[215] O. A. Moultos, I. N. Tsimpanogiannis, A. Z. Panagiotopoulos, and I. G. Economou, *Self-Diffusion Coefficients of the Binary (H_2O + CO_2) Mixture at High Temperatures and Pressures,* Journal of Chemical Thermodynamics **93**, 424–429 (2016).

[216] H. Jiang, Z. Mester, O. A. Moultos, I. G. Economou, and A. Z. Panagiotopoulos, *Thermodynamic and Transport Properties of H_2O + NaCl from Polarizable Force Fields,* Journal of Chemical Theory and Computation **11**, 3802–3810 (2015).

[217] Sandia National Laboratories, Albuquerque, USA, *LAMMPS Documentation,* `https://lammps.sandia.gov/doc/Manual.html` (accessed 21 November 2019).

[218] S. H. Jamali, *OCTP (On-the-fly Calculation of Transport Properties),* `https://github.com/omoultosEthTuDelft/OCTP` (accessed 1 October 2019).

[219] R. Krishna and J. Wesselingh, *The Maxwell-Stefan Approach to Mass Transfer,* Chemical Engineering Science **52**, 861–911 (1997).

[220] H. A. Kooijman and R. Taylor, *Estimation of Diffusion Coefficients in Multicomponent Liquid Systems,* Industrial & Engineering Chemistry Research **30**, 1217–1222 (1991).

[221] R. Taylor and H. A. Kooijman, *Composition Derivatives of Activity Coefficient Models (For the Estimation of Thermodynamic Factors in Diffusion),* Chemical Engineering Communications **102**, 87–106 (1991).

[222] R. Krishna and J. M. van Baten, *Describing Diffusion in Fluid Mixtures at Elevated Pressures by Combining the Maxwell-Stefan Formulation with an Equation of State,* Chemical Engineering Science **153**, 174–187 (2016).

[223] Wesselingh and R. Krishna, *Mass Transfer in Multicomponent Mixtures*, 1st ed. (VSSD, Delft, 2006).

[224] R. Krishna and J. M. van Baten, *The Darken Relation for Multicomponent Diffusion in Liquid Mixtures of Linear Alkanes: An Investigation Using Molecular Dynamics (MD) Simulations,* Industrial & Engineering Chemistry Research **44**, 6939–6947 (2005).

[225] X. Liu, T. J. H. Vlugt, and A. Bardow, *Maxwell-Stefan Diffusivities in Liquid Mixtures: Using Molecular Dynamics for Testing Model Predictions,* Fluid Phase Equilibria **301**, 110–117 (2011).

[226] X. Liu, S. K. Schnell, J.-M. Simon, D. Bedeaux, S. Kjelstrup, A. Bardow, and T. J. H. Vlugt, *Fick Diffusion Coefficients of Liquid Mixtures Directly Obtained from Equilibrium Molecular Dynamics,* Journal of Physical Chemistry B **115**, 12921–12929 (2011).

[227] X. Liu, T. J. H. Vlugt, and A. Bardow, *Maxwell-Stefan Diffusivities in Binary Mixtures of Ionic Liquids with Dimethyl Sulfoxide (DMSO) and H_2O,* Journal of Physical Chemistry B **115**, 8506–8517 (2011).

[228] X. Liu, A. Bardow, and T. J. H. Vlugt, *Multicomponent Maxwell-Stefan Diffusivities at Infinite Dilution,* Industrial & Engineering Chemistry Research **50**, 4776–4782 (2011).

[229] X. Liu, T. J. H. Vlugt, and A. Bardow, *Predictive Darken Equation for Maxwell-Stefan Diffusivities in Multicomponent Mixtures,* Industrial & Engineering Chemistry Research **50**, 10350–10358 (2011).

[230] D. J. Keffer, C. Y. Gao, and B. J. Edwards, *On the Relationship between Fickian Diffusivities at the Continuum and Molecular Levels,* Journal of Physical Chemistry B **109**, 5279–5288 (2005).

[231] S. P. Balaji, S. K. Schnell, E. S. McGarrity, and T. J. H. Vlugt, *A Direct Method for Calculating Thermodynamic Factors for Liquid Mixtures Using the Permuted Widom Test Particle Insertion Method,* Molecular Physics **111**, 287–296 (2013).

[232] S. P. Balaji, S. K. Schnell, and T. J. H. Vlugt, *Calculating Thermodynamic Factors of Ternary and Multicomponent Mixtures Using the Permuted Widom Test Particle insertion Method,* Theoretical Chemistry Accounts **132**, 1333 (2013).

[233] Y. Zhou and G. H. Miller, *Green-Kubo Formulas for Mutual Diffusion Coefficients in Multicomponent Systems,* Journal of Physical Chemistry **100**, 5516–5524 (1996).

[234] A. Ben-Naim, *Molecular Theory of Solutions*, 1st ed. (Oxford University Press, Oxford, 2006).

[235] N. Dawass, P. Krüger, S. K. Schnell, D. Bedeaux, S. Kjelstrup, J. M. Simon, and T. J. H. Vlugt, *Finite-Size Effects of Kirkwood-Buff Integrals from Molecular Simulations,* Molecular Simulation **7022**, 1–14 (2017).

[236] X. Liu, A. Martín-Calvo, E. McGarrity, S. K. Schnell, S. Calero, J.-M. Simon, D. Bedeaux, S. Kjelstrup, A. Bardow, and T. J. H. Vlugt, *Fick Diffusion Coefficients in Ternary Liquid Systems from Equilibrium Molecular Dynamics Simulations,* Industrial & Engineering Chemistry Research **51**, 10247–10258 (2012).

[237] E. Ruckenstein and I. Shulgin, *Entrainer Effect in Supercritical Mixtures,* Fluid Phase Equilibria **180**, 345–359 (2001).

[238] P. Ganguly and N. F. A. van der Vegt, *Convergence of Sampling Kirkwood-Buff Integrals of Aqueous Solutions with Molecular Dynamics Simulations,* Journal of Chemical Theory and Computation **9**, 1347–1355 (2013).

[239] J. Milzetti, D. Nayar, and N. F. A. van der Vegt, *Convergence of Kirkwood-Buff Integrals of Ideal and Nonideal Aqueous Solutions Using Molecular Dynamics Simulations,* Journal of Physical Chemistry B **122**, 5515–5526 (2018).

[240] D. Borgis, R. Assaraf, B. Rotenberg, and R. Vuilleumier, *Computation of Pair Distribution Functions and Three-dimensional Densities with a Reduced Variance Principle,* Molecular Physics **111**, 3486–3492 (2013).

[241] D. Frenkel, *Personal Communication,* (2019).

[242] M. Mondello and G. S. Grest, *Viscosity Calculations of n-Alkanes by Equilibrium Molecular Dynamics,* Journal of Chemical Physics **106**, 9327 (1997).

[243] D. M. Heyes, *Pressure Tensor of Partial-Charge and Point-Dipole Lattices with Bulk and Surface Geometries,* Physical Review B **49**, 755–764 (1994).

[244] A. P. Thompson, S. J. Plimpton, and W. Mattson, *General Formulation of Pressure and Stress Tensor for Arbitrary Many-Body Interaction Potentials Under periodic Boundary Conditions,* Journal of Chemical Physics **131**, 154107 (2009).

[245] W. E. Meador, G. A. Miner, and L. W. Townsend, *Bulk Viscosity as a Relaxation Parameter: Fact or Fiction?* Physics of Fluids **8**, 258–261 (1996).

[246] B. Sharma and R. Kumar, *Estimation of Bulk Viscosity of Dilute Gases Using a Nonequilibrium Molecular Dynamics Approach,* Physical Review E **100**, 013309 (2019).

[247] K. Meier, A. Laesecke, and S. Kabelac, *Transport Coefficients of the Lennard-Jones Model Fluid. III. Bulk Viscosity,* Journal of Chemical Physics **122**, 014513 (2005).

[248] R. Vogelsang, C. Hoheisel, and G. Ciccotti, *Thermal Conductivity of the Lennard-Jones Liquid by Molecular Dynamics Calculations,* Journal of Chemical Physics **86**, 6371–6375 (1987).

[249] A. Kinaci, J. B. Haskins, and T. Çağın, *On Calculation of Thermal Conductivity from Einstein Relation in Equilibrium Molecular Dynamics,* The Journal of Chemical Physics **137**, 014106 (2012).

[250] G. Pranami and M. H. Lamm, *Estimating Error in Diffusion Coefficients Derived from Molecular Dynamics Simulations,* Journal of Chemical Theory and Computation **11**, 4586–4592 (2015).

[251] W. H. Press, S. A. Teukolsky, W. T. Vetterling, and B. P. Flannery, *Numerical Recipes: The Art of Scientific Computing*, 3rd ed. (Cambridge University Press, Hong Kong, 2007).

[252] D. N. Theodorou and U. W. Suter, *Geometrical Considerations in Model Systems with Periodic Boundaries,* Journal of Chemical Physics **82**, 955–966 (1985).

[253] M. Deserno, *How to Calculate a Three-dimensional $g(r)$ under Periodic Boundary Conditions,* `https://www.cmu.edu/biolphys/deserno/pdf/gr_periodic.pdf` (accessed 21 November 2019).

[254] K. Meier, A. Laesecke, and S. Kabelac, *Transport Coefficients of the Lennard-Jones Model Fluid. II Self-diffusion,* Journal of Chemical Physics **121**, 9526–9535 (2004).

[255] O. A. Moultos, I. N. Tsimpanogiannis, A. Z. Panagiotopoulos, J. P. M. Trusler, and I. G. Economou, *Atomistic Molecular Dynamics Simulations of Carbon Dioxide Diffusivity in n-hexane, n-decane, n-hexadecane, Cyclohexane, and Squalane,* Journal of Physical Chemistry B **120**, 12890–12900 (2016).

[256] V. K. Michalis, O. A. Moultos, I. N. Tsimpanogiannis, and I. G. Economou, *Molecular Dynamics Simulations of the Diffusion Coefficients of Light n-alkanes in Water over a Wide Range of Temperature and Pressure,* Fluid Phase Equilibria **407**, 236–242 (2016).

[257] O. Borodin, G. D. Smith, and H. Kim, *Viscosity of a Room Temperature Ionic Liquid: Predictions from Nonequilibrium and Equilibrium Molecular Dynamics Simulations,* Journal of Physical Chemistry B **113**, 4771–4774 (2009).

[258] K. Meier, A. Laesecke, and S. Kabelac, *Transport Coefficients of the Lennard-Jones Model Fluid. I. Viscosity,* Journal of Chemical Physics **121**, 3671–3687 (2004).

[259] S. H. Jamali, R. Hartkamp, C. Bardas, J. Söhl, T. J. H. Vlugt, and O. A. Moultos, *Shear Viscosity Computed from the Finite-Size Effects of Self-Diffusivity in Equilibrium Molecular Dynamics,* Journal of Chemical Theory and Computation **14**, 5959–5968 (2018).

[260] H. J. C. Berendsen, J. R. Grigera, and T. P. Straatsma, *The Missing Term in Effective Pair Potentials,* Journal of Physical Chemistry **91**, 6269–6271 (1987).

[261] J. R. Errington, P. G. Debenedetti, and S. Torquato, *Quantification of Order in the Lennard-Jones System,* Journal of Chemical Physics **118**, 2256–2263 (2003).

[262] O. A. Moultos, Y. Zhang, I. N. Tsimpanogiannis, I. G. Economou, and E. J. Maginn, *System-Size Corrections for Self-Diffusion Coefficients Calculated from Molecular Dynamics Simulations: The Case of CO_2, n-alkanes, and Poly(Ethylene Glycol) Dimethyl Ethers,* Journal of Chemical Physics **145**, 074109 (2016).

[263] S. H. Jamali, L. Wolff, T. M. Becker, A. Bardow, T. J. H. Vlugt, and O. A. Moultos, *Finite-size Effects of Binary Mutual Diffusion Coefficients from Molecular Dynamics,* Journal of Chemical Theory and Computation **14**, 2667–2677 (2018).

[264] S. K. Das, M. E. Fisher, J. V. Sengers, J. Horbach, and K. Binder, *Critical Dynamics in a Binary Fluid: Simulations and Finite-size Scaling,* Physical Review Letters **97**, 025702 (2006).

[265] R. Krishna and J. M. van Baten, *An Investigation of the Characteristics of Maxwell-Stefan Diffusivities of Binary Mixtures in Silica Nanopores,* Chemical Engineering Science **64**, 870–882 (2009).

[266] R. Krishna and J. M. van Baten, *Unified Maxwell-Stefan Dscription of Binary Mixture Diffusion in Micro- and Meso-porous Materials,* Chemical Engineering Science **64**, 3159–3178 (2009).

[267] R. Krishna and J. M. van Baten, *Highlighting Pitfalls in the Maxwell-Stefan Modeling of Water-Alcohol Mixture Permeation Across Pervaporation Membranes,* Journal of Membrane Science **360**, 476–482 (2010).

[268] R. Krishna, *The Maxwell-Stefan Description of Mixture Diffusion in Nanoporous Crystalline Materials,* Microporous and Mesoporous Materials **185**, 30–50 (2014).

[269] R. Krishna, *Using the Maxwell-Stefan Formulation for Highlighting the Influence of Interspecies (1-2) Friction on Binary Mixture Permeation Across Microporous and Polymeric Membranes,* Journal of Membrane Science **540**, 261–276 (2017).

[270] M. Schoen and C. Hoheisel, *The Mutual Diffusion Coefficient D_{12} in Binary Liquid Model Mixtures. Molecular Dynamics Calculations Based on Lennard-Jones (12-6) Potentials,* Molecular Physics **52**, 33–56 (1984).

[271] M. Schoen and C. Hoheisel, *The Mutual Diffusion Coefficient D_{12} in Liquid Model Mixtures A Molecular Dynamics Study Based on Lennard-Jones (12-6) Potentials,* Molecular Physics **52**, 1029–1042 (1984).

[272] H. Weingärtner, *The Microscopic Basis of Self Diffusion - Mutual Diffusion Relationships in Binary Liquid Mixtures,* Berichte der Bunsengesellschaft für physikalische Chemie **94**, 358–364 (1990).

[273] C. D'Agostino, J. Stephens, J. Parkinson, M. Mantle, L. Gladden, and G. Moggridge, *Prediction of the Mutual Diffusivity in Acetone-chloroform Liquid Mixtures from the Tracer Diffusion Coefficients,* Chemical Engineering Science **95**, 43–47 (2013).

[274] T. Allie-Ebrahim, Q. Zhu, P. Bräuer, G. D. Moggridge, and C. D'Agostino, *Maxwell-Stefan diffusion Coefficient Estimation for Ternary Systems: An Ideal Ternary Alcohol system,* Physical Chemistry Chemical Physics **19**, 16071–16077 (2017).

[275] M. Fisher and M. Barber, *Scaling Theory for Finite-size Effects in the Critical Region,* Physical Review Letters **28**, 1516–1519 (1972).

[276] R. Hilfer and N. B. Wilding, *Are Critical Finite-size Scaling Functions Calculable from Knowledge of an Approriate Critical Exponent?* Journal of Physics A: Mathematical and General **28**, L281 (1995).

[277] K. Binder, *Theory of First-order Phase Transitions,* Reports on Progress in Physics **50**, 783–859 (1987).

[278] N. B. Wilding, *Critical-point and Coexistence-curve Properties of the Lennard-Jones Fluid: A Finite-size Scaling Study,* Physical Review E **52**, 602–611 (1995).

[279] A. D. Bruce and N. B. Wilding, *Critical-point Finite-size Scaling in the Microcanonical Ensemble,* Physical Review E **60**, 3748–3760 (1999).

[280] E. Guazzelli and J. F. Morris, *A Physical Introduction to Suspension Dynamics*, 1st ed. (Cambridge University Press, Cambridge, 2012).

[281] A. Botan, V. Marry, and B. Rotenberg, *Diffusion in Bulk Liquids: Finite-size Effects in Anisotropic Systems,* Molecular Physics **113**, 2674–2679 (2015).

[282] M. Vögele and G. Hummer, *Divergent Diffusion Coefficients in Simulations of Fluids and Lipid Membranes,* Journal of Physical Chemistry B **120**, 8722–8732 (2016).

[283] X. Yang, H. Zhang, L. Li, and X. Ji, *Corrections of the Periodic Boundary Conditions with Rectangular Simulation Boxes on the Diffusion Coefficient, General Aspects,* Molecular Simulation **43**, 1423–1429 (2017).

[284] P. Simonnin, B. Noetinger, C. Nieto-Draghi, V. Marry, and B. Rotenberg, *Diffusion under Confinement: Hydrodynamic Finite-size Effects in Simulation,* Journal of Chemical Theory and Computation **13**, 2881–2889 (2017).

[285] O. A. Moultos, G. A. Orozco, I. N. Tsimpanogiannis, A. Z. Panagiotopoulos, and I. G. Economou, *Atomistic Molecular Dynamics Simulations of H_2O Diffusivity in Liquid and Supercritical CO_2,* Molecular Physics **113**, 2805–2814 (2015).

[286] L. Martínez, R. Andrade, E. G. Birgin, and J. M. Martínez, *PACKMOL: A Package for Building Initial Configurations for Molecular Dynamics Simulations,* Journal of Computational Chemistry **30**, 2157–2164 (2009).

[287] N. R. Tummala and A. Striolo, *Hydrogen-bond Dynamics for Water Confined in Carbon Tetrachloride-acetone Mixtures,* Journal of Physical Chemistry B **112**, 10675–10683 (2008).

[288] X. Wang, Y. Chi, and T. Mu, *A Review on the Transport Properties of Ionic Liquids,* Journal of Molecular Liquids **193**, 262–266 (2014).

[289] Y. Zhang, L. Xue, F. Khabaz, R. Doerfler, E. L. Quitevis, R. Khare, and E. J. Maginn, *Molecular Topology and Local Dynamics Govern the Viscosity of Imidazolium-Based Ionic Liquids,* Journal of Physical Chemistry B **119**, 14934–14944 (2015).

[290] E. L. Smith, A. P. Abbott, and K. S. Ryder, *Deep Eutectic Solvents (DESs) and Their Applications,* Chemical Reviews **114**, 11060–11082 (2014).

[291] I. N. Tsimpanogiannis, O. A. Moultos, L. F. M. Franco, M. B. M. Spera, M. Erdös, and I. G. Economou, *Self-diffusion Coefficient of Bulk and Confined Water: A Critical Review of Classical Molecular Simulation Studies,* Molecular Simulation **45**, 425–453 (2019).

[292] D. Spångberg and K. Hermansson, *Effective Three-body Potentials for Li^+ (aq) and Mg^{2+} (aq),* Journal of Chemical Physics **119**, 7263–7281 (2003).

[293] T. D. Kühne, M. Krack, and M. Parrinello, *Static and Dynamical Properties of Liquid Water from First Principles by a Novel Car-Parrinello-like Approach,* Journal of Chemical Theory and Computation **5**, 235–241 (2009).

[294] S. Tazi, A. Botan, M. Salanne, V. Marry, P. Turq, and B. Rotenberg, *Diffusion Coefficient and Shear Viscosity of Rigid Water Models,* Journal of Physics: Condensed Matter **24**, 284117 (2012).

[295] P. Tröster, K. Lorenzen, and P. Tavan, *Polarizable Six-point Water Models from Computational and Empirical Optimization,* Journal of Physical Chemistry B **118**, 1589–1602 (2014).

[296] M. Ramdin, T. W. de Loos, and T. J. H. Vlugt, *State-of-the-Art of CO_2 Capture with Ionic Liquids,* Industrial & Engineering Chemistry Research **51**, 8149–8177 (2012).

[297] A. Uma Maheswari and K. Palanivelu, *Carbon Dioxide Capture and Utilization by Alkanolamines in Deep Eutectic Solvent Medium,* Industrial & Engineering Chemistry Research **54**, 11383–11392 (2015).

[298] B. Wang, J. Kuo, S. C. Bae, and S. Granick, *When Brownian Diffusion is not Gaussian,* Nature Materials **11**, 481–485 (2012).

[299] Y. Zhang and E. J. Maginn, *Direct Correlation between Ionic Liquid Transport Properties and Ion Pair Lifetimes: A Molecular Dynamics Study,* Journal of Physical Chemistry Letters **6**, 700–705 (2015).

[300] T. Ishida and H. Shirota, *Dicationic versus Monocationic Ionic Liquids: Distinctive Ionic Dynamics and Dynamical Heterogeneity,* Journal of Physical Chemistry B **117**, 1136–1150 (2013).

[301] Z. Ren, A. S. Ivanova, D. Couchot-Vore, and S. Garrett-Roe, *Ultrafast Structure and Dynamics in Ionic Liquids: 2D-IR Spectroscopy Probes the Molecular Origin of Viscosity,* Journal of Physical Chemistry Letters **5**, 1541–1546 (2014).

[302] M. A. Gonzaélez and J. L. F. Abascal, *The Shear Viscosity of Rigid Water Models,* Journal of Chemical Physics **132**, 096101 (2010).

[303] C. Vega and J. L. F. Abascal, *Simulating Water with Rigid Non-polarizable Models: A General Perspective,* Physical Chemistry Chemical Physics **13**, 19663 (2011).

[304] G. Guevara-Carrion, J. Vrabec, and H. Hasse, *Prediction of Self-diffusion Coefficient and Shear Viscosity of Water and its Binary Mixtures with Methanol and Ethanol by Molecular Simulation,* Journal of Chemical Physics **134**, 074508 (2011).

[305] M. J. Abraham, T. Murtola, R. Schulz, S. Páll, J. C. Smith, B. Hess, and E. Lindah, *Gromacs: High Performance Molecular Simulations through Multi-level Parallelism from Laptops to Supercomputers,* SoftwareX **1-2**, 19–25 (2015).

[306] R. Salomon-Ferrer, A. W. Götz, D. Poole, S. Le Grand, and R. C. Walker, *Routine Microsecond Molecular Dynamics Simulations with AMBER on GPUs. 2. Explicit Solvent Particle Mesh Ewald,* Journal of Chemical Theory and Computation **9**, 3878–3888 (2013).

[307] D. M. Heyes, M. J. Cass, J. G. Powles, and W. A. B. Evans, *Self-diffusion Coefficient of the Hard-sphere Fluid: System Size Dependence and Empirical Correlations,* Journal of Physical Chemistry B **111**, 1455–1464 (2007).

[308] S. H. Jamali, T. van Westen, O. A. Moultos, and T. J. H. Vlugt, *Optimizing Nonbonded Interactions of the OPLS Force Field for Aqueous Solutions of Carbohydrates: How to Capture Both Thermodynamics and Dynamics,* Journal of Chemical Theory and Computation **14**, 6690–6700 (2018).

[309] A. Varki, R. D. Cummings, J. D. Esko, P. Stanley, G. W. Hart, M. Aebi, A. G. Darvill, T. Kinoshita, N. H. Packer, J. H. Prestegard, R. L. Schnaar, and P. H. Seeberger, eds., *Essentials of Glycobiology*, 3rd ed. (Cold Spring Harbor Laboratory Press, New York, 2017).

[310] O. Fennema and W. D. Powrie, *Fundamentals of Low-temperature Food Preservation,* (Academic Press, 1964) pp. 219–347.

[311] J. Lee and S. Timasheff, *The Stabillization of Proteins by Sucrose,* Journal of Biological Chemistry **256**, 7193–7201 (1981).

[312] J. O. Karlsson and M. Toner, *Long-term Storage of Tissues by Cryopreservation: Critical Issues,* Biomaterials **17**, 243–256 (1996).

[313] J. G. Day and G. N. Stacey, *Cryopreservationand Freeze-drying Protocols*, 2nd ed. (Humana Press, Totowa, 2007).

[314] M. S. Rahman, *Handbook of Food Preservation*, 2nd ed. (CRC Press, Boca Raton, 2007).

[315] Y. H. Roos and S. Drusch, *Phase Transitions in Foods*, 2nd ed. (Academic Press, Oxford, 2015).

[316] L. N. Csonka, *Physiological and Genetic Responses of Bacteria to Osmotic Stress,* Microbiological reviews **53**, 121–47 (1989).

[317] W. Vollmer, D. Blanot, and M. A. de Pedro, *Peptidoglycan Structure and Architecture,* FEMS Microbiology Reviews **32**, 149–167 (2008).

[318] W. Vollmer and U. Bertsche, *Murein (Peptidoglycan) Structure, Architecture and Biosynthesis in Escherichia Coli,* Biochimica et Biophysica Acta - Biomembranes **1778**, 1714–1734 (2008).

[319] L. Sapir and D. Harries, *Linking Trehalose Self-association with Binary Aqueous Solution Equation of State,* Journal of Physical Chemistry B **115**, 624–634 (2011).

[320] M. L. S. Batista, G. Pérez-Sánchez, J. R. B. Gomes, J. A. P. Coutinho, and E. J. Maginn, *Evaluation of the GROMOS 56A CARBO Force Field for the Calculation of Structural, Volumetric, and Dynamic Properties of Aqueous Glucose Systems,* Journal of Physical Chemistry B **119**, 15310–15319 (2015).

[321] W. K. Lay, M. S. Miller, and A. H. Elcock, *Optimizing Solute-solute Interactions in the GLYCAM06 and CHARMM36 Carbohydrate Force Fields Using Osmotic Pressure Measurements,* Journal of Chemical Theory and Computation **12**, 1401–1407 (2016).

[322] P. S. Schmalhorst, F. Deluweit, R. Scherrers, C.-P. Heisenberg, and M. Sikora, *Overcoming the Limitations of the MARTINI Force Field in Simulations of Polysaccharides,* Journal of Chemical Theory and Computation **13**, 5039–5053 (2017).

[323] O. Guvench, E. Hatcher, R. M. Venable, R. W. Pastor, and A. D. MacKerell, *CHARMM Additive All-atom Force Field for Glycosidic Linkages between Hexopyranoses,* Journal of Chemical Theory and Computation **5**, 2353–2370 (2009).

[324] E. P. Raman, O. Guvench, and A. D. MacKerell, *CHARMM Additive All-atom Force Field for Glycosidic Linkages in Carbohydrates Involving Furanoses,* Journal of Physical Chemistry B **114**, 12981–12994 (2010).

[325] K. N. Kirschner, A. B. Yongye, S. M. Tschampel, J. González-Outeiriño, C. R. Daniels, B. L. Foley, and R. J. Woods, *GLYCAM06: A Generalizable Biomolecular Force Field. Carbohydrates,* Journal of Computational Chemistry **29**, 622–655 (2008).

[326] R. D. Lins and P. H. Hünenberger, *A New GROMOS Force Field for Hexopyranose-based Carbohydrates,* Journal of Computational Chemistry **26**, 1400–1412 (2005).

[327] D. Kony, W. Damm, S. Stoll, and W. F. van Gunsteren, *An Improved OPLS-AA Force Field for Carbohydrates,* Journal of Computational Chemistry **23**, 1416–1429 (2002).

[328] C. A. Lopez, A. J. Rzepiela, A. H. de Vries, L. Dijkhuizen, P. H. Hunenberger, and S. J. Marrink, *Martini Coarse-grained Force Field: Extension to Carbohydrates,* Journal of Chemical Theory and Computation **5**, 3195–3210 (2009).

[329] D. Dubbeldam, S. Calero, and T. J. H. Vlugt, *iRASPA: GPU-accelerated Visualization Software for Materials Scientists,* Molecular Simulation **44**, 653–676 (2018).

[330] F. E. Young and F. T. Jones, *Sucrose Hydrates. The Sucrose-water Phase Diagram.* Journal of Physical and Colloid Chemistry **53**, 1334–1350 (1949).

[331] F. E. Young, *D-glucose-water Phase Diagram,* Journal of Physical Chemistry **61**, 616–619 (1957).

[332] Y. Wu, H. L. Tepper, and G. A. Voth, *Flexible Simple Point-charge Water Model with Improved Liquid-state Properties,* Journal of Chemical Physics **124**, 024503 (2006).

[333] M. Asadi, *Beet-sugar Handbook*, 1st ed. (John Wiley & Sons, Hoboken, 2007).

[334] M. Rampp, C. Buttersack, and H.-D. Lüdemann, *c, T -Dependence of the Viscosity and the Self-diffusion Coefficients in Some Aqueous Carbohydrate Solutions,* Carbohydrate Research **328**, 561–572 (2000).

[335] R. A. Robinson and R. H. Stokes, *Activity Coefficients in Aqueous Solutions of Sucrose, Mannitol and Their Mixtures at 25°,* Journal of Physical Chemistry **65**, 1954–1958 (1961).

[336] M. Starzak and M. Mathlouthi, *Temperature Dependence of Water Activity in Aqueous Solutions of Sucrose,* Food Chemistry **96**, 346–370 (2006).

[337] A. V. Onufriev and S. Izadi, *Water Models for Biomolecular Simulations,* Wiley Interdisciplinary Reviews: Computational Molecular Science **8**, e1347 (2018).

[338] Y. Song and L. L. Dai, *The Shear Viscosities of Common Water Models by Non-equilibrium Molecular Dynamics Simulations,* Molecular Simulation **36**, 560–567 (2010).

[339] J. Medina, R. Prosmiti, P. Villarreal, G. Delgado-Barrio, G. Winter, B. González, J. Alemán, and C. Collado, *Molecular Dynamics Simulations of Rigid and Flexible Water Models: Temperature Dependence of Viscosity,* Chemical Physics **388**, 9–18 (2011).

[340] J. L. F. Abascal and C. Vega, *A general purpose model for the condensed phases of water: TIP4P/2005,* Journal of Chemical Physics **123**, 234505 (2005).

[341] S. W. Rick, *A Reoptimization of the Five-site Water Potential (TIP5P) for use with Ewald Sums,* Journal of Chemical Physics **120**, 6085–6093 (2004).

[342] H. Jiang, O. A. Moultos, I. G. Economou, and A. Z. Panagiotopoulos, *Hydrogen-bonding Polarizable Intermolecular Potential Model for Water,* Journal of Physical Chemistry B **120**, 12358–12370 (2016).

[343] Y. Mao and Y. Zhang, *Thermal Conductivity, Shear Viscosity and Specific Heat of Rigid Water Models,* Chemical Physics Letters **542**, 37–41 (2012).

[344] M. Mathlouthi and P. Reiser, eds., *Sucrose Properties and Applications*, 1st ed. (Springer US, Boston, MA, 1995).

[345] A. F. Fucaloro, Y. Pu, K. Cha, A. Williams, and K. Conrad, *Partial Molar Volumes and Refractions of Aqueous Solutions of Fructose, Glucose, Mannose, and Sucrose at 15.00, 20.00, and 25.00 °C,* Journal of Solution Chemistry **36**, 61–80 (2007).

[346] D. Girlich, H. D. Lüdemann, C. Buttersack, and K. Buchholz, *c, T-Dependence of the Self Diffusion in Concentrated Aqueous Sucrose Solutions,* Zeitschrift fur Naturforschung - Section C Journal of Biosciences **49**, 258–264 (1994).

[347] P. N. Henrion, *Diffusion in the Sucrose + Water System,* Transactions of the Faraday Society **60**, 72 (1964).

[348] R. R. Irani and A. W. Adamson, *Transport Processes in Binary Liquid Systems,* Journal of Physical Chemistry **62**, 1517–1521 (1958).

[349] Y. Nishida, H. Ohrui, and H. Meguro, ^{1}*H-NMR Studies of (6r)- and (6s)-deuterated D-hexoses: Assignment of the Preferred Rotamers about C5-C6 bond of D-glucose and D-galactose Derivatives in Solutions,* Tetrahedron Letters **25**, 1575–1578 (1984).

[350] Y. Nishida, H. Hori, H. Ohrui, and H. Meguro, ^{1}*H NMR Analyses of Rotameric Distribution of C5-C6 bonds of D-glucopyranoses in Solution,* Journal of Carbohydrate Chemistry **7**, 239–250 (1988).

[351] J. F. Comesaña, J. J. Otero, E. García, and A. Correa, *Densities and Viscosities of Ternary Systems of Water + Glucose + Sodium Chloride at Several Temperatures,* Journal of Chemical & Engineering Data **48**, 362–366 (2003).

[352] M. Castaldi, G. D'Errico, L. Paduano, and V. Vitagliano, *Transport Properties of the Binary System Glucose-water at 25 °C. A Velocity Correlation Study,* Journal of Chemical & Engineering Data **43**, 653–657 (1998).

[353] R. H. Stokes and R. A. Robinson, *Interactions in Aqueous Nonelectrolyte Solutions. I. Solute-solvent Equilibria,* Journal of Physical Chemistry **70**, 2126–2131 (1966).

[354] K. Miyajima, M. Sawada, and M. Nakagaki, *Studies on Aqueous Solutions of Saccharides. I. Activity Coefficients of Monosaccharides in Aqueous Solutions at 25 °C,* Bulletin of the Chemical Society of Japan **56**, 1620–1623 (1983).

[355] V. Telis, J. Telis-Romero, H. Mazzotti, and A. Gabas, *Viscosity of Aqueous Carbohydrate Solutions at Different Temperatures and Concentrations,* International Journal of Food Properties **10**, 185–195 (2007).

[356] C. Talon, L. J. Smith, J. W. Brady, B. A. Lewis, J. R. D. Copley, D. L. Price, and M.-L. Saboungi, *Dynamics of Water Molecules in Glucose Solutions,* Journal of Physical Chemistry B **108**, 5120–5126 (2004).

[357] J. K. Gladden and M. Dole, *Diffusion in Supersaturated Solutions. II. Glucose Solutions,* Journal of the American Chemical Society **75**, 3900–3904 (1953).

[358] I. M. J. J. van de Ven-Lucassen and P. J. A. M. Kerkhof, *Diffusion Coefficients of Ternary Mixtures of Water, Glucose, and Dilute Ethanol, Methanol, or Acetone by the Taylor Dispersion Method,* Journal of Chemical & Engineering Data **44**, 93–97 (1999).

[359] C. J. Pedersen, *Cyclic Polyethers and their Complexes with Metal Salts,* Journal of the American Chemical Society **89**, 7017–7036 (1967).

[360] A. Swidan and C. L. B. Macdonald, *Polyether Complexes of Groups 13 and 14,* Chemical Society Reviews **45**, 3883–3915 (2016).

[361] R. Mohammadzadeh Kakhki, *Application of Crown Ethers as Stationary Phase in the Chromatographic Methods,* Journal of Inclusion Phenomena and Macrocyclic Chemistry **75**, 11–22 (2013).

[362] F. Arnaud-Neu, R. Delgado, and S. Chaves, *Critical Evaluation of Stability Constants and Thermodynamic Functions of Metal Complexes of Crown Ethers (IUPAC technical report),* Pure and Applied Chemistry **75**, 71–102 (2003).

[363] M. Yoshio and H. Noguchi, *Crown Ethers for Chemical Analysis: A Review,* Analytical Letters **15**, 1197–1276 (1982).

[364] G. W. Gokel, W. M. Leevy, and M. E. Weber, *Crown Ethers: Sensors for Ions and Molecular Scaffolds for Materials and Biological Models,* Chemical Reviews **104**, 2723–2750 (2004).

[365] N. Giri, M. G. Del Pópolo, G. Melaugh, R. L. Greenaway, K. Rätzke, T. Koschine, L. Pison, M. F. C. Gomes, A. I. Cooper, and S. L. James, *Liquids with Permanent Porosity,* Nature **527**, 216–220 (2015).

[366] S. L. James, *The Dam Bursts for Porous Liquids,* Advanced Materials **28**, 5712–5716 (2016).

[367] S. Das, P. Heasman, T. Ben, and S. Qiu, *Porous Organic Materials: Strategic Design and Structure-Function Correlation,* Chemical Reviews **117**, 1515–1563 (2017).

[368] N. O'Reilly, N. Giri, and S. L. James, *Porous Liquids,* Chemistry - A European Journal **13**, 3020–3025 (2007).

[369] M. Mastalerz, *Liquefied Molecular Holes,* Nature **527**, 174–175 (2015).

[370] J. Zhang, S.-H. Chai, Z.-A. Qiao, S. M. Mahurin, J. Chen, Y. Fang, S. Wan, K. Nelson, P. Zhang, and S. Dai, *Porous Liquids: A Promising Class of Media for Gas Separation,* Angewandte Chemie International Edition **54**, 932–936 (2015).

[371] F. Zhang, F. Yang, J. Huang, B. G. Sumpter, and R. Qiao, *Thermodynamics and Kinetics of Gas Storage in Porous Liquids,* Journal of Physical Chemistry B **120**, 7195–7200 (2016).

[372] R. L. Greenaway, D. Holden, E. G. B. Eden, A. Stephenson, C. W. Yong, M. J. Bennison, T. Hasell, M. E. Briggs, S. L. James, and A. I. Cooper, *Understanding Gas Capacity, Guest Selectivity, and Diffusion in Porous Liquids,* Chemical Science **8**, 2640–2651 (2017).

[373] A. I. Cooper, *Porous Molecular Solids and Liquids,* ACS Central Science **3**, 544–553 (2017).

[374] F. Zhang, Y. He, J. Huang, B. G. Sumpter, and R. Qiao, *Multicomponent Gas Storage in Organic Cage Molecules,* Journal of Physical Chemistry C **121**, 12426–12433 (2017).

[375] J. van Eerden, S. Harkema, and D. Feil, *Molecular Dynamics of 18-crown-6 Complexes with Alkali-metal Cations: Calculation of Relative Free Energies of Complexation,* Journal of Physical Chemistry **92**, 5076–5079 (1988).

[376] P. D. J. Grootenhuis and P. A. Kollman, *Molecular Mechanics and Dynamics Studies of Crown Ether-cation Interactions: Free Energy Calculations on the Cation Selectivity of Dibenzo-18-crown-6 and Dibenzo-30-crown-10,* Journal of the American Chemical Society **111**, 2152–2158 (1989).

[377] L. X. Dang and P. A. Kollman, *Free Energy of Association of the 18-crown-6: K^+ Complex in Water: A Molecular Dynamics Simulation,* Journal of the American Chemical Society **112**, 5716–5720 (1990).

[378] G. Wipff, *Molecular Modeling Studies on Molecular Recognition: Crown Ethers, Cryptands and Cryptates. From Static Models in vacuo to Dynamical Models in Solution,* Journal of Coordination Chemistry **27**, 7–37 (1992).

[379] P. Guilbaud and G. Wipff, *Hydration of Uranyl (UO_2^{2+}) Cation and its Nitrate Ion and 18-crown-6 Adducts Studied by Molecular Dynamics Simulations,* Journal of Physical Chemistry **97**, 5685–5692 (1993).

[380] L. Troxler and G. Wipff, *Conformation and Dynamics of 18-crown-6, Cryptand 222, and Their Cation Complexes in Acetonitrile Studied by Molecular Dynamics Simulations,* Journal of the American Chemical Society **116**, 1468–1480 (1994).

[381] L. X. Dang, *Mechanism and Thermodynamics of Ion Selectivity in Aqueous Solutions of 18-crown-6 Ether: A Molecular Dynamics Study,* Journal of the American Chemical Society **117**, 6954–6960 (1995).

[382] L. X. Dang and P. A. Kollman, *Free Energy of Association of the K^+:18-crown-6 Complex in Water: A New Molecular Dynamics Study,* The Journal of Physical Chemistry **99**, 55–58 (1995).

[383] M. C. Zwier, J. W. Kaus, and L. T. Chong, *Efficient Explicit-solvent Molecular Dynamics Simulations of Molecular Association Kinetics: Methane/methane, Na^+/Cl^- , Methane/benzene, and K^+/18-crown-6 Ether,* Journal of Chemical Theory and Computation **7**, 1189–1197 (2011).

[384] M. Billeter, A. E. Howard, I. D. Kuntz, and P. A. Kollman, *A New Technique to Calculate Low-energy Conformations of Cyclic Molecules Utilizing the Ellipsoid Algorithm and Molecular Dynamics: Application to 18-crown-6,* Journal of the American Chemical Society **110**, 8385–8391 (1988).

[385] J. van Eerden, S. Harkema, and D. Feil, *Molecular-Dynamics Simulation of Crystalline 18-crown-6: Thermal Shortening of Covalent Bonds,* Acta Crystallographica Section B Structural Science **46**, 222–229 (1990).

[386] M. S. Shah, M. Tsapatsis, and J. I. Siepmann, *Development of the Transferable Potentials for Phase Equilibria Model for Hydrogen Sulfide,* Journal of Physical Chemistry B **119**, 7041–7052 (2015).

[387] Wavefunction Inc., Irvine, USA, *Spartan'14,* `https://www.wavefun.com` (accessed 21 November 2019).

[388] MathWorks Inc., Natick, USA, *Optimization Toolbox User's Guide,* `https://www.mathworks.com/products/optimization.html` (accessed 21 November 2019).

[389] D. Dubbeldam, S. Calero, D. E. Ellis, and R. Q. Snurr, *RASPA: Molecular Simulation Software for Adsorption and Diffusion in Flexible Nanoporous Materials,* Molecular Simulation **42**, 81–101 (2016).

[390] D. Dubbeldam, A. Torres-Knoop, and K. S. Walton, *On the Inner Workings of Monte Carlo Codes,* Molecular Simulation **39**, 1253–1292 (2013).

[391] R. T. Cygan, V. N. Romanov, and E. M. Myshakin, *Molecular Simulation of Carbon Dioxide Capture by Montmorillonite Using an Accurate and Flexible Force Field,* Journal of Physical Chemistry C **116**, 13079–13091 (2012).

[392] W. Shi and E. J. Maginn, *Continuous Fractional Component Monte Carlo: An Adaptive Biasing Method for Open System Atomistic Simulations,* Journal of Chemical Theory and Computation **3**, 1451–1463 (2007).

[393] W. Shi and E. J. Maginn, *Molecular Simulation and Regular Solution Theory Modeling of Pure and Mixed Gas Absorption in the Ionic Liquid 1-n-hexyl-3-methylimidazolium Bis(Trifluoromethylsulfonyl)amide ([hmim][Tf_2N]),* Journal of Physical Chemistry B **112**, 16710–16720 (2008).

[394] W. Shi, D. C. Sorescu, D. R. Luebke, M. J. Keller, and S. Wickramanayake, *Molecular Simulations and Experimental Studies of Solubility and Diffusivity for Pure and Mixed Gases of H_2, CO_2, and Ar Absorbed in the Ionic Liquid 1-n-hexyl-3-methylimidazolium Bis(Trifluoromethylsulfonyl)amide ([hmim][Tf_2N]),* Journal of Physical Chemistry B **114**, 6531–6541 (2010).

[395] M. Ramdin, S. P. Balaji, J. M. Vicent-Luna, J. J. Gutiérrez-Sevillano, S. Calero, T. W. de Loos, and T. J. H. Vlugt, *Solubility of the Precombustion Gases CO_2, CH_4, CO, H_2, N_2, and H_2S in the Ionic Liquid [bmim][Tf_2N] from Monte Carlo Simulations,* Journal of Physical Chemistry C **118**, 23599–23604 (2014).

[396] M. Ramdin, Q. Chen, S. P. Balaji, J. M. Vicent-Luna, A. Torres-Knoop, D. Dubbeldam, S. Calero, T. W. de Loos, and T. J. H. Vlugt, *Solubilities of CO_2, CH_4, C_2H_6, and SO_2 in Ionic Liquids and Selexol from Monte Carlo Simulations,* Journal of Computational Science **15**, 74–80 (2016).

[397] M. Ramdin, S. P. Balaji, J. M. Vicent-Luna, A. Torres-Knoop, Q. Chen, D. Dubbeldam, S. Calero, T. W. de Loos, and T. J. H. Vlugt, *Computing Bubble-points of CO_2/CH_4 Gas Mixtures in Ionic Liquids from Monte Carlo Simulations,* Fluid Phase Equilibria **4**, 4–11 (2015).

[398] S. H. Jamali, M. Ramdin, T. M. Becker, A. Torres-Knoop, D. Dubbeldam, W. Buijs, and T. J. H. Vlugt, *Solubility of Sulfur Compounds in Commercial Physical Solvents and an Ionic Liquid from Monte Carlo Simulations,* Fluid Phase Equilibria **433**, 50–55 (2017).

[399] A. L. Kohl and R. Nielsen, *Gas Purification*, 5th ed. (Gulf Professional Publishing, Houston, 1997).

[400] J. Li, M. Mundhwa, and A. Henni, *Volumetric Properties, Viscosities, Refractive Indices, and Surface Tensions for Aqueous Genosorb 1753 Solutions,* Journal of Chemical & Engineering Data **52**, 955–958 (2007).

[401] H. Vogel and A. Weiss, *Transport Properties of Liquids I. Self-diffusion, Viscosity and Density of Nearly Spherical and Disk Like Molecules in the Pure Liquid Phase,* Berichte der Bunsengesellschaft für physikalische Chemie **85**, 539–548 (1981).

[402] J. M. Prausnitz, R. N. Lichtenthaler, and E. G. de Azevedo, *Molecular Thermodynamics of Fluid-phase Equilibria* (Prentice Hall, New Jersey, 1998).

[403] R. Linford and D. Thornhill, *Solubilities of a Gas in a Crown Ether,* Journal of Chemical Thermodynamics **17**, 701–702 (1985).

[404] A. Henni, P. Tontiwachwuthikul, and A. Chakma, *Solubilities of Carbon Dioxide in Polyethylene Glycol Ethers,* Canadian Journal of Chemical Engineering **83**, 358–361 (2008).

[405] A. V. Rayer, A. Henni, and P. Tontiwachwuthikul, *High Pressure Physical Solubility of Carbon Dioxide (CO_2) in Mixed Polyethylene Glycol Dimethyl Ethers (Genosorb 1753),* Canadian Journal of Chemical Engineering **90**, 576–583 (2012).

[406] I. Gainar and G. Anitescu, *The Solubility of CO_2, N_2 and H_2 in a Mixture of Dimethylether Polyethylene Glycols at High Pressures,* Fluid Phase Equilibria **109**, 281–289 (1995).

[407] A. Henni, P. Tontiwachwuthikul, and A. Chakma, *Solubility Study of Methane and Ethane in Promising Physical Solvents for Natural Gas Sweetening Operations,* Journal of Chemical & Engineering Data **51**, 64–67 (2006).

SUMMARY

Knowledge on transport properties of fluids is of great interest for process and product design development in the chemical, food, pharmaceutical, and biotechnological industry. In the past few decades, molecular simulation has become a powerful tool to calculate these properties. In this context, Molecular Dynamics (MD) is important for the calculation of transport properties of complex systems, where currently available models are not valid, or at extreme conditions at which performing an experiment is dangerous or not feasible. MD simulations provide detailed information about the dynamics of the system at the molecular level. In this thesis, the aim is to investigate the computation of transport properties using force field-based MD simulations. To this end, this thesis consists of two parts. In the first part (chapters 2-5), the methodologies to compute transport properties from equilibrium Molecular Dynamics (EMD) and non-equilibrium Molecular Dynamics (NEMD) simulations are discussed and applied to investigate finite-size effects of transport properties. In the second part (chapters 6 and 7), force field improvement is the focus of study as the used force fields determine the accuracy of computed properties from MD simulations.

The focus of this thesis is on the computation of transport properties in EMD simulations. However, NEMD methods are extensively used in molecular simulation studies due to their advantages in some specific cases. An important example of these cases is the study of diffusion of fluids through a nanoporous material, e.g., reverse osmosis desalination. Reverse osmosis constitutes a large portion of currently operating commercial water desalination systems. Using membranes with large water fluxes while maintaining high salt rejection is of central importance for decreasing the associated energy consumption and costs. The ultrathin-film nature of zeolite nanosheets and their versatile pore structures provide great opportunities for desalination. In chapter 2, NEMD simulations were carried out to systematically study zeolites as reverse osmosis membranes and establish fundamental structure-performance relationships. It was observed that zeolite nanosheets can achieve a high salt rejection rate close to 100%, while allowing nearly two orders of magnitude higher water permeability than currently available membranes. The effects of the pore density, inclusion of

cages, and the free energy barrier on the water permeability and salt rejection are unraveled, leading to important insight into the rational design of novel zeolite membranes.

To study transport properties from EMD simulations, having a tool to efficiently and consistently sample properties of the system is necessary. In chapter 3, a new plugin for LAMMPS is presented for On-the-fly Computation of Transport Properties (OCTP). This plugin computes the self- and Maxwell-Stefan (MS) diffusivities, bulk and shear viscosities, and thermal conductivities of pure fluids and mixtures in a single simulation. OCTP is the first implementation in LAMMPS that uses the Einstein relations combined with the order-n algorithm for the efficient sampling of dynamic variables. In this chapter, the calculation of transport properties from EMD simulations is described in detail. To demonstrate the efficiency of the new plugin, the transport properties of an equimolar mixture of water-methanol were computed at 298 K and 1 bar. Finite-size effects of transport properties of a Lennard-Jones (LJ) fluid close to the critical point are studied. These results indicate that the bulk viscosity shows large finite-size effects while shear viscosity has the smallest system-size dependency. In the next chapters, the developed plugin, OCTP, is used to obtain transport properties of fluids.

In chapter 4, EMD simulations were performed for the prediction of finite-size effects of Maxwell-Stefan diffusion coefficients of molecular mixtures and a wide variety of binary LJ systems. Computed self- and MS diffusivities are found to increase with the number of molecules. A correction is proposed for the extrapolation of Maxwell-Stefan diffusion coefficients to the thermodynamic limit, based on the study by Yeh and Hummer (Journal of Physical Chemistry B 108, 15873-15879 (2004)). The proposed correction is a function of the viscosity of the system, the size of the simulation box, and the so-called thermodynamic factor, which is a measure for the nonideality of the mixture. Verification is carried out for more than 200 distinct binary LJ systems, as well as 9 binary systems of methanol, water, ethanol, acetone, methylamine, and carbon tetrachloride. Significant deviations between finite-size Maxwell-Stefan diffusivities and the corresponding diffusivities in the thermodynamic limit are found for mixtures close to demixing. In these cases, the finite-size correction can be even larger than the computed (finite-size) Maxwell-Stefan diffusivity. These results show that considering these finite-size effects is crucial and that the suggested correction allows for reliable computations of mutual diffusion coefficients without system-size dependency. In the rest of this thesis, this correction is used to compute system-size independent mutual diffusivities.

In chapter 5, a method is proposed for calculating the shear viscosity of a liquid from finite-size effects of self-diffusion coefficients in EMD simulations. This method uses the difference in the self-diffusivities, computed from at least two system sizes, and an analytic equation to calculate the shear viscosity. To enable the efficient use of this method, a set of guidelines is developed. The most efficient number of system sizes is two and the large system should be at least four times the small system. The number of independent simulations for each system size should be assigned in such a way that ca. 50%-70% of the total available computational resources is allocated to the largest system. The method was verified for 250 binary and 26 ternary Lennard-Jones systems, pure water, and the ionic liquid [Bmim][Tf_2N]. The computed shear viscosities are in excellent agreement with viscosities obtained from EMD simulations for all systems not too close to the critical point. The results indicate that the proposed method is suitable for multicomponent mixtures and highly viscous liquids. This may enable the systematic screening of the viscosities of ionic liquids and deep eutectic solvents.

Force field improvement is the focus of the second part of this thesis. The main reason for such improvement is that current classical force fields often cannot provide accurate estimates for all properties of interest of a fluid. As an example, aqueous solutions of carbohydrates have an extensive food and pharmaceutical applications, which makes these systems an interesting subject for molecular simulation studies. However, the force fields show poor performance, mainly for concentrated solutions, where solute-solute interactions are overestimated. In chapter 6, a method is proposed to refine force fields of these systems, such that solute-solute interactions are more accurately described. The OPLS force field combined with the SPC/Fw water model is used as a basis. The non-bonded interaction parameters of sucrose, a disaccharide, are scaled. The scaling factors are chosen in such a way that experimental thermodynamic and transport properties of aqueous solutions of sucrose are accurately reproduced. In this way, excellent agreement could be obtained between experiments and computed liquid densities, thermodynamic factors, shear viscosities, self-diffusion coefficients, and Fick (mutual) diffusion coefficients. The transferability of the optimum scaling factors to other carbohydrates is verified by computing thermodynamic and transport properties of aqueous solutions of D-glucose, which is a monosaccharide. The good agreement between computed properties and experiments suggests that the scaled interaction parameters are transferable to other carbohydrates, especially for concentrated solutions.

Crown-ethers have recently been used to assemble porous liquids (PLs), which are liquids with permanent porosity formed by mixing bulky solvent molecules (e.g., 15-crown-5 ether) with solvent-inaccessible organic cages. PLs

and crown-ethers belong to a novel class of fluids, which can potentially be used for gas separation and storage, but their performance for this purpose needs to be assessed in detail. In chapter 7, molecular simulations are used to study the gas separation performance of crown-ethers. The TraPPE force field has been developed for linear ether molecules, but this force field may not be used for cyclic ether molecules. To accurately describe intermolecular interactions of cyclic crown-ether molecules, a new set of torsional potentials is refitted to torsional energies obtained from quantum mechanics computations. EMD simulations were used to compute densities, shear viscosities, and self-diffusion coefficients of 12-crown-4, 15-crown-5, and 18-crown-6 ethers. Monte Carlo (MC) simulations were used to compute the solubility of the gases CO_2, CH_4, and N_2 in 12-crown-4, and 15-crown-5 ether. The computed properties are compared with available experimental data of crown-ethers and their linear counterparts, i.e., polyethylene glycol dimethyl ethers. The good agreement between experimental and simulation results suggests that modifying the torsional potentials can correctly refine the force field without any need to change the other inter- and intramolecular potentials parameters.

SAMENVATTING

Kennis van transportcoëfficiënten van gassen en vloeistoffen is van groot belang voor de ontwikkeling van processen en producten in de chemische, voedingsmiddelen-, farmaceutische en biotechnologische industrie. In de afgelopen decennia hebben moleculaire simulaties zich ontwikkeld tot een belangrijk hulpmiddel om deze transportcoëfficiënten te berekenen. Moleculaire Dynamica (MD) is belangrijk voor de berekening van transporteigenschappen van complexe systemen waarvoor bestaande modellen niet geschikt zijn, of onder extreme omstandigheden waarbij het uitvoeren van experimenten gevaarlijk of onmogelijk is. MD simulaties verschaffen gedetailleerde informatie over de dynamica van een systeem op de moleculaire schaal. Het doel van dit proefschrift is om methoden waarmee transporteigenschappen berekend kunnen worden te onderzoeken met behulp van op interactiemodellen (force field-based) MD simulaties. Dit proefschrift bestaat uit twee delen. In het eerste deel (hoofdstukken 2-5) worden de methodologieën om transporteigenschappen te berekenen met behulp van Evenwichts Moleculaire Dynamica (EMD) en Niet-Evenwichts Moleculaire Dynamica (NEMD) simulaties besproken en toegepast om finite-size effecten van transporteigenschappen te onderzoeken. In het tweede deel (hoofdstukken 6 en 7) ligt de nadruk op de verbetering van force fields, aangezien force fields de nauwkeurigheid van de berekende eigenschappen van een MD simulatie bepalen.

De nadruk van dit proefschrift ligt op de berekening van de transporteigenschappen in EMD simulaties. NEMD methoden worden echter vaak gebruikt in moleculaire simulatiestudies vanwege hun voordelen in specifieke gevallen. Een belangrijk voorbeeld hiervan is de diffusie van kleine moleculen door een nanoporeus materiaal, zoals in het geval van ontzilting door middel van reverse osmosis. Een groot deel van de huidige commerciële waterontziltingssystemen is gebaseerd op reverse osmosis. Het gebruik van membranen met grote waterfluxen met behoud van een hoge salt-rejection is van cruciaal belang voor het verminderen van het energieverbruik en de kosten. Het feit dat zeoliet-nanosheets ultradun zijn en gevarieerde poriestructuren kunnen hebben, biedt veel mogelijkheden voor gebruik in ontzilting. In hoofdstuk 2 worden testen we, aan de hand van NEMD simulaties, systematisch de fundamentele relaties tussen de structuur en prestaties van zeolieten als reverse osmosis membranen. Zeoliet nanosheets kunnen een hoge salt-rejection van bijna 100% bereiken, en kunnen tevens

een waterdoorlaatbaarheid bereiken van bijna twee ordegroottes hoger dan de huidige beschikbare membranen. De effecten van de poriedichtheid, de aanwezigheid van open ruimten en de vrije energiebarrière van membranen op de waterpermeabiliteit en salt-rejection worden ontrafeld, wat leidt tot een belangrijk inzicht in het rationele ontwerp van nieuwe zeolietmembranen.

Het bestuderen van transporteigenschappen met behulp van MD vereist een manier om de eigenschappen van het systeem efficiënt en eenduidig te samplen. In hoofdstuk 3 wordt een nieuwe plugin voor LAMMPS gepresenteerd voor On-the-fly Computation of Transport Properties (OCTP). Deze plugin berekent door middel van één enkele simulatie de zelf- en Maxwell-Stefan (MS) diffusiecoëfficiënten, bulk- en afschuifviscositeiten en de thermische geleidbaarheid van pure substanties en mengsels. OCTP is de eerste implementatie in LAMMPS die gebruik maakt van de Einstein-relaties in combinatie met het order-n-algoritme voor het efficiënt samplen van dynamische variabelen. In dit hoofdstuk wordt de berekening van de transporteigenschappen met behulp van EMD simulaties in detail beschreven. De efficiëntie van de nieuwe plugin wordt gedemonstreerd door de transporteigenschappen van een equimolair water-methanol mengsel bij 298 K en 1 bar te berekenen. Finite-size effecten van de transporteigenschappen van een Lennard-Jones (LJ) vloeistof dicht bij het kritische punt worden bestudeerd. De resultaten van deze studie laten zien dat een eindige grootte van het simulatiesysteem een grote invloed heeft op de bulkviscositeit, terwijl er slechts een kleine invloed is op de afschuifviscositeit. In de volgende hoofdstukken wordt de ontwikkelde OCTP plugin gebruikt om de transporteigenschappen van vloeistoffen te berekenen.

In hoofdstuk 4 worden EMD simulaties uitgevoerd voor het voorspellen van finite-size effecten van Maxwell-Stefan diffusiecoëfficiënten van moleculaire mengsels en van een grote verscheidenheid aan binaire LJ systemen. De berekende zelf- en MS-diffusiecoëfficiënten blijken toe te nemen met de systeemgrootte. Een correctie wordt voorgesteld voor de extrapolatie van Maxwell-Stefan diffusiecoëfficiënten naar de thermodynamische limiet. Deze correctie is gebaseerd op de studie van Yeh en Hummer (The Journal of Physical Chemistry B 108, 15873-15879 (2004)). De voorgestelde correctie is een functie van de viscositeit van het systeem, de grootte van het systeem in de simulatie, en de zogenaamde thermodynamische factor, welke een maat is voor de niet-idealiteit van het mengsel. Deze correctie wordt getest voor meer dan 200 verschillende binaire LJ-systemen, alsmede 9 binaire systemen van methanol, water, ethanol, aceton, methylamine en tetrachloorkoolstof. Significante afwijkingen tussen Maxwell-Stefan diffusiecoëfficiënten voor systemen met een eindige grootte en de corresponderende diffusiecoëfficiënten in de thermodynamische limiet worden gevonden voor mengsels die nog net geen fasescheiding ondergaan. In deze

gevallen kan de finite-size correctie zelfs groter zijn dan de berekende Maxwell-Stefan diffusiviteit. Deze resultaten tonen aan dat het meenemen van finite-size effecten van cruciaal belang is en dat de voorgestelde correctie betrouwbare berekeningen van de Maxwell-Stefan diffusiecoëfficiënt mogelijk maakt zonder systeem-grootte afhankelijkheid. In de rest van dit proefschrift wordt deze correctie gebruikt om diffusiecoëfficiënten in de thermodynamische limiet te berekenen.

In hoofdstuk 5 wordt een methode voorgesteld om de afschuifviscositeit van een vloeistof te berekenen met behulp van EMD simulaties. Deze methode maakt gebruik van het verschil in de zelf-diffusiecoëfficiënten, berekend voor ten minste twee systeemgroottes, en een analytische vergelijking om de afschuifviscositeit te berekenen. Richtlijnen worden ontwikkeld om een efficiënt gebruik van deze methode mogelijk te maken. Het meest efficiënte aantal systeemgroottes is twee en het grootste systeem moet minstens vier keer zo groot zijn als het kleinste systeem. Het aantal onafhankelijke simulaties voor elke systeemgrootte moet zodanig worden toegewezen dat ca. 50%-70% van de totale beschikbare rekenkracht aan het grootste systeem wordt besteed. De methode is geverifieerd voor 250 binaire en 26 ternaire Lennard-Jones systemen, water en de ionische vloeistof [Bmim][Tf2N]. Voor alle systemen komt de berekende afschuifviscositeit uitstekend overeen met de viscositeit verkregen uit EMD simulaties, mits het systeem ver genoeg verwijderd is van het kritisch punt. Uit de resultaten blijkt dat de voorgestelde methode geschikt is voor mengsels van meerdere componenten en voor zeer viskeuze vloeistoffen. Dit kan een systematische screening van de viscositeit van ionische vloeistoffen en diep eutectische oplosmiddelen mogelijk maken.

Het tweede deel van dit proefschrift staat in het teken van het verbeteren van force fields. De belangrijkste reden voor een dergelijke verbetering is dat de huidige klassieke force fields vaak geen nauwkeurige schatting van relevante vloeistofeigenschappen opleveren. Een typisch voorbeeld hiervan zijn waterige oplossingen van koolhydraten. Deze oplossingen hebben diverse voedings- en farmaceutische toepassingen, hetgeen deze systemen een interessant onderwerp maakt voor moleculaire simulaties. De force fields presteren echter slecht. Met name in geconcentreerde oplossingen worden de interacties tussen koolhydraten overschat. In hoofdstuk 6 wordt een methode voorgesteld om de force fields van deze systemen te verbeteren zodat de interacties tussen koolhydraten nauwkeuriger beschreven kunnen worden. Het OPLS force field in combinatie met het SPC/Fw watermodel wordt gebruikt als basis. De niet-covalente interactieparameters van sucrose, een disacharide, worden geschaald. De schaalfactoren worden zo gekozen dat de experimentele thermodynamische en transporteigenschappen van waterige oplossingen van sucrose nauwkeurig worden gereprodu-

ceerd. Op deze manier kan een uitstekende overeenkomst worden bereikt tussen experimenten en berekende vloeistofdichtheden, thermodynamische factoren, afschuifviscositeiten, zelf-diffusiecoëfficiënten, en Fick diffusiecoëfficiënten. De overdraagbaarheid van de optimale schaalfactoren naar andere koolhydraten wordt geverifieerd aan de hand van thermodynamische en transporteigenschappen van waterige oplossingen van D-glucose (een monosacharide). De goede overeenkomst tussen berekende eigenschappen en experimenten suggereert dat de geschaalde interactieparameters ook toegepast kunnen worden op andere koolhydraten, vooral ook voor geconcentreerde oplossingen.

Kroonethers zijn recentelijk gebruikt voor het creëren van poreuze vloeistoffen (PV's). Dit zijn vloeistoffen met een permanente porositeit die gevormd worden door het mengen van oplosmiddelen bestaande uit grote moleculen (bijv. 15-kroon-5 ether) met organische openingen die niet toegankelijk zijn voor het oplosmiddel. PV's en kroonethers behoren tot een nieuwe klasse van vloeistoffen die potentieel gebruikt kunnen worden voor gasscheidingen en -opslag. Hun geschiktheid voor dit doel moet dient verder onderzocht te worden. In hoofdstuk 7 worden moleculaire simulaties gebruikt om de geschiktheid van kroonethers om verschillende gassen te scheiden te bestuderen. Het TraPPE force field is ontwikkeld voor lineaire ethermoleculen, maar dit force field is niet geschikt voor cyclische ethermoleculen. Om de intermoleculaire interacties van cyclische kroonether moleculen nauwkeurig te beschrijven zijn torsie-energiën verkregen uit kwantummechanische berekeningen gebruikt om een nieuwe set van torsiepotentialen te fitten. EMD simulaties zijn vervolgens gebruikt om dichtheden afschuifviscositeiten, en zelfdiffusiecoëfficiënten van 12-kroon- 4, 15-kroon-5, en 18-kroon-6 ethers te berekenen en Monte Carlo simulaties zijn gebruikt om de oplosbaarheid van de gassen CO_2, CH_4 en N_2 in 12-kroon-4 en 15 kroon-5 ether te berekenen. De berekende eigenschappen worden vergeleken met beschikbare experimentele gegevens van kroonethers en hun lineaire tegenhangers, d.w.z. polyethyleenglycoldimethylethers. De goede overeenstemming tussen experimentele en simulatieresultaten suggereert dat het mogelijk is om het force field te verbeteren door de torsiepotentialen te wijzigen, zonder de parameters van de andere inter- en intramoleculaire potentialen te veranderen.

CURRICULUM VITAE

Seyed Hossein Jamali was born on 5 August 1989 in Tehran, Iran. In 2012, he obtained his Bachelor of Science degree in Mechanical Engineering from the University of Tehran. He then continued his study at Delft University of Technology and carried out his MSc project under the supervision of Prof. Dirk Roekaerts on the subject of flameless combustion. He received his Master of Science degree in 2014, with the specialization Sustainable Process and Energy Technology (SPET). In 2015, he started his PhD at Engineering Thermodynamics group in Delft University of Technology under the supervision of Dr. Li-Chiang Lin and Prof. Thijs J. H. Vlugt, followed by Dr. Othonas Moultos. In this period, he was working on molecular simulation techniques, e.g., Monte Carlo and Molecular Dynamics simulations. He used these simulation techniques to investigate the performance of nanoporous materials and different fluids for separation applications, such as water desalination and gas treatment. In collaboration with the Institute of Technical Thermodynamics at RWTH Aachen University, he investigated transport properties of fluids computed from molecular simulation. This dissertation presents the results of these studies.

LIST OF PUBLICATIONS

Publications included in this thesis:

1. S.H. Jamali, L. Wolff, T.M. Becker, M. de Groen, M. Ramdin, R. Hartkamp, A. Bardow, T.J.H. Vlugt, and O.A. Moultos, *OCTP: A Tool for On-the-fly Calculation of Transport Properties of Fluids with the Order-n Algorithm in LAMMPS*, Journal of Chemical Information and Modeling, **59**, 1290-1294 (2019).

2. S.H. Jamali, T. van Westen, O.A. Moultos, and T.J.H. Vlugt, *Optimizing Nonbonded Interactions of the OPLS Force Field for Aqueous Solutions of Carbohydrates: How to Capture Both Thermodynamics and Dynamics*, Journal of Chemical Theory and Computation, **14**, 6690-6700 (2018).

3. S.H. Jamali, R. Hartkamp, C. Bardas, J. Söhl, T.J.H. Vlugt, and O.A. Moultos, *Shear Viscosity Computed from the Finite-Size Effects of Self-Diffusivity in Equilibrium Molecular Dynamics*, Journal of Chemical Theory and Computation, **14**, 5959-5968 (2018).

4. S.H. Jamali, L. Wolff, T.M. Becker, A. Bardow, T.J.H. Vlugt, and O.A. Moultos, *Finite-size Effects of Binary Mutual Diffusion Coefficients from Molecular Dynamics*, Journal of Chemical Theory and Computation, **14**, 2667-2677 (2018).

5. S.H. Jamali, M. Ramdin, T.M. Becker, S.K. Rinwa, W. Buijs, and T.J.H. Vlugt, *Thermodynamic and Transport Properties of Crown-ethers: Force Field Development and Molecular Simulations.* Journal of Physical Chemistry B, **121**, 8367-8376 (2017).

6. S.H. Jamali, T.J.H. Vlugt, and L.-C. Lin, *Atomistic Understanding of Zeolite Nanosheets for Water Desalination.* Journal of Physical Chemistry C, **121**, 11273-11280 (2017).

Publications not included in this thesis:

1. S.H. Jamali, A. Bardow, T.J.H. Vlugt, and O.A. Moultos, *A Generalized Form for Finite-size Corrections in Mutual Diffusion Coefficients of Multicomponent Mixtures Obtained from Equilibrium Molecular Dynamics Simulation*, submitted.

2. I.N. Tsimpanogiannis, S.H. Jamali, I.G. Economou, T.J.H. Vlugt, and O.A. Moultos, *On the Validity of the Stokes-Einstein Relation for Various Water Force Fields*, Molecular Physics, in press, https://doi.org/10.1080/00268976.2019.1702729.

3. S.H. Jamali, M. de Groen, O.A. Moultos, R. Hartkamp, T.J.H. Vlugt, W. Ubachs, and W. van der Water, *Rayleigh-Brillouin Light Scattering Spectra of CO_2 from Molecular Dynamics*, Journal of Chemical Physics, **151**, 064201 (2019).

4. A. Rahbari, R. Hens, S.H. Jamali, M. Ramdin, D. Dubbeldam, and T.J.H. Vlugt, *Effect of Truncating Electrostatic Interactions on Predicting Thermodynamic Properties of Water–methanol Systems*, Molecular Simulation, **45**, 336-350 (2019).

5. L. Wolff, S.H. Jamali, T.M. Becker, O.A. Moultos, T.J.H. Vlugt and A. Bardow, *Prediction of Composition-dependent Self-diffusion Coefficients in Binary Liquid Mixtures: The Missing Link for Darken-based Models*, Industrial & Engineering Chemistry Research, **57**, 14784-14794 (2018).

6. T.M. Becker, M. Wang, A. Kabra, S.H. Jamali, M. Ramdin, D. Dubbeldam, C.A. Infante Ferreira, and T.J.H. Vlugt, *Absorption Refrigeration Cycles with Ammonia–ionic Liquid Working Pairs Studied by Molecular Simulation*, Industrial & Engineering Chemistry Research, **57**, 5442-5452 (2018).

7. M. Ramdin, S.H. Jamali, L.J. van den Broeke, W. Buijs, and T.J.H. Vlugt, *CO_2 Solubility in Small Carboxylic Acids: Monte Carlo Simulations and PC-SAFT Modeling*. Fluid Phase Equilibria, **458**, 1-8 (2018).

8. M. Ramdin, S.H. Jamali, T.M. Becker, and T.J.H. Vlugt, *Gibbs Ensemble Monte Carlo Simulations of Multicomponent Natural Gas Mixtures*. Molecular Simulation, **44**, 377-383 (2018).

9. S.H. Jamali, M. Ramdin, T.M. Becker, A. Torres-Knoop, D. Dubbeldam, W. Buijs, and T.J.H. Vlugt, *Solubility of Sulfur Compounds in Commercial Physical Solvents and an Ionic Liquid from Monte Carlo Simulations*. Fluid Phase Equilibria, **433**, 50-55 (2017).

10. M. Ramdin, T.M. Becker, S.H. Jamali, M. Wang, and T.J.H. Vlugt, *Computing Equation of State Parameters of Gases from Monte Carlo Simulations*. Fluid Phase Equilibria, **428**, 174-181 (2017).

ACKNOWLEDGMENTS

A PhD dissertation is a small part of a long journey. I could not complete this journey and this stage of my life without the help of my family, my friends, and colleagues, whom I would like to thank.

First and foremost, I thank my supervisors, Thijs and Otto (Othonas). Thijs, as my promotor, you have always been supportive. When I started my PhD and when I had to define a new project, you gave me directions without restricting my freedom to choose what I prefer. I really appreciate that you were always accessible, and it was easy to ask for your feedback. This helped me to focus only on my research. Meanwhile, you have always been critical about the outcome of a research and this is the most appreciated quality I learned during my PhD. Otto, you became my direct supervisor since the end of my second year. You helped me define a specific subject for my PhD to focus only on one subject. You were always open to scientific discussions and challenges. Also, I enjoyed having the occasional coffee or dinner plans in the center of Delft. This was a good social aspect of my PhD life.

I thank my first PhD supervisor, Li-Chiang (Lin). Although we worked for less than a year, I learned many things from you, especially persistence and accuracy. David (Dubbeldam), you always welcomed us whenever our group came to Amsterdam Science Park. You also helped me with programming issues or implementation of new functionalities in RASPA. Wim (Buijs), I met you for the first time during my MSc at the course Technology and Sustainability, followed by Advanced Thermodynamics. The latter made curious about molecular simulation, which lead me to start my PhD on this subject. Since then, whenever I had a question about chemistry and later quantum mechanics, you explained me the answers with passion and in great detail. During coffee breaks, I also enjoyed listening to your work and personal experiences. Remco (Hartkamp), you were always available for any help, and I could use your experience in molecular simulation. I appreciate that you translated the summary of my dissertation to Dutch.

I would like to thank Prof. André Bardow and Ludger Wolff from RWTH Aachen. Ludger, it was late 2015 when you came to Delft for a short visit, followed by a three-month visit in the summer of 2016. While this visit was for a short collaboration between our groups in Delft and Aachen, I could continue the work and it became an important part of my PhD. You and André were hos-

pitable when we visited your group in Aachen, and I enjoyed having discussions and working with you. Thanks to you, the collaboration is one of my best memories of my PhD.

While not being a part of my PhD, I could work on the interesting subject of bulk viscosity of fluids with great colleagues: Hassan (Nemati), Mariëtte (de Groen), and Willem (van der Water). Hassan, you were really helpful when I was carrying out my MSc thesis and later when I started my PhD. I came many times to your office and asked you questions about Linux, programming, and MPI. When I came early in the morning to work, you were also there to start the day with a cup of coffee and lots of energy. Mariëtte, thanks for the nice collaboration as well as the nice Dutch discussions that we had. It was a great practice for me, and I am missing those talks. You are truly patient, and you managed to endure my slecht Nederlands. Also thanks for introducing me to the concerts in Delft. Willem, I was very lucky to know you because of this project. Since Physics was not my background, I could not follow many subjects, but you explained them in meticulous detail. It was not only the scientific aspects for which I enjoyed working with you, but also the talks and lunches we had. It was a great pleasure to meet you.

When I had to define my new PhD project, I could have constructive talks with the postdocs in our group: Martijn (de Lange) and Mahinder (Ramdin). Martijn, you were a good colleague and office mate. I learned many things about nanoporous materials from you. Mahinder, you are a great friend. I enjoyed all coffee breaks we had to discuss both work-related and non-scientific subjects. I always appreciated that while you helped me in work, you also acknowledged my contribution to the projects.

Thijs (van Westen), you finished your PhD before I started mine, so I could take your desk and your computer. Fortunately, we could carry out a project on simulations of saccharides, and it is now a chapter of my dissertation. I appreciate the time you spent on the project and meticulously checked all results while I can clearly remember that you were totally busy. Tim (Becker), you had a totally different PhD subject; however, we managed to have many collaborations. We took courses together, supervised MSc students, attended courses and conferences, and published articles. One my best memories from my PhD is still the two-week thermodynamic course in Denmark, where we stayed in the center of Cophenhagen.

During these four years, I had the chance to be directly or indirectly involved in three MSc theses. I enjoyed working with Robin (Buitendijk), Prajakta (Nakate), and Shwet (Kumar Rinwa). Being your supervisor was a great experi-

ence for me. I also appreciate the help of Prof. Arian Nijmeijer at Shell Global, who helped for the project “molecular simulation of membranes for gas separation”.

My other colleagues in the group of Engineering Thermodynamics made a good memory of my PhD: Máté (Erdős), Hirad (Salehi), Remco (Hens), Noura (Dawass), Sebastian (Caro-Ortiz), Alper (Celebi), Christos (Bardas), and Max (Döpke), you are really good friends and colleagues inside and outside the university. We went together to conferences, workshops, and meetings, and we spend time for other activities outside the work. I have also good memories with my other colleagues at the Engineering Thermodynamic group: Carlos (Infante Ferreira), Brian (Tighe), Meng (Wang), Zhaochuan (Fan), Sayee (Prasaad Balaji), Vilborg (Gudjonsdottir), Bernardo (Oyarzun Rivera), Hongxia (Zhou), Karsten (Baumgarten), Dion (Koeze), and Xuan (Tao). Seeing each other during group meetings might not be our best memories as everybody focused on his/her work, but I am happy that I know all of you in these years and learned about your expertise.

It was a quite unique experience to work in the biggest office of Process & Energy with many office mates through 2015 to 2019: Vincent (Oldenbroek), Nikolaos (Chrysochoidis-Antsos), Gustavo (Otero), Rishabh (Ghotge), Uttiya (Sengupta), Valentina (Valori), MengMeng (Zhang), Selvaraj (Chinnathambi), and Jie (Ren), in addition to the other colleagues that I have named. Essentially, I spent most of my time at TU Delft with you. You made a vibrant atmosphere by having small coffee breaks and other sorts of activities such as the secret Santa. I did my best to be a good office mate for you and I hope you had good times in these years when I was in the office. Furthermore, I met many Iranian friends: Nafiseh (Talebanfard), Fatima (Anisi) and Erfan (Hoseini), Maryam (Khodadadian), Mohammad (Mehrali), Samira (Farahani), and Farnaz (Eghbal). It is always great to see you at the coffee machine and have discussions about everything from everywhere. Finally, I met some colleagues in the past few years at Process & Energy or other universities: Peter (van den Broeke), Nazila (Yaghini), Arianna (Torres-Knoop), Jurn (Heinen), and Jakob (Söhl). I would like to thank you all for making good memories during my PhD.

In June 2019, I started my work at Van Oord. It was a pleasure to meet and work with Michel (de Nijs), Willem (Eerland), and Behzad (Soltanbeigi). You encouraged me to proceed with my dissertation. Because of the good atmosphere at work, I had the energy to work on my dissertation during my free time, and after 8 months, my dissertation is ready.

In the past eight years that I have been in the Netherlands, I had my friends who helped to reach here. During my MSc, I had the supervision of Dirk Roekaerts (MSc thesis supervisor), Likun Ma (MSc thesis supervisor), Carlos

Infante Ferreira (internship supervisor), and Jo Berkhoff (internship supervisor at Fluor). Your utmost attention makes it possible for me to enjoy my study in Delft. Now that I review 2012-2014, these were great years when I learned many new subjects with which I was not familiar, and I found the courage to study any new subject, knowing that I can achieve it.

In addition to my colleagues, I would like to thank my friends in the Netherlands. Eight years ago, I started my MSc at Sustainable Process and Energy Technology with Ali (Poursaeidesfahani), Arash (Rasooli), and Ahmadreza (Rahbari). Later, I met Shima (Ebrahimigharehbaghi) and Elyas (Mohammadzadeh Moghaddam). You were the closest friends in the Netherlands, and I could feel at home while being far from my family. I have enjoyed the travels, dinners, etc. which we have done together. We always discuss about different subjects. These discussions have given a me a better understanding of the world and life. Thanks to you, I made many changes (improvements) in my life in the past eight years.

I would like to thank all my friends, teachers, and professors from Rouzbeh high school and the University of Tehran; especially, my dearest friends, Hossein (Karami), Abbas (Sohrabpour), Mohamad (Mahmoudi), Alireza (Ghasemi), Amin (Niayifar), and Ramin (Abkar), as well as Prof. Vahid Esfahanian and Prof. Keumarce J. Shaghaghi. I am very happy that we are still in contact although we may be thousands of kilometers apart.

Finally, I would like to express my special thanks to my family: my father, mother, and sister. You always appreciated the importance of education and did all your best to provide me the best education. I went to the best schools and universities thanks to your support. You are always my best role model, and I appreciate what you did for me.

Now I am here at the end of my PhD. With the end of this stage, new stages will start. I am continuing my path with this belief that I have the support of my family and friends to overcome any problem.